

SPATIAL CHARACTERISTICS OF A
FURNACE ATOMIZATION PLASMA EXCITATION SPECTROMETRY SOURCE

By

CHARLES WILFRED LE BLANC

B.Sc.H., Acadia University, 1986

M.Sc., University of British Columbia, 1989

A THESIS SUBMITTED IN PARTIAL FULFILLMENT OF THE
REQUIREMENTS FOR THE DEGREE OF
DOCTOR OF PHILOSOPHY

in

THE FACULTY OF GRADUATE STUDIES
Department of Chemistry

We accept this thesis as conforming
to the required standard

THE UNIVERSITY OF BRITISH COLUMBIA

February, 1996

© Charles Wilfred Le Blanc, 1996

In presenting this thesis in partial fulfilment of the requirements for an advanced degree at the University of British Columbia, I agree that the Library shall make it freely available for reference and study. I further agree that permission for extensive copying of this thesis for scholarly purposes may be granted by the head of my department or by his or her representatives. It is understood that copying or publication of this thesis for financial gain shall not be allowed without my written permission.

Department of Chemistry

The University of British Columbia
Vancouver, Canada

Date March 26/1996

ABSTRACT

Furnace atomization plasma excitation spectrometry (FAPES) is a relatively new atomic emission elemental analysis technique. In FAPES, a radio frequency (r.f.) plasma is created inside the cuvette of a graphite furnace atomizer by applying r.f. power to an electrode placed inside, and coaxial with, the atomization chamber of the cuvette. The plasma provides the energy to excite analyte atoms which then emit the light measured as the analytical signal. In the research reported in this thesis, the spatial structure of this plasma was studied using spectroscopic techniques.

Spatially resolved OH and N_2^+ molecular and Pb(I) excitation temperature measurements showed that there is a significant thermal gradient in the source with higher temperatures adjacent to the center electrode and cuvette wall. Spatially resolved absorption and emission profiles of an In(I) line were measured to determine the spatial distributions of ground and excited states in the plasma. The emission profiles contained three concentric emission maxima; the most intense was adjacent to the center electrode, another was adjacent to the cuvette wall, and the third was separated from these maxima by two emission minima. These maxima and minima did not appear in the absorption profiles thus must be due to plasma excitation processes. Spatially resolved magnesium ionization measurements showed that the zones adjacent to the graphite cuvette and center electrode have the highest degree of ionization which causes a decrease in the atomic emission signal at higher r.f. powers. As the pressure in the source was decreased, the emission maxima adjacent to the center electrode and

adjacent to the cuvette wall moved away from the graphite surfaces creating dark spaces.

These observations suggest that the FAPES source operates as an atmospheric pressure r.f. glow discharge. Two concentric negative glows, adjacent to the cuvette wall and center electrode, are seen where there are maxima in both ionic and atomic emission intensities. Moving away from these glows there are then two Faraday dark spaces. The emission maximum between these is the positive column which exhibits relatively weak ionic emission. Furthermore, cathode dark spaces appear adjacent to each electrode as the pressure is decreased from atmospheric.

TABLE OF CONTENTS

Abstract	ii
Table of Contents	iv
List of Tables	viii
List of Figures	ix
List of Abbreviations	xiii
Acknowledgments	xiv
Chapter 1	
Introduction	1
1.1 FAPES	1
1.2 Thesis Objective	2
1.3 Development of the FAPES and Related Sources	3
1.3.1 A Brief Historical Background	3
1.3.2 Plasma Optical Emission Sources	4
1.3.3 Emission Sources Based on Graphite Furnaces	5
1.4 Electrical Discharges in Gases	8
1.5 Fundamental Properties of Spectrochemical Plasmas and their Measurement	11
1.5.1 Atom and Ion Populations	12
1.5.2 Electron Number Densities	12
1.5.3 Temperature Measurements	13
1.6 A Survey of FAPES Research	15
1.7 Thesis Overview	18

Chapter 2

Experimental	20
2.1 The Experimental System	20
2.1.1 The FAPES Sources	22
2.1.1.1 The GF-CCP-100 Source	23
2.1.1.2 The Cube Source	25
2.1.2 Detection System	27
2.1.2.1 Optical Configuration	28
2.1.2.2 The Monochromator and CCD Detector	29
2.2 Data Acquisition	31
2.3 Analyte Atomization	33

Chapter 3

Spatially Resolved Temperature Measurements	35
3.1 Introduction	35
3.2 Experimental	37
3.2.1 Background	37
3.2.1.1 OH Rotational Temperature Measurements	37
3.2.1.2 N_2^+ Rotational Temperature Measurements	39
3.2.1.3 Pb(I) Excitation Temperature Measurements	39
3.2.2 Instrumental Parameters	41
3.2.3 Procedure	42
3.3. Results and Discussion	43
3.3.1 The Effect of R.F. Power on the Spatial Profiles of He, OH, and N_2^+ Emission Lines	43

3.3.2	Rotational Temperature Profiles of OH and N_2^+	51
3.3.3	Pb(I) Excitation Temperatures.....	56
3.4	Summary and Conclusions	59
Chapter 4		
	Analyte Spatial and Temporal Profiles	60
4.1	Introduction	60
4.2	Experimental	62
4.2.1	Background	62
4.2.2	Instrumental Parameters	63
4.2.3	Procedure	64
4.3	Results and Discussion	65
4.4	Summary and Conclusions	87
Chapter 5		
	Analyte Ionization in the FAPES Source	88
5.1	Introduction	88
5.2	Experimental	89
5.2.1	Background	89
5.2.2	Instrumental Parameters	89
5.2.3	Procedure.....	90
5.3	Results and Discussion	91
5.3.1	Effect of Magnesium Load on Mg(I) and Mg(II) Emission Line Intensities.	91
5.3.2	Effect of R.F. Power on Mg(I) and Mg(II) Emission Line Intensities.	97
5.4	Summary and Conclusions	108

Chapter 6	
Reduced Pressure Studies	110
6.1 Introduction	110
6.2 Experimental	111
6.2.1 Background	111
6.2.2 Instrumental Parameters	112
6.2.3 Procedure	112
6.3 Results and Discussion	113
6.4 Summary and Conclusions	123
Chapter 7	
Additional Observations	125
7.1 Introduction	125
7.2 Visual Observations in the FAPES source	125
7.3 Center Electrode Self-Bias	129
7.4 Attempts at Spatially Resolved Electron Number Density Measurements	132
Chapter 8	
Conclusion	134
8.1 Summary	134
8.2 Suggestions for Future Research	138
References	141

LIST OF TABLES

Table	Page
1.1 Lowest FAPES detection limits reported thus far. Values are calculated as three time the standard deviation of the background ($3\sigma_B$). Values are for helium plasmas unless otherwise indicated.....	16
3.1 Spectroscopic data for Pb(I) lines used to calculate excitation temperatures.....	41
5.1 Magnesium detection limits for various techniques. Values were calculated as 3σ of the background intensity except for the GFAAS result which represents an absorbance value of 0.025.....	97
5.2 R.F. power where the atomic emission intensity is a maximum in the FAPES and analyte ionization potentials.....	100
5.3 Parameters used for calculating magnesium ion/atom population ratios from ion/atom emission intensity ratios.....	102

LIST OF FIGURES

Figures	Page
1.1 FAPES graphite cuvette and center electrode configuration.....	2
1.2 Atomizer configuration for two-step furnace.....	6
1.3 Hollow cathode furnace atomization non-thermal excitation spectrometry (HC-FANES) source configuration.	7
1.4 Voltage-current plot for various gas-discharges.....	9
1.5 Schematic illustration of a direct current electrical discharge at reduced pressure.	9
2.1 Schematic diagram of the experimental setup.	21
2.2 The GF-CCP-100 prototype FAPES source work-head.....	24
2.3 The Cube FAPES source work-head.	27
2.4 Sequence of events during data acquisition using the FAPES sources.	32
3.1 OH spectrum in the FAPES source at 60 Watts r.f. power.....	38
3.2 N_2^+ spectrum in the FAPES source at 60 Watts r.f. power.	40
3.3 Effect of r.f. power on the spatially integrated emission intensities from He(I), N_2^+ , and OH.....	45
3.4 He(I) 388.86 nm emission intensity spatial profiles measured at different r.f. powers.....	48
3.5 Vertical emission profiles of the sum of the N_2^+ lines measured at different r.f. powers.....	49
3.6 Vertical emission profiles of the sum of the OH lines measured at different r.f. powers.....	50

3.7	N_2^+ rotational temperature vertical profile at 60 Watts r.f. power.	52
3.8	OH rotational temperature vertical profile at 60 Watts r.f. power.	52
3.9	Effect of r.f. power on the spatial profile of the OH rotational temperature.	54
3.10	Effect of r.f. power on the spatial profile of the N_2^+ rotational temperature.	54
3.11	Partial energy level diagram for He_2^+ , $He(2^3S)$ and N_2^+	55
3.12	Spatial emission profile of the Pb(I) 280.20 nm line for a 10 ng lead sample with 25 Watts r.f. power.	57
3.13	Spatial profile of Pb(I) excitation temperature at 25 Watts r.f. power.....	57
3.14	Effect of r.f. power on Pb(I) excitation temperature.....	58
4.1	Effect of r.f. power on the emission intensity of the In(I) 303.94 nm line from 10 ng of indium and on its Boltzmann factor. (A) shows the emission intensity as a function of r.f. power. (B) shows the emission intensity as a function of time.	67
4.2	Spatially and temporally resolved In(I) 303.94 nm line emission profiles from 10 ng indium with 6 Watts r.f. power.	70
4.3	Spatially and temporally resolved In(I) 303.94 nm line emission profiles from 10 ng indium with 10 Watts r.f. power.	71
4.4	Spatially and temporally resolved In(I) 303.94 nm line emission profiles from 10 ng indium with 20 Watts r.f. power.	72
4.5	Spatially and temporally resolved In(I) 303.94 nm line emission profiles from 10 ng indium with 40 Watts r.f. power.	73
4.6	Spatially and temporally resolved In(I) 303.94 nm line emission profiles from 10 ng indium with 60 Watts r.f. power.	74
4.7	Spatially and temporally resolved In(I) 303.94 nm line emission profiles from 10 ng indium with 80 Watts r.f. power.	75
4.8	Spatially and temporally resolved In(I) 303.94 nm line emission profiles from 10 ng indium with 100 Watts r.f. power.	76

4.9	Temporally integrated spatially resolved In(I) 303.94 nm emission intensity at various r.f. powers. (A) represents relative emission intensity and (B) represents the area normalized emission intensity.	80
4.10	Spatially and temporally resolved In(I) 303.94 nm line emission profiles from 10 ng indium with 20 Watts r.f. power.	82
4.11	Indium lamp 303.94 nm spatial emission profile after passing through the furnace.	84
4.12	Indium absorption profile at 303.94 nm for 0.3 s integration at 3.0 s in the atomization cycle.	84
4.13	Absorbance profiles for 10 ng indium samples at 303.94 nm. Integration time was 0.3 s.	85
4.14	Spatially averaged emission and absorbance signal as a function of time for 10 ng of indium in a 20 Watt FAPES.	86
5.1	Calibration plots for magnesium with 20 Watts r.f. power.	92
5.2	Log-log magnesium calibration plots with 20 Watts r.f. power.	93
5.3	Magnesium ion/atom emission intensity ratio as a function of magnesium load with 20 Watts r.f. power.	94
5.4	Mg(I) 285.21 nm spectral line profile for several magnesium loads in a 20 Watts plasma.	96
5.5	Spatially and temporally integrated magnesium atom and ion emission intensities from 0.5 ng magnesium samples at different r.f. powers.	99
5.6	Mg(II)/Mg(I) emission intensity ratio for 0.5 ng magnesium samples as a function of r.f. power.	101
5.7	Degree of magnesium ionization at different r.f. powers.	103
5.8	Spatially resolved Mg(I) 285.21 nm (A) and Mg(II) 279.55 nm (B) emission profiles for 0.5 ng magnesium samples at several r.f. powers.	105
5.9	Spatially resolved magnesium ion/atom emission intensity ratios (A) and degree of magnesium ionization (B) at several r.f. powers.	107
6.1	Spatially resolved He(I) 388.86 nm emission in a 20 Watt plasma at several pressures.	114

6.2	Spatially resolved N_2^+ emission in a 20 Watt plasma at several pressures.....	115
6.3	Integrated emission intensities for He(I) and N_2^+ emission lines in a 20 Watt plasma as a function of pressure.....	119
6.4	Diameter of the emission intensity maximum for the He(I) and N_2^+ lines in a 20 Watt plasma as a function of pressure.....	119
7.1	Visual end view appearance of the helium FAPES source at different r.f. powers.....	126
7.2	Schematic of a high frequency glow discharge circuit.	129
7.3	General trend of the d.c. bias on the center electrode in the FAPES source. Data shown represents typical values found over the course of the research.	131
7.4	Effect of pressure on the magnitude of the center electrode self-bias for a 60 W plasma.....	132
8.1	End-view schematic illustration of the FAPES source showing the different spatial zones present at atmospheric pressure.....	138

LIST OF ABBREVIATIONS

AAS	Atomic Absorption Spectrometry
CCD	Charged Coupled Device
d.c.	Direct Current
DCP	Direct Current Plasma
EIE	Easily Ionizable Element
FANES	Furnace Atomization Non-thermal Excitation Spectrometry
FAPES	Furnace Atomization Plasma Excitation Spectrometry
GD	Glow Discharge
GFAAS	Graphite Furnace Atomic Absorption Spectrometry
GFAES	Graphite Furnace Atomic Emission Spectrometry
HA-FANES	Hollow Anode Furnace Atomization Non-thermal Excitation Spectrometry
HC-FANES	Hollow Cathode Furnace Atomization Non-thermal Excitation Spectrometry
ICP	Inductively Coupled Plasma
MIP	Microwave Induced Plasma
r.f.	Radio Frequency
W	Watt

ACKNOWLEDGMENTS

This work is dedicated to my parents, Celina and Wilfred, for always giving me their unconditional love and support and to Sheila Powell (soon to be Sheila Le Blanc) for her loving support and motivation during the completion of this work.

A special thanks to my research supervisor Mike Blades for giving me the freedom and guidance to pursue the research I chose. Thanks also to my fellow graduate students for their camaraderie.

Acknowledgment goes to Aurora Instruments Ltd., Vancouver, British Columbia, for the GF-CCP-100 used in this study and for their technical support. Acknowledgment is also made to the Science Council of British Columbia's G.R.E.A.T. program and to the Natural Science and Engineering Research Council of Canada (NSERC) for financial support.

CHAPTER 1

INTRODUCTION

“What light through yonder window breaks?”

W. Shakespeare

1.1 FAPES

Furnace atomization plasma excitation spectrometry (FAPES) is a relatively new atomic emission elemental analysis technique [1-24] that has been shown to have detection limits comparable to graphite furnace atomic absorption spectrometry (GFAAS) [2-6, 8, 9, 18]. In FAPES, the emission source consists of a conventional atomic absorption graphite cuvette together with an electrode placed coaxially within this cuvette, as shown in Fig. 1.1. Upon heating, the graphite cuvette acts as a desolvator and atomizer for solid or liquid samples as in graphite furnace atomic absorption spectrometry. A radio frequency (r.f.) potential is applied to the central electrode and generates an atmospheric pressure helium or argon plasma within the cuvette. This plasma acts as an excitation medium for atoms.

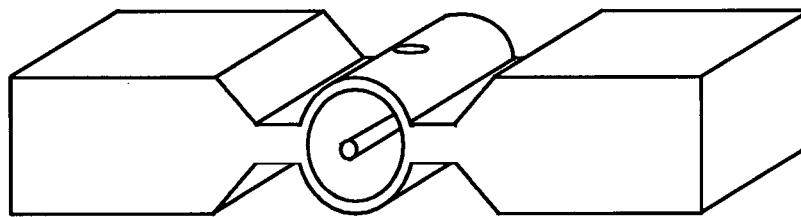


Fig. 1.1 FAPES graphite cuvette and center electrode configuration.

1.2 Thesis Objective

Since FAPES is a relatively new analytical atomic emission source [1, 2], very little is known about how instrumental parameters influence its spatial structure. Most spectroscopic studies reported thus far have either been done by looking at a fairly large portion of the plasma or by looking at only one section of it. While these yield valuable information, a more complete understanding of the source requires studying the spatial distribution of species within the plasma and how these distributions are affected by the experimental parameters. Gaining some information on the plasma's spatial characteristics will ultimately help to determine and optimize the analytical zone of this source, in both physical and operating parameter space. More importantly, spatially resolved studies in this emission source will help in understanding the character of the plasma. The studies reported in this thesis were designed to gain such spatial information.

1.3 Development of the FAPES and Related Sources

1.3.1 A Brief Historical Background

Optical emission sources have been used as analytical tools since Bunsen and Kirchhoff's laboratory flame experiments [25] in the mid 1800's. A few decades later, in 1882, Hartley [26] made the first spectroscopic quantitative analysis by measuring the amount of beryllium in certain compounds using a "condensed spark" optical emission source.

Following Walsh's classic paper [27] on atomic absorption spectrometry (AAS), the laboratory flame began to be used as a vaporization and atomization device for AAS. The introduction of the graphite furnace by B. L'vov [28] improved the sensitivity of AAS significantly and graphite furnace atomic absorption spectrometry is currently one of the most sensitive atomic spectrometric methods available for trace metal analysis due mainly to its near 100% atomization efficiency [29]. While recent advances in continuum source AAS [30-32] give this technique the ability to perform simultaneous multi-elemental analysis, GFAAS still remains mainly a technique used for the analysis of one element at a time. Optical emission sources are not limited to this restriction and can be used to perform routine simultaneous multi-elemental analysis.

Aside from laboratory flames and laser induced plasmas, current optical emission sources rely mainly on electrical discharges creating plasmas to excite the analyte species. These have evolved in several directions ranging from the three electrode direct current plasma (DCP) to the current workhorse of trace elemental analysis, the inductively coupled plasma (ICP). A thorough discussion

of optical emission sources used for quantitative analysis is beyond the scope of this introduction and can be found in review papers by Blades *et al.* [33] and Broekaert [34].

1.3.2 Plasma Optical Emission Sources

A plasma is a partially ionized gas with an approximately equal number of positive and negative charges and is composed primarily of neutral atoms, atomic ions, and unbound or free electrons. If a gas is given enough thermal energy, the molecules and atoms in the gas may become ionized as a result of their collisions. The properties of the gas may then be dominated by the effect of electromagnetic forces acting on these charged particles. Such a gas is called a plasma. Plasmas are therefore high temperature ionized gasses which necessarily contain excited species. These excited species may undergo radiative deexcitation. The radiation emitted by this process is used as the basis of spectrometric analysis. A more complete description of plasmas in general can be found elsewhere [35]. Optical emission sources based on electrical discharges using this phenomena include inductively coupled plasmas (ICP), direct current plasmas (DCP), microwave induced plasmas (MIP), glow discharges (GD), sparks and exploding films. These differ in both their geometry and the frequency of the applied electric fields. The geometry of these sources varies from electrodes in direct contact with the plasma, as in the DCP, to induction coils separated from the plasma by glass torches, as in the ICP. The frequencies of the applied field varies between the direct currents applied to the DCP and GD to the gigahertz frequency currents applied to the MIP.

1.3.3 Emission Sources Based on Graphite Furnaces

The use of a graphite furnace as an emission source provides the possibility of using the high atomization efficiency of the graphite furnace combined with the inherent multi-elemental capabilities of an optical emission source. Four techniques have been designed to utilize optical emission from within graphite furnaces: graphite furnace atomic emission spectrometry (GFAES), hollow cathode furnace atomization non-thermal excitation spectrometry (HC-FANES), hollow anode furnace atomization non-thermal excitation spectrometry (HA-FANES), and the FAPES source described in this thesis.

The first published attempts at using a graphite furnace for optical emission spectrochemical analysis were by Molnar *et al.* [36] and by Ottaway and Shaw [37] in 1975. In GFAES the high temperature graphite cuvette provides the energy that excites the analyte atoms from which optical emission is measured. Baxter and Frech have recently written an extensive review of GFAES [38]. Baxter [39] has shown that the best emission results using GFAES could be obtained by using a graphite cuvette that was both spatially and temporally isothermal. A two-step furnace with an transversely heated graphite cuvette, shown in Fig. 1.2, provided these conditions. This configuration provided the highest emission efficiencies, approaching 100%, as all the atoms within the cuvette are heated up to the cuvette temperature.

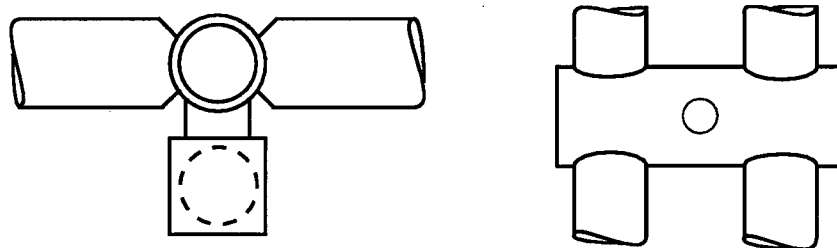


Fig. 1.2: Atomizer configuration for two-step furnace. Dashed line in end view (left) represents the position of the atomizer cup contact electrode. Center circle on top view (right) represents hole between atomizer cup and excitation cuvette. Adapted from Baxter [39].

Since the graphite furnace atomizer is at local thermal equilibrium under the conditions normally used for analysis [40], the intensities of the emission lines are dependent on the atomization temperature used and can be calculated using the Boltzmann equation as discussed below. In GFAES, these excitation temperatures have been found to be roughly equal to the tube wall temperature during atomization [41]. This temperature, normally around 2500 K, limits the usefulness of GFAES to those elements that have relatively low excitation energies of up to approximately 2 eV. Increasing the furnace temperature to increase the atomic emission intensities also increases the blackbody emission from the graphite cuvette thus no improvement in detection limits are seen [42]. In order to increase the excitation energy of the analyte atoms in the graphite furnace without increasing the background, non-thermal excitation methods have been developed using graphite furnace cuvettes as electrodes in electrical discharges.

The first implementation of a furnace atomization non-thermal excitation spectrometry (FANES) source was by Falk *et al.* [43-46] who used the graphite

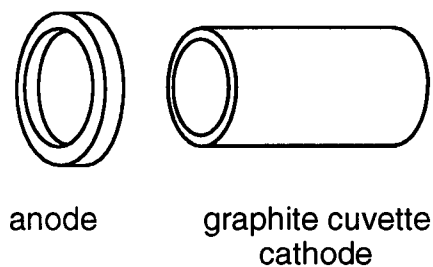


Fig. 1.3: Hollow cathode furnace atomization non-thermal excitation spectrometry (HC-FANES) source configuration. Adapter from Falk *et al.* [42].

cuvette of a conventional furnace atomizer as the cathode in a low pressure discharge with the geometry shown in Fig. 1.3. This HC-FANES source has been used successfully in atomic emission analysis and compares favorably with GFAAS [47]. The use of HC-FANES for molecular emission has also been investigated with some degree of success [48]. Falk *et al.* [42] have written an in depth review of HC-FANES and concluded that the principal advantages of HC-FANES over GFAAS are its inherent multielement capabilities and the extension of the range of elements, which includes the halogens, that can be analyzed.

Ballou *et al.* [49] first described the use of the graphite cuvette as the anode in their design of a HA-FANES source. In this source, a thin graphite electrode was placed coaxially within the graphite cuvette and served as the cathode, as in the FAPES geometry shown in Fig. 1.1. By using the furnace as the anode it was not necessary to electrically shield the furnace as required in HC-FANES [50]. The HA-FANES source was found to have a lower excitation

ability when compared to the HC-FANES but could be operated at pressures of up to an order of magnitude higher thus integrated emission intensities were about the same. Very little has been reported on the use of this source [49-52] but detection limits were found to be on the same order as those for HC-FANES [51].

Liang and Blades [1] and Sturgeon *et al.* [2] described the first designs of an atmospheric pressure r.f. plasma source inside the cuvette of a graphite furnace atomizer. This is currently referred to as a furnace atomization plasma excitation spectrometry (FAPES) source. Their designs were based on the geometry of the HA-FANES source but in this case r.f. power was applied to the central electrode which allowed atmospheric pressure operation. This simplified sample handling compared to the HC-FANES and HA-FANES which require low pressure operation and was also expected to increase the residence time of the analytes in the source. A more detailed description of this FAPES source can be found in the experimental chapter of this thesis.

1.4 Electrical Discharges in Gases

Atmospheric pressure electric discharges are observed regularly every day and can be as small as the static electric discharge you get from touching someone else after walking on a rug and as large as a lightning strike. These have in common the fact that the electrical potential difference between the electrodes has reached a critical value, called the breakdown potential, where the gas becomes a conductor. This breakdown potential is dependent on the separation, geometry, and composition of the electrodes, the composition and pressure of the gas between them and the frequency of the applied electric field.

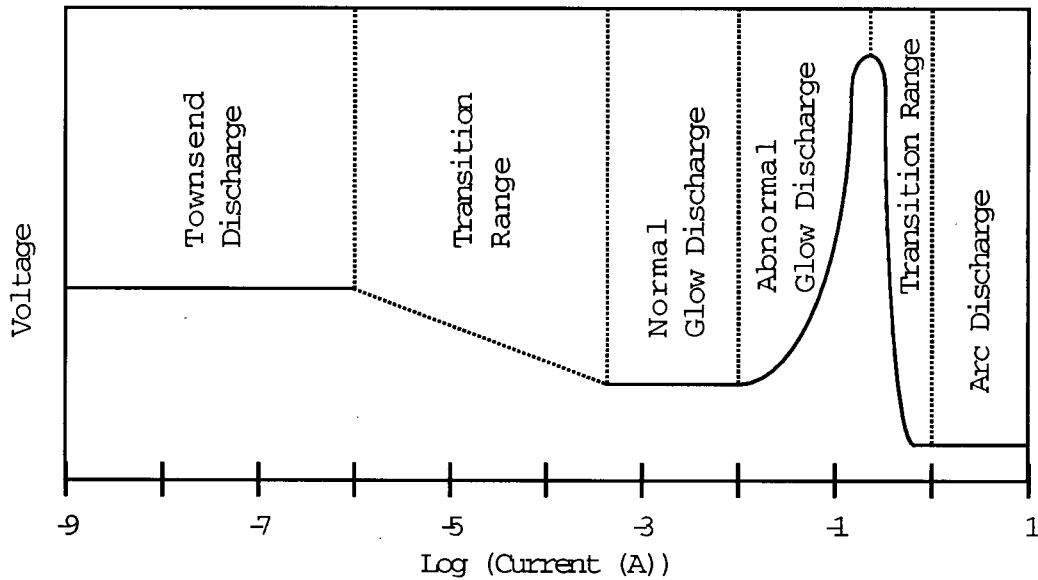


Fig. 1.4: Voltage-current plot for various gas-discharges. Adapted from Fang and Marcus [53].

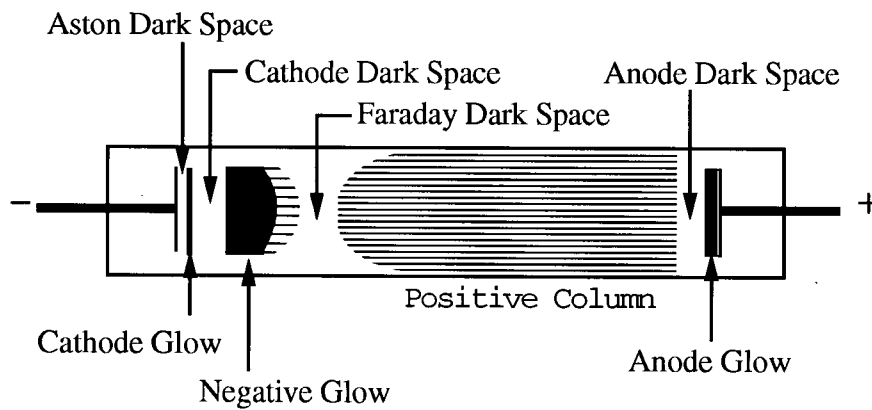


Fig. 1.5: Schematic illustration of a direct current electrical discharge at reduced pressure. Shaded areas represent luminous areas. Adapted from Chapman [56].

Detailed discussions of electric discharges can be found elsewhere [53-57] and are discussed here only as they help in understanding the FAPES source. For this discussion, direct current (d.c.) discharges are considered first since Schwab *et al.* [58-61] and Hotz [62] have shown that r.f. discharges between electrodes in gasses occur similarly to d.c. discharges with the cathode glow shifting from one electrode to the other in alternating half cycles.

Direct current electrical discharges in gasses can be classified by looking at their voltage-current characteristics as shown in Fig. 1.4. At low powers, a Townsend discharge occurs which is not usually visible to the naked eye. As the current is increased there is a transition to a lower voltage and the discharge becomes visible to the eye. This is the onset of the normal glow discharge. In the normal glow discharge, an increase in the current does not change the potential difference between the electrodes or the current density at the cathode but instead the cathode area covered by the discharge increases. Once the cathode is fully covered, an increase in current results in an increase in the voltage. This region is called the abnormal glow discharge. A further increase in current causes an arc to form with a coincident drop in voltage.

The spatial structure of a glow discharge, first observed by Michael Faraday in the 1830's [54], is shown in Fig. 1.5. It consists essentially of a series of light and dark spaces, historically given names, between the electrodes. Moving from the cathode to the electrode in this figure, there is first the Aston dark space adjacent to the cathode. Here electrons have insufficient energy to excite gas atoms. As the electrons gain enough energy to excite gas atoms the cathode glow appears. In the cathode glow, positive ions accelerated towards the cathode also have sufficient energy to excite gas atoms. As the electrons are

accelerated further away from the cathode they become quite energetic and undergo few collisions. This results in the cathode dark space where the majority of the discharge potential drops. The negative glow is the brightest zone in the discharge and where electrons, having lost some energy in the cathode dark space, excite and ionize gas atoms most efficiently. Adjacent to the negative glow is the Faraday dark space where electrons have insufficient energy to excite or ionize gas atoms. The positive column most closely resembles a plasma in that it is quasi-neutral with an approximately equal number of positive and negative charge carriers which can excite gas atoms. Near the anode, electrons are accelerated and thus the anode dark space and anode glow occur similarly to the Aston dark space and cathode glow.

It should be noted that all of these dark spaces and glows are not present in all glow discharge configurations. Notably, the Aston and anode dark spaces and the cathode and anode glows are not usually observed in typical glow discharge operation. If the electrodes are brought together, the negative glow retains its size but the positive column shrinks. If the pressure of the discharge is increased, the thickness of the cathode dark space decreases and eventually the negative glow essentially comes in contact with the cathode.

1.5 Fundamental Properties of Spectrochemical Plasmas and their Measurement

The FAPES source consists of a r.f. plasma within the atomization cuvette of a graphite furnace atomizer and as such can be studied using plasma diagnostic techniques. The following are brief descriptions of the more important analytical plasma characteristics and their measurement. More complete information on plasma diagnostics can be found elsewhere [63-65].

1.5.1 Atom and Ion Populations

Atom and ion populations within spectrochemical optical emission sources are not usually spatially homogeneous [66] due to the geometry of the source. Measurement of their spatial distributions yields valuable information from both fundamental and analytical perspectives. Knowledge of the atom and ion distributions within spectrochemical sources can be used to gain information on the ability of the source to atomize and ionize analyte species. This knowledge can be used to better understand the processes and mechanisms of atom and ion formation in the source and gives insight into the source's energy distribution. Knowledge of these spatial distributions is also important for the analyst as they help determine where in the source the analytical observation should take place. Population distributions of atoms and ions can be calculated by measuring spatially resolved absorption, emission, or fluorescence.

1.5.2 Electron Number Densities

Another important characteristic of spectrochemical plasmas is the electron number density. In these plasmas, reactions with analytes are usually dominated by charge exchange reactions which can most easily be related to the electron (or ion) density since these are the primary excitation agents [67]. Electron number density measurements in spectrochemical plasmas are usually calculated from the Stark broadening of the $H\beta$ line or from the background continuum intensity. A description of these techniques can be found elsewhere [68].

1.5.3 Temperature Measurements

One of the most important characteristics of a spectrochemical optical emission source is its temperature. The reason is that higher temperatures make sources able to atomize fairly robust molecules, thus reducing matrix interferences, and also produce strong atomic excitation resulting in intense emission lines. Most analytical spectrochemical sources such as plasmas do not exhibit a unique temperature. The spectral intensity does not follow the Planck blackbody distribution [69] and different temperatures, that are not usually equal to each other in these plasmas, are defined which describe the velocity or state distribution of specific particles in the source. Some of these temperatures are the electron, gas kinetic, excitation and ionization temperatures [70]. Experimental techniques have been designed to measure each of these temperatures and are described by Thorne [69] and by Mermet [68]. In this thesis, two types of excitation temperatures were measured: atomic excitation temperatures and molecular rotational excitation temperatures, usually called simply the excitation temperatures and the rotational temperatures respectively.

There are two techniques commonly used to measure the excitation temperatures in spectrochemical sources; the Boltzmann plot and the line pair intensity ratio methods [68]. Both techniques assume that the populations of the species in the excited state follow the Boltzmann distribution. Thus the population N of the excited state k or N_k is given by

$$N_k = \frac{N_0 g_k}{U(T_{exc})} e^{-(E_k/k_B T_{exc})} \quad (1.1)$$

where N_0 is the total number density of the species under study. E_k is the excitation energy and g_k is the statistical weight (equal to $2J_k+1$ where J_k is the total angular momentum quantum number) of the state k . U is the partition

function or sum over states. T_{exc} is the excitation temperature and k_B is the Boltzmann constant. The total intensity, I_{ki} , of a spectral line of wavelength λ_{ik} in a optically thin, homogeneous layer of length l is given by

$$I_{ki} = \frac{A_{ki} N_k h c l}{4\pi\lambda_{ik}} \quad (1.2)$$

where A_{ki} is the transition probability, h is the Planck constant, and c is the speed of light. Combining equations 1.1 and 1.2, simplifying and converting to natural logarithms yields

$$\ln \frac{I_{ki} \lambda_{ik}}{g_k A_{ki}} = \frac{-E_k}{k_B T_{exc}} + \ln C \quad (1.3)$$

Both the Boltzmann plot and the line pair intensity ratio methods use equation 1.3 to calculate T_{exc} from the relative intensity of emission lines. In the Boltzmann plot method a plot of $\ln (I_{ki} \lambda_{ik} / g_k A_{ki})$ versus E_k yields a straight line with a slope of $-1/k_B T_{exc}$. For rotational temperatures of molecules, T_{rot} , the same equations are used though the appropriate statistical weights replace g_k . Detailed derivations from equation 1.3 for rotational temperature calculations are beyond the scope of this thesis and can be found elsewhere [68, 70]. Ishii and Montaser [71] have also published a useful tutorial on these calculations. In the line pair intensity ratio method, the emission intensity from two lines is measured then equation 1.3 is applied. With only two lines this equation is commonly simplified to

$$T_{exc} = \frac{k(E_1 - E_2)}{\ln \frac{g_1 A_1 \lambda_2}{g_2 A_2 \lambda_1} - \ln \frac{I_1}{I_2}} \quad (1.4)$$

where I_1 and I_2 are the intensities of the two emission lines.

1.6 A Survey of FAPES Research

FAPES research is currently being published by three research groups. One headed by D. C. Liang (Aurora Instruments Ltd., Vancouver B.C.) [9, 13, 14], a second headed by R. E. Sturgeon (National Research Council of Canada, Ottawa Ont.) [2, 4-8, 12, 17-22], and this laboratory headed by M. W. Blades (University of British Columbia, Vancouver B.C.) [1, 3, 9-11, 16, 24]. While Ali [72] described the status of FAPES as embryonic in 1991, it has definitely been born by now with a commercial FAPES source currently available (Aurora Instruments Ltd., Vancouver B.C.). FAPES is however still in its infancy with less than 25 papers published on the subject.

Since the first publications on the FAPES source [1, 2] several papers [3-6, 8, 13, 17, 18] have reported some analytical figures of merit. The linear dynamic range of the FAPES source has been found to be approximately 4 orders of magnitude [3, 5, 11] with detection limits on the order of picograms and precisions of roughly 5% [5, 6]. Table 1.1 lists the lowest detection limits reported thus far in the FAPES source. In this table, the results are for the intensities calculated from emission peak heights, unless otherwise noted, as these have been found to give slightly better detection limits.

Increases in the frequency of the applied r.f. power to the center electrode were shown to increase the sensitivity but did not improve detection limits as the noise in the background also increased [8]. A FAPES instrument manufacturer (Aurora Instruments Ltd., Vancouver, B.C.) has reported that using argon as the plasma gas increases the signal-to-noise ratio as compared to helium but presented no specific data on the magnitude of this effect [13]. The use of L'vov platforms and palladium modifiers was also investigated and found to improve

Element	Detection Limit (pg) (As $3\sigma_B$)	Comments	Reference
Ag	0.3		[3]
Al	5.5	Two-step furnace	[17]
As	1.3		[8]
B	276	Bias controlled at 0 V	[18]
Be	5.0		[5]
Bi	25		[5]
Cd	0.6	Bias controlled at 0 V	[18]
Cr	17	2-step furnace	[17]
Cu	0.86		[8]
Fe	0.4	In Ar	[8]
Mn	0.90	Pd modifier and platform	[6]
Ni	8.6	In Ar	[8]
P	29	Manufacturer	[9]
Pb	7.2	Pd modifier and platform	[6]
Pt	53	Area, Bias = 0 V	[18]
S	1100	CS molecule, Bias = -11 V	[18]
Sb	16	Manufacturer	[9]
Se	110	Manufacturer	[9]
Sn	6.1	2-step furnace	[17]
Te	61	Manufacturer	[9]
Tl	5	Manufacturer	[9]
Zn	1.8	Manufacturer	[9]

Table 1.1 Lowest FAPES detection limits reported thus far. Values are calculated as three time the standard deviation of the background ($3\sigma_B$). Values are for helium plasmas unless otherwise indicated.

the stability of the plasma [6] as did control of the bias potential on the center electrode [18]. A two step furnace, where analyte samples were atomized into a constant temperature chamber containing the plasma, was designed and found to have good detection limits [17]. Controlled pressure studies [21] showed that the best results could be obtained at pressures slightly above atmospheric.

Fundamental characterization studies have been performed to help better understand the nature of the FAPES plasma [6-8, 10, 12, 16, 19, 20, 22, 24]. Excitation temperatures have been measured using emission intensities from He(I), Fe(I) and Fe(II) lines and range between 2920 K and 7600 K depending on the thermometric species, the emission lines chosen, and the magnitude and frequency of the r.f. power applied to the center electrode [7, 8, 10, 24]. These excitation temperatures were found to be independent of the atomizer tube wall temperature and are discussed in more detail in Chapter 3. A translation temperature based on the Doppler broadening of a Be(I) line was measured to be 7030 ± 1150 K and also found to be independent of the tube wall temperature [7]. Electron number densities were calculated from the Stark broadening of the $H\beta$ line as 9.6, 8.1, and $6.7 \times 10^{13} \text{ cm}^{-3}$ with 100, 75, and 50 Watts r.f. power applied to the center electrode respectively.

The effect of easily ionizable elements (EIE) in sample matrices was investigated in several studies [6, 15, 19]. These showed that the presence of an EIE could attenuate the analytical signal in the FAPES source however this effect could be decreased if the r.f. power was increased [6]. The cause of the EIE's effect on the analytical signal was attributed to a loss of power radiated from the plasma by excited matrix vapor components and an alteration in the electron energy distribution function by the injection of low energy electrons from

ionization of the EIE. Non-spectral interferences were found to change the analytical signal's intensity and temporal behavior [16, 20]. These were concluded to be caused by the formation of volatile compounds which vaporized prior to the appearance temperature of the analytes. Under certain conditions the center electrode was seen to act as a condensation site with analyte atoms vaporized from the cuvette wall condensing on the center electrode then revaporizing later in the atomization cycle [11, 20].

1.7 Thesis Overview

This thesis describes spatially, spectrally and temporally resolved emission studies in the FAPES source. An improved understanding of the effects of operating parameters on the ability of the FAPES source to excite analyte atoms will help in their optimization for routine analysis. Since one of the main parameters of the FAPES source is the r.f. power applied to the center electrode, most of the studies reported in this thesis show the effect of varying this r.f. power on various plasma characteristics. Hopefully these should give a clearer understanding of this relatively new atomic emission analytical source.

Chapter 3 describes the results from spatially resolved temperature measurements. These include profiles of He(I), N_2^+ , OH, and Pb(I) emission line intensities as well as rotational and excitation temperature measurements. In the studies reported in Chapter 4, indium was used as a spectrometric species to investigate the spatial and temporal profile of analyte in the FAPES source with different r.f. powers applied to the center electrode. Since these results showed that atomic emission intensities do not continue to increase with r.f. power, it was suspected that analyte ionization occurred at these higher r.f. powers. In

Chapter 5, the results of analyte ionization studies are shown. Here magnesium was used as the spectrometric species. The results showed that analyte atoms are indeed ionized in the FAPES source and the degree of ionization is dependent on both the spatial position within the source and the intensity of the r.f. power applied to the center electrode. A clearer understanding of the plasma in the FAPES source was gained by looking at the effect of reducing the pressure inside the source on the emission's spatial structure. The results of these reduced pressure emission measurements are shown in Chapter 6 and suggest that the FAPES source is essentially an atmospheric pressure radio frequency glow discharge with a coaxial geometry. Chapter 7 brings together a variety of additional data and observations that add insight into the character of the FAPES source.

CHAPTER 2

EXPERIMENTAL

“The principle of science, the definition, almost, is the following: The test of all knowledge is experiment. Experiment is the sole judge of scientific truth.”

R. P. Feynman [73]

2.1 The Experimental System

The experimental system used in the studies reported in this thesis was designed to conduct spectroscopic diagnostics in the FAPES source. Specifically, the detection system was designed to measure spatially, temporally, and spectrally resolved emission from the FAPES source simultaneously. Fig. 2.1 is a schematic illustration of this experimental system which consisted of a FAPES source coupled with an optical emission spectrometry measurement system. Instrumentation to allow measuring atomic absorption and reduced pressure operation were also included in the experimental set-up.

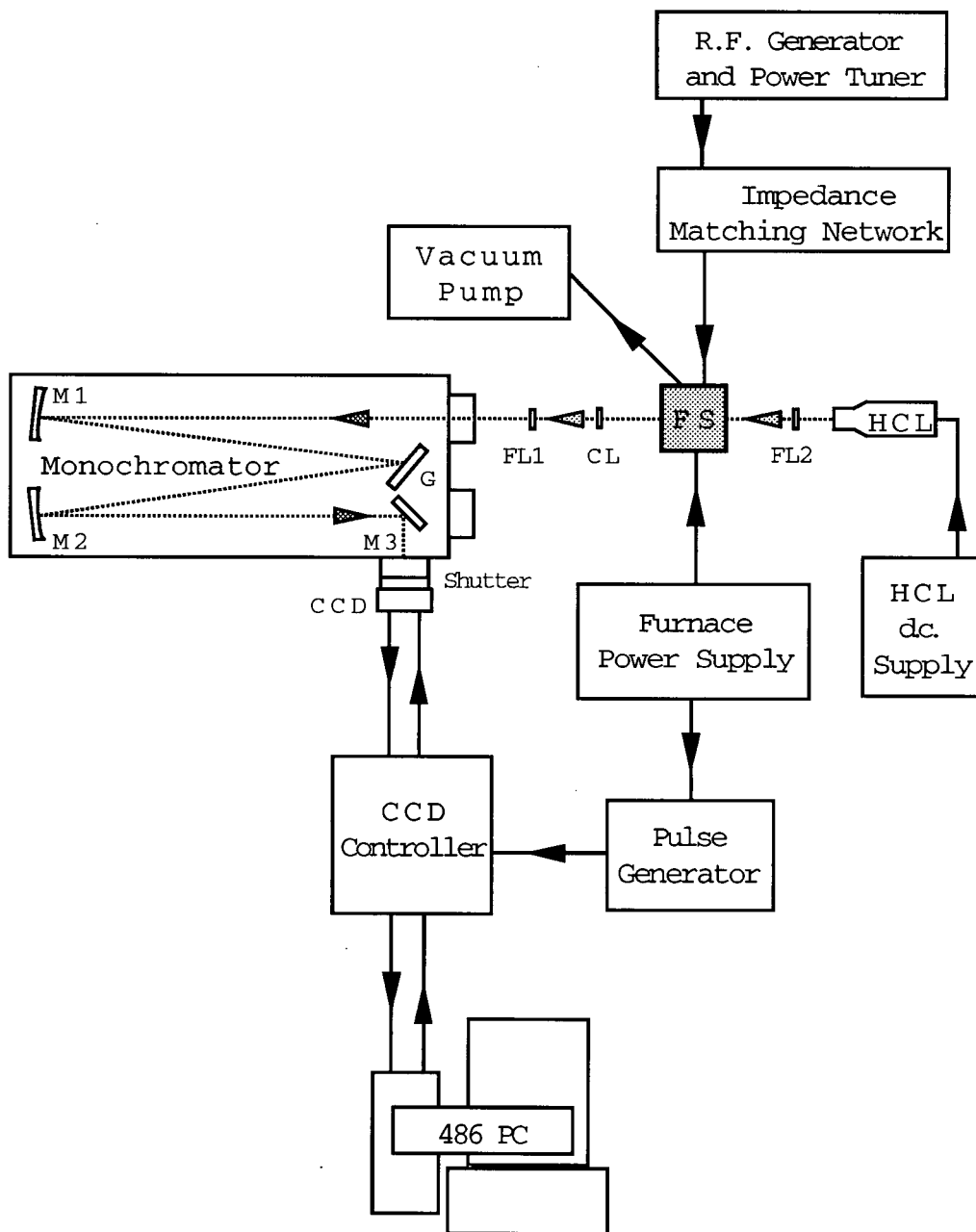


Fig. 2.1: Schematic diagram of the experimental setup.

2.1.1 The FAPES Sources

Two FAPES work-heads were used throughout this research, a model GF-CCP-100 prototype FAPES work-head built by Aurora Instruments, Ltd. (Vancouver, B.C., Canada), shown in Fig. 2.2, and one built in-house, shown in Fig. 2.3. Both FAPES work-heads consisted of a pyrolytic-graphite coated integrated contact cuvette (Fig. 1.1) with a pyrolytic-coated coaxial center electrode (Ringsdorff-Werke, Bad Goesberg, Germany) contained within a water cooled aluminum box with quartz optical windows. The cuvettes used contained a 19 mm long cylindrical atomization chamber with an internal diameter of 5.7 mm and a wall thickness of 0.75 mm. They also had a 2.0 mm diameter sample dosing hole through the top center of the atomization chamber. The coaxial center electrode had a diameter of 0.9 mm and extended from an electrode holder, electrically insulated from the aluminum box, through the full length of the cuvette and beyond the front of the cuvette by 1 mm.

In each source, the cuvette was resistively heated by a direct current applied to the clamp electrodes holding it in place. A helium plasma was created in the volume of the cuvette by applying a r.f. potential to the center electrode. In both sources, r.f. power was supplied by a 13.56 MHz. r.f. generator using an automatic power tuner and an impedance matching network (Models RFX-600, ATX-600 and 5017-000-G respectively, Advanced Energy, Fort Collins, CO, USA).

Helium was chosen as the plasma gas as this provided a more stable plasma under the conditions used [74]. Specifically, the use of helium as the plasma gas allowed the operation of the FAPES source over a wide range of r.f. powers and at pressures from a few mmHg to atmospheric pressure. The helium

gas (Union Carbide, Toronto, Ont., Canada) was supplied to the FAPES source from a pressurized cylinder. The helium flow rate was regulated by a servo-controlled needle valve in the GF-CCP-100 prototype and was kept at 1.5 L/min. throughout the heating cycle except during the atomization cycle at which time the helium flow was turned off. The helium flow rate in the Cube source built in-house was also turned off during the atomization cycle and was otherwise kept at 4 SCFH (standard cubic feet per hour) as indicated on the graphite furnace supply described below.

2.1.1.1 The GF-CCP-100 Source

The FAPES source from Aurora Instruments Ltd. used in this study was a GF-CCP-100 prototype. This source's 27.12 MHz. r.f. power supply was not used since there was no technique to monitor the r.f. power level available and most of the studies conducted used the r.f. power level as a significant parameter. The prototype's work-head and temperature control systems were used together with the 13.56 MHz. Advanced Energy r.f. power supply. It should be noted that some instrumental details of the GF-CCP-100 prototype are considered proprietary information by Aurora Instruments Ltd. and are not included in the following description of the source.

The work-head, shown in Fig. 2.2, consisted of a water cooled aluminum box 120 mm square and 6.25 mm thick. Optical emission from the source was viewed through a 16 mm diameter quartz optical window on the front end. The top of the aluminum box was fastened to the lower portion of the box using four corner screws. An inverted cone made of titanium containing a 2 mm diameter

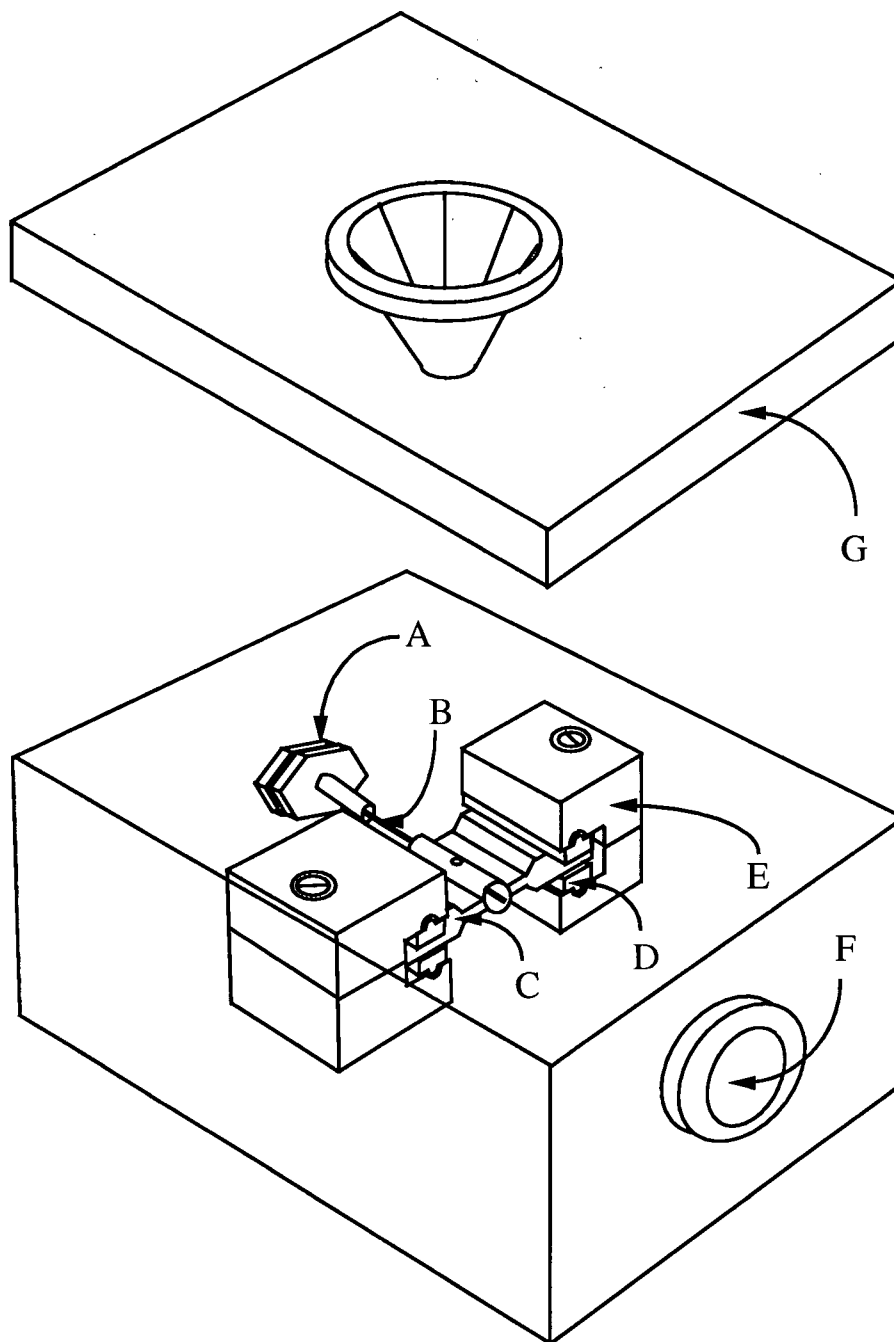


Fig. 2.2: The GF-CCP-100 prototype FAPES source work-head.
A) R.F. Connector; B) Graphite Electrode; C) Graphite Cuvette;
D) Copper D.C. Contact; E) Copper D.C. Electrode; F) Quartz Window;
G) Workhead Lid

sample dosing hole was fastened to a 50 mm port through the top of the box. "O"-rings were used on all ports and between the box top and lower body.

The graphite cuvette was held in place by two copper contacts on each side which were squeezed onto the cuvette by copper clamping electrodes. These electrodes were water cooled and delivered the direct current to the graphite cuvette. The top and bottom of these clamps were held together by spring loaded screws to insure a good electrical contact between the electrodes and the cuvette. A r.f. feed-through machined with a center electrode holder was located at the back of the aluminum box. Plasma gas, in this case helium, was fed into the box through an 80 mm long, 7 mm inside diameter brass tube secured to a hole at the bottom center of box. An optical sensor was positioned in the center of this hole and focused at the bottom of the graphite cuvette. The furnace temperature was computer controlled *via* a feedback loop from this optical sensor allowing the software to adjust the current supplied to the clamping electrodes.

2.1.1.2 The Cube Source

The FAPES work-head built in-house, shown in Fig. 2.3, consisted of a hollow 6 inch aluminum cube with 5 inch ports on each side. The design of this work-head was based on the description by Ballou *et al.* [49] of their hollow anode FANES source. The 5 inch ports were each fitted with an "O"-ring sealed aluminum flange. The entire cube was mounted on a mechanical translation stage connected to the bottom flange which allowed movement along one horizontal axis. The graphite cuvette support structure, direct current electrodes, plasma gas, and cooling water were connected through one of the vertical

aluminum flanges. A vertical post on one of the cube's top corner was used to mount an optical pyrometer.

The graphite cuvette support structure consisted of copper electrodes and some MacorTM used to make the structure stable. It allowed cooling water to pass inside the copper electrodes which were used to supply the direct current to the graphite cuvette. The r.f. electrode was held in place by a clamp connected to a r.f. feed-through on the flange opposite the one holding the graphite cuvette support structure. A small gas outlet port was machined at the center of this flange thus the plasma gas did not flow directly through the graphite cuvette. There were 1 inch quartz windows at the center of each of the three remaining flanges. The optical emission was viewed through one of the side quartz windows and absorption measurements were made by passing light through the source *via* the two side windows. The top flange, besides containing a viewing port, also had a sample injection port, shown in Fig. 2.3, with a screw-on cap.

The graphite cuvette temperature was controlled by a graphite furnace power supply (Model IL-655, formerly Instrumentation Laboratory; now Thermo-Jarrell Ash, Waltman, MA, USA) and was monitored with an optical pyrometer (Model 11 X 30, Series 1100, Iacon Inc., IL, USA). The optical pyrometer was focused on the outside wall of the cylindrical portion of the graphite cuvette through the top quartz window and measured the radiation emitted by the graphite cuvette during the atomization cycle. The pyrometer output was simply recorded on a chart recorder and atomization temperatures were interpolated from a calibration plot provided by the pyrometer manufacturer.

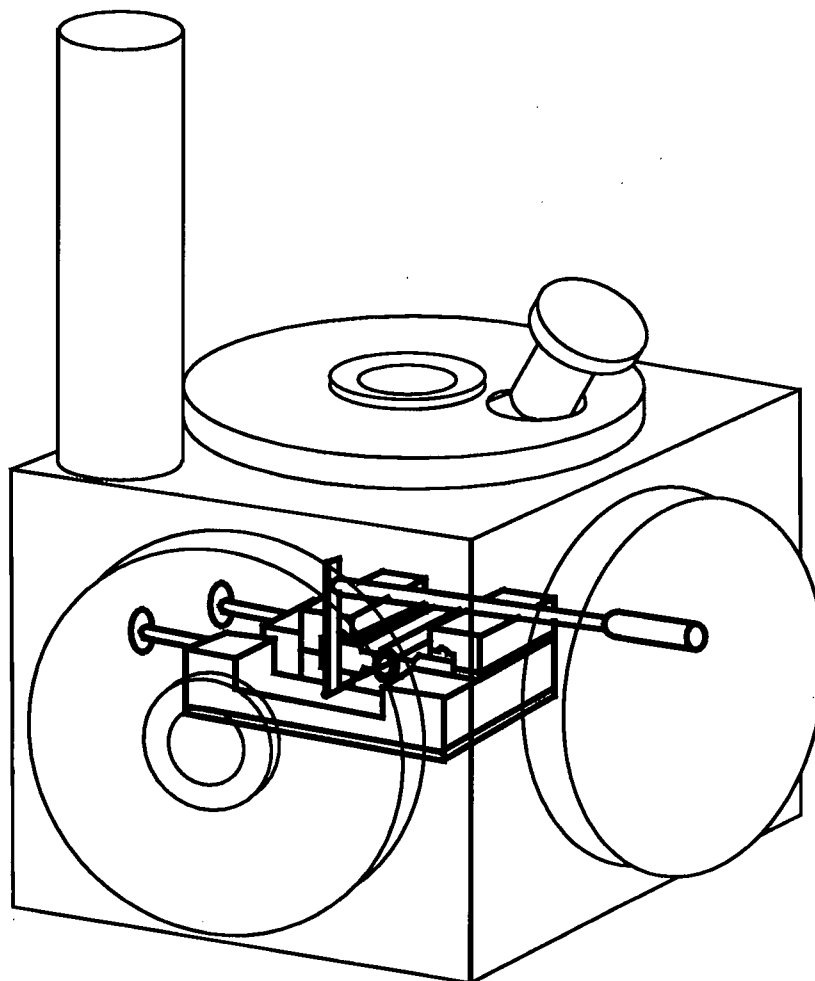


Fig. 2.3: The Cube FAPES source work-head.

2.1.2 Detection System

The studies reported in this thesis required a detection system that could view the FAPES source and obtain spatial, temporal and spectral information simultaneously. The detection system chosen focused analytically useful light, either from plasma emission or from a hollow cathode lamp, onto the entrance slit of a monochromator. The monochromator spectrally resolved this light and

focused it onto a two dimensional CCD detector. This configuration , described in more detail below, fulfilled the requirements.

2.1.2.1 Optical Configuration

Measurement of optical emission and absorption requires the use of light steering optics between the source and the light sensitive detector. This usually takes the form of one or more lenses which focus the spectroscopic light onto the entrance slit of a monochromator. Many lens configurations fulfill this requirement and each have both advantages and disadvantages. For this experimental system it was necessary to use lenses that transmitted ultraviolet light since many of the measurements made in these studies were at wavelengths in the ultraviolet region of the electromagnetic spectrum. Lenses made of fused silica were chosen for this purpose. A helium-neon laser (Melles Griot, Carlsbad, CA, U.S.A.) was used to help in the alignment of all the optical components including the positioning of the FAPES source with respect to the monochromator.

For the spectroscopic temperature measurements described in Chapter 3, the emission from the FAPES source was imaged at 1:1 onto the entrance slit of the monochromator with a 50 mm focal length fused silica biconvex lens which replaced the lenses CL and FL1 in Fig. 2.1. The optical specifications for those studies are given in more detail in the experimental section of that chapter. For the studies reported in the other chapters, a two lens system was chosen to focus the light from the FAPES source onto the entrance slit of the monochromator. This simplified the experimental reconfiguration needed when changing the observed wavelength. The focal length of a lens is dependent on

its index of refraction which is a function of wavelength [75]. By using a collimating lens and a focusing lens, when the wavelength observed was changed, refocusing could be done by simply moving the two lenses. A single lens used for this purpose would have required moving either the monochromator or the source to keep the source focused onto the monochromator when the wavelength observed was changed. It would also have been necessary to move the lens if a constant magnification was desired.

Farnsworth *et al.* [76] have conducted ray tracing computer calculations of the light collection efficiency for several commonly used lens configurations for a system geometrically similar to the FAPES source. The optimum configuration for a two lens system was found to consist of two plano-convex lenses with their curved surfaces facing each other. For the studies reported in Chapters 4 to 6, a collimating lens with a focal length of 250 mm, CL in Fig. 2.1, was used to collimate the light from the FAPES source. A focusing lens with a focal length of 150 mm, FL in Fig. 2.1, was used to focus this collimated light onto the entrance slit of the monochromator.

Spatial resolution was obtained by placing an aperture on either the collimating lens on the two lens imaging system or on the imaging biconvex lens in the one lens system. Details of the spatial resolution obtained are discussed in more detail in the experimental sections of the appropriate chapters.

2.1.2.2 The Monochromator and CCD Detector

A 1 metre Czerny-Turner monochromator (Model 2061 Scoeffel-McPherson, Acton, MA, U.S.A.) was used to spectrally resolve the light from the

FAPES source. Holographic gratings (Scoeffel-McPherson, Acton, MA, U.S.A.) with 3600 and 1200 lines/mm were used interchangeably in the monochromator. The choice of grating used was dictated by the spectral resolution necessary to resolve the emission lines and the spectral width observed by the detector since most studies involved the measurement of several spectral lines simultaneously.

A CCD detector was mounted at the exit plane of the monochromator using a coupling ring built in-house. The CCD used was a thermoelectrically cooled 1024 by 256 pixel CCD (Model TE/CCD-1024EMUV1, Princeton Instruments, Inc., Trenton, NJ, U.S.A.) cooled to -50°C with the long CCD axis positioned horizontally. In this configuration it was possible to obtain both spectral and spatial information simultaneously. The emission from the source was spectrally dispersed by the monochromator along the horizontal dimension while the vertical dimension preserved the spatial information namely, the emission intensity of a vertical slice through the center of the source. This CCD system came equipped with a software controlled electronic shutter that provided the temporal resolution required in these studies.

The CCD detector pixels had $27\ \mu\text{m}$ centers which was more than adequate for obtaining the spatial resolution defined by the imaging system. With the CCD system used it was possible to hardware sum, or bin, CCD pixels together in order to decrease the data transfer time and the size of the data files created by the CCD controlling software. The binning used in the data collection described in the experimental sections of the following chapters created super pixels whose size was the total area of the pixels binned together. The data acquisition software allowed binning a fixed number of pixels along each spatial dimension. If A pixels are binned along the horizontal axis and B pixels are binned along the vertical axis then the 1024 by 256 array would be converted to a

1024/A by 256/B array with each super pixel being $A \times 27 \mu\text{m}$ wide and $B \times 27 \mu\text{m}$ high. (For simplicity, when super pixel sizes are discussed in this thesis, the size given corresponds to the pixel centers' separation. The size of one super pixel can be calculated by subtracting one pixel separation thickness of $2 \mu\text{m}$ along each axis.)

2.2 Data Acquisition

The GF-CCP-100 prototype source was used for the measurements described in Chapter 3. The remaining studies were done using the Cube FAPES source built in-house. The FAPES source was normally operated at atmospheric pressure except for the reduced pressure studies reported in Chapter 6. Details of the vacuum system are described in that chapter.

Data acquisition was controlled by a Princeton Instruments, Inc. model ST-130 controller using a 486 PC running the Princeton Instruments, Inc.'s CSMA, WinView, or WinSpec software. Since the CSMA, WinView, and WinSpec software acquire data in the same way except for the operator interface, all versions of the data acquisition software were used interchangeably. Triggering of the ST-130 controller was done *via* a function generator (Model F52A Interstate Electronics Corporation, Anaheim, CA, U.S.A.) triggered by the graphite furnace's power supply. Once the data had been acquired, spectroscopic temperatures and emission intensity profiles were calculated from the data using software written in-house in Microsoft (Redmond, WA, U.S.A.) QuickBASIC version 4.5.

The data acquisition of the light from the FAPES source followed a similar sequence, illustrated in Fig. 2.4, for all the studies reported in this thesis. (Note that the operating parameters used in the studies reported in this thesis are given

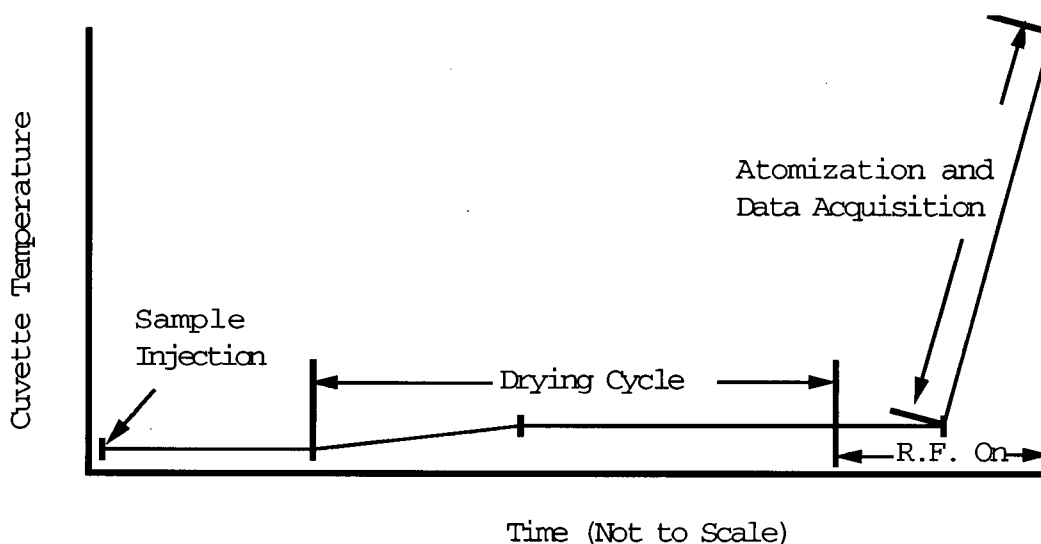


Fig. 2.4: Sequence of events during data acquisition using the FAPES sources.

in more detail in the experimental sections of the appropriate chapters.) For those studies where a sample was used, 5 to 10 μL aliquots of sample were deposited on the inside surface of the cuvette wall using an Eppendorf pipette (Brinkmann Instruments Co., Rexdale). A 2 cm long piece of 1 mm outside diameter polyethylene tube was fitted to the end of the pipette tips to allow pipetting directly into the graphite cuvette without touching, and thereby possibly breaking, the center electrode. The furnace temperature program was then initiated.

The furnace temperature was slowly ramped up to the selected drying temperature. This was followed by a quick ramp to the atomization temperature. The r.f. power to the center electrode was applied 5 s before the start of the atomization cycle, during the drying cycle, and left on throughout the remainder of the furnace temperature program for the emission studies. The furnace power supply sent a trigger pulse to the function generator at the beginning of the

atomization cycle. The function generator was used to send a series of timed pulses to the CCD controller which opened and closed the shutter at each of these pulses for a predetermined, software controlled, exposure time. After each exposure, the CCD controlling software stored the intensity signal for each pixel, or super pixel on the CCD into a file on the hard drive of the 486 PC.

Peak heights were used in all the measurements as they resulted in better precision than did peak areas. Background subtraction was done by baseline subtraction in the spectral dimension thus removing any contribution to the peak heights from background continuum radiation due to ion-electron recombination and from blackbody radiation off the graphite furnace and center electrode. These peak heights were usually normalized to account for the pixel binning (hardware summing of CCD pixels) and the data acquisition integration, or exposure, times. In all the spatial profiles presented in this thesis, both of signal intensities and spectroscopic temperatures, the horizontal axis represents the vertical position in the FAPES source with the origin being at the center of the source, namely the center electrode.

2.3 Analyte Atomization

A single atomization temperature was chosen for all the analyte emission and absorption signal measurements since the main goal of these studies was to characterize the plasma in the FAPES source and not the analyte's atomization behavior. Unless otherwise noted the atomization temperature chosen was 1450 °C because the plasma became unstable and extinguished itself at higher temperatures. This was characterized by a sharp increase in the reflected r.f. power with the impedance matching network unable to match the impedance of the source. Rahman [23] has shown that this is likely caused by a sharp

increase in the thermionic emission of electrons from the graphite cuvette and center electrode which occurs around this temperature. This increase in electrons likely reduced the impedance of the source faster than the impedance matching network can react and possibly lower than it can match thus the r.f. power delivered to the plasma dropped sharply and the plasma became extinguished.

CHAPTER 3

SPATIALLY RESOLVED TEMPERATURE MEASUREMENTS *

“In short, the goal of spectrochemical physics is the shaping or reshaping of spectrochemical analysis methods as the fruit of rational thinking and experimentation rather than as the result of trial and error fiddling.”

P.W.J.M. Boumans [77]

3.1 Introduction

Spatially resolved atomic and molecular emission was measured in the FAPES source while varying the forward r.f. power applied to the center electrode. From these measurements, some spatially resolved spectroscopic temperatures were calculated. These results were used to gain a better understanding of the plasma within the FAPES source.

Several papers [4-7, 10, 15, 18, 20] have discussed the effect of changing the forward r.f. power applied to the center electrode. Sturgeon *et al.* [5] noted that, as the r.f. power is increased, there is an increase in the emission intensity from He(I) lines. A 25 Watt increase in r.f. power from 50 Watts to 75 Watts resulted in a 3-fold increase in the emission intensity from the He(I) 587.6 and 447.1 nm lines. This was further seen as a slight increase in the He(I) excitation

* Portions of this chapter have been published in *Spectrochim. Acta*, **50B**, 1395 (1995).

temperature [7]. Raising the input r.f. power from 25 Watts to 100 Watts increased the He(I) excitation temperature from 2990 K to 3300 K. Hettipathirana and Blades [10] measured a linear relationship between the r.f. power and the excitation temperature of Fe(I) with values ranging from 3100 K to 4200 K at r.f. powers of 10 Watts to 50 Watts respectively. Both groups also observed a degradation in the signal-to-noise ratio of analyte emission signals due mainly to a loss in the stability of the plasma [4, 10]. At higher r.f. powers, temporal shifts in emission peak positions [5, 10] also occurred with appearance temperatures increasing or decreasing depending on which element was observed. In some cases, it was found that an increase in the r.f. power caused multiple peaks to form. This latter effect was attributed to analyte condensation on the center electrode. While these analyte signal observations suggest that increasing the r.f. power leads to inferior analytical conditions, the spectroscopic diagnostic measurements suggest that higher r.f. powers provide more energetic excitation conditions, clearly an advantage for optical emission spectrometry. In some cases this more energetic excitation environment also reduces interferences from easily ionizable elements. The signal from 5 ng of Pb was attenuated by 18 mg of NaCl [6] to 70% at 50 Watts r.f. power, 80% at 75 Watts and remained unchanged at 100 Watts.

The potential of an analytical source to excite analyte atoms can be studied by measuring spectroscopic temperatures within it. To date no studies published (except those shown here [24]) have shown the spatial distribution of these parameters. In the studies reported in this chapter, the effect of the magnitude of the r.f. power applied to the center electrode in a helium plasma was characterized by measuring the spatially resolved emission of four spectrometric species: He, N_2^+ , OH, and Pb. Spatially resolved helium atomic

emission was measured to provide information on the spatial distribution of the plasma inside the graphite cuvette at different r.f. powers. Spatially resolved emission from N_2^+ and OH was used to calculate the effect of r.f. power on the rotational temperatures of these species. Finally, the effect of r.f. power on the excitation temperature of an analyte, Pb(I), was calculated.

3.2 Experimental

3.2.1 Background

3.2.1.1 OH Rotational Temperature Measurements

OH rotational temperatures were calculated by measuring emission line intensities around 308 nm from the Q₁ branch of the OH (0-0) rotational $A^2\Sigma^+ \rightarrow X^2\Pi_i$ band. Fig. 3.1 is an emission spectrum from the FAPES source operating with 60 Watts r.f. power showing the OH lines used. As was discussed with more detail in Chapter 1, a Boltzmann plot of $\ln(I_{em}\lambda/A_k)$ vs. E_k yields a straight line with a slope equal to $-hc/k_B T_{rot}$ where I_{em} , λ and A_k are the emission intensity, wavelength, and transition probability of the spectral line measured. E_k is the energy level of the upper state, k_B is the Boltzmann constant, h is the Planck constant, c is the speed of light, and T_{rot} is the rotational temperature. Six lines, Q₁₂, Q₁₄, Q₁₅, Q₁₆, Q₁₉, and Q₁₀ were used in these calculations and the A_k and E_k spectroscopic data for these lines was taken from Mermet [68].

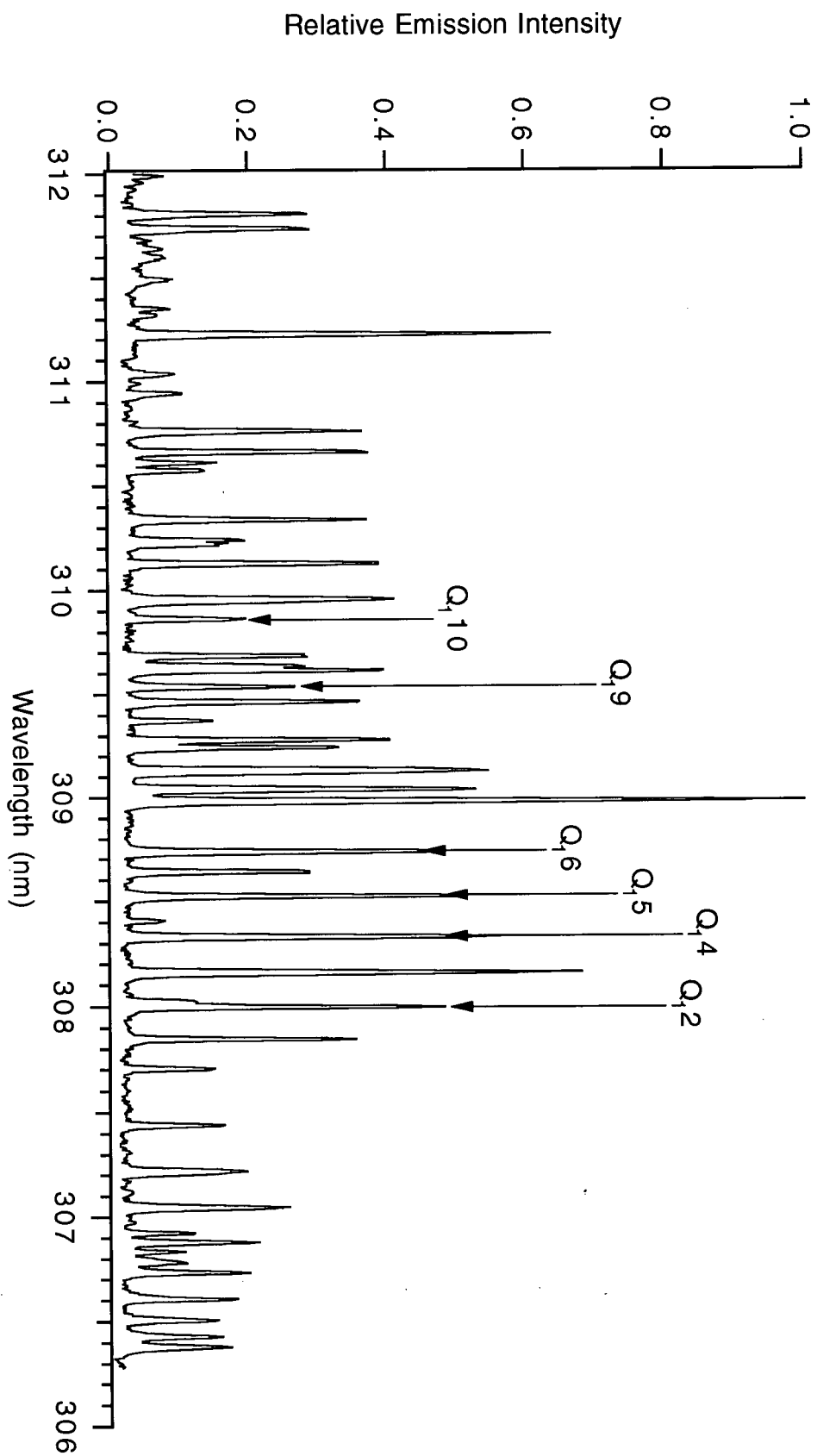


Fig. 3.1: OH spectrum in the FAPES source at 60 Watts r.f. power.

3.2.1.2 N₂⁺ Rotational Temperature Measurements

N₂⁺ rotational temperatures were calculated by measuring emission line intensities around 390 nm from the R branch of the of the first negative system of N₂⁺ (0-0) rotational B²Σ_u⁺ → X²Σ_g⁺ band. Fig. 3.2 is an emission spectrum from the FAPES source operating with 60 Watts r.f. power showing the N₂⁺ lines used. For the R branch emission intensities measured, a Boltzmann plot of $\ln(I_{em}/a2(K''+1))$ vs. $(K''+1)(K''+2)$ yields a straight line with a slope equal to $-B'hc/kT_{rot}$ where B' is the rotational constant of the upper electronic state [71], a is the alternating intensity factor (equal to 1 for even K'' and 2 for odd K'') [78] and K'' is the angular momentum quantum number for the upper state. Seven lines with K'' equal to 6, 8, 10, 12, 14, 16, and 18 were used for these calculations.

3.2.1.3 Pb(I) Excitation Temperature Measurements

Pb(I) excitation temperatures, T_{exc}, were calculated using the line pair intensity ratio method [68] described in Chapter 1. Pb(I) was chosen as a spectrometric species in this study for several reasons. The plasma in the FAPES source used in this study became unstable at temperatures above 1600 K, eventually extinguishing at higher temperatures. The cause of this instability has not yet been investigated however, it is believed to be caused by the emission of thermionic electrons from the center electrode and cuvette wall at higher temperatures, thus changing the impedance of the source beyond the range or faster than the response time of the impedance matching network [23]. Lead has been shown to have appearance temperatures in the FAPES source of 770 K and 1010 K at r.f. powers of 40 Watts and 14 Watts respectively [15], well

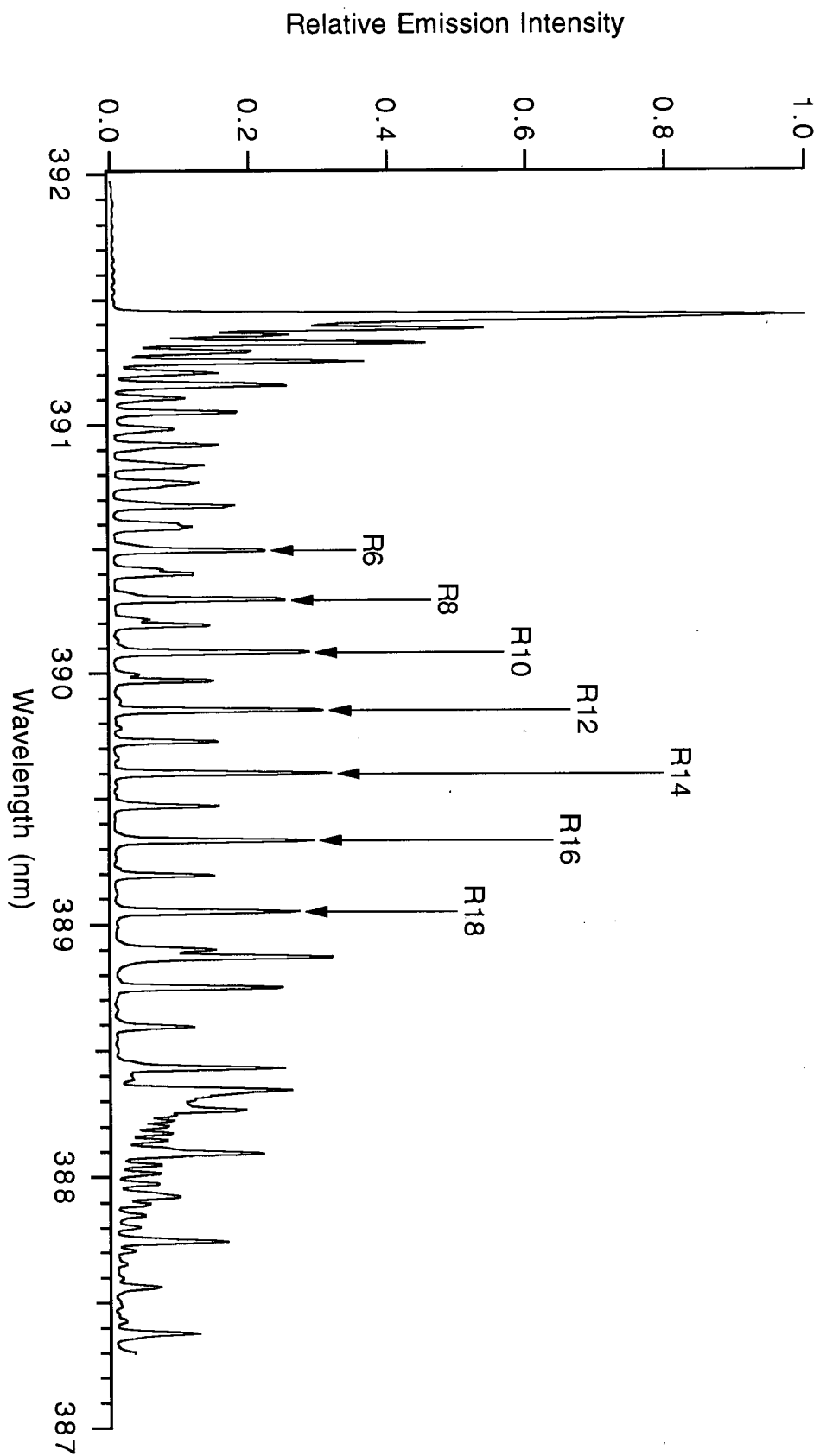


Fig. 3.2: N_2^+ spectrum in the FAPES source at 60 Watts r.f. power.

Wavelength (nm)	$g_k A_k$ (10^8 s^{-1})	E_k (cm^{-1})
280.199	43	46329
283.306	1.8	35287

Table 3.1: Spectroscopic data for Pb(I) lines used to calculate excitation temperatures [79, 80].

within the operating range of the source. Lead also has two fairly sensitive emission lines, listed in Table 3.1, which have a small difference in wavelength and a relatively large separation in upper energy levels, E_k .

The small wavelength separation of these two lines makes it possible to measure their intensity simultaneously with the CCD detector used since their separation is less than the spectral window of the detector. A large energy separation in the upper energy levels of the two lines use in the line pair intensity ratio method is preferred since this difference determines the sensitivity of the technique.

3.2.2 Instrumental Parameters

This study involved spatial characterization therefore some degree of spatial resolution was necessary. A 50 mm focal length fused silica biconvex lens was used for 1:1 imaging of the FAPES source onto the entrance slit of the monochromator. After trying several f /numbers by using different diameter apertures in front of the lens, $f/100$ was settled on as yielding the best balance

between light throughput and spatial resolution. Since the furnace was 18 mm long and the lens was positioned to focus the center of the furnace onto the monochromator's entrance slit, a spatial resolution of 90 μm resulted at the furnace's opening. The width of the entrance slit of the monochromator was set to 100 μm . In order to obtain the necessary data acquisition speed, 8 pixels along the spatial (vertical) dimension of the CCD were binned (hardware summed) with no binning along the spectral dimension. While this yielded a measurement spatial resolution of 0.2 mm, the f/100 optics were retained to standardize the measurements.

The 3600 lines/mm holographic grating was installed in the monochromator for measuring the OH and N_2^+ spectra and the 1200 line/mm holographic grating was installed for measuring the Pb(I) spectra. As noted in Chapter 2, these choices were dictated by the spectral resolution necessary to resolve the emission lines and the spectral width observed by the detector.

3.2.3 Procedure

The He 388.86 nm atomic emission line as well as the N_2^+ and OH molecular emission lines have been shown [10] to be present in the background spectra of the helium FAPES source, however, it was necessary to introduce lead into the source to obtain Pb(I) spectra. In order to obtain Pb(I) spectra, 10 ng of lead were injected into the graphite cuvette as 5 μL aliquots of an aqueous 2 ppm lead solution. This 2 ppm lead solution was prepared by dissolving the appropriate amount of $\text{Pb}(\text{NO}_3)_2$ in deionized water followed by serial dilutions. The graphite furnace temperature profile was optimized for these Pb(I) spectral measurements and consisted of 10 s at 100 $^\circ\text{C}$ then 50 s at

500 °C followed by an atomization step at the furnace's maximum heating rate to 1100 °C. The 50 s step at 500 °C was found necessary to remove all the water from the furnace work-head. The CCD integration times were optimized to observe the entire temporal profile of the Pb(I) emission. This resulted in using a 1.5 s integration time starting at the beginning of the atomization cycle.

Replicate measurements of the optical emission data from the background species, He, OH, and N_2^+ , at 60 Watts r.f. power resulted in relative standard deviations less than 1 % of the maximum intensities for each profile. Therefore, error bars are not included in the emission profiles.

3.3. Results and Discussion

3.3.1 The Effect of R.F. Power on the Spatial Profiles of He, OH, and N_2^+ Emission Lines

The effect of r.f. power level on the emission profile of the helium 388.86 nm line in the FAPES source is shown in Fig. 3.4. At low powers the plasma is located primarily next to the center electrode. As the r.f. power is increased from 20 Watts to 200 Watts this emission increases almost 20 fold. At higher r.f. powers there is a relative increase in the emission adjacent to the cuvette wall. There is also some fairly low intensity emission throughout the volume of the cuvette which also increases slightly at higher r.f. powers relative to the maximum emission.

These observations agree well with Schwab and Hotz's theoretical calculations [58] and experimental observations [59, 62] in atmospheric pressure r.f. discharges operating in air with electrodes in contact with the discharge.

They found that the plasma operates similarly to direct current glow discharge with the cathode glow shifting from one electrode to the other in alternating half-cycles. Since the current density is related to the area of the electrode, the plasma is less energetic adjacent to the cuvette wall compared to adjacent to the center electrode. This agrees with the observation that the He(I) emission intensity is more intense adjacent to the center electrode than adjacent to the cuvette wall. Schwab *et al.* [58] also noted that since the voltage necessary to maintain the discharge was less than that required to ignite it, there must be some residual ionization remaining between the electrodes throughout the r.f. cycle. This likely corresponds with the low intensity He(I) emission observed in the volume of the cuvette described above.

Fig. 3.3 contains a plot of the spatially integrated emission intensities from the helium 388.86 nm line for different r.f. powers applied to the center electrode. There is a fairly linear relationship between the total emission intensity from this line and the r.f. power. This correlates well with previous studies. Sturgeon *et al.* [5] observed an increase in the emission intensities from cadmium, copper, and iron analytes when increasing the applied r.f. power from 50 to 75 Watts. The data in the present study does not support one of their conclusions that the increased emission is related to an increase in the plasma volume unless the weak emission adjacent to the cuvette wall is considered the increase in plasma volume. While they lacked the spatial information necessary to measure this effect, the present study does give some indications that this is not the case. In Fig. 3.4, the vertical emission profiles of the helium 388.86 nm line at r.f. powers from 10 Watts to 200 Watts, show no increase in the plasma volume, reflected in the spatial width of the profiles, adjacent to the center electrode but the intensity does increase significantly. However, this may also be due to the limitations in

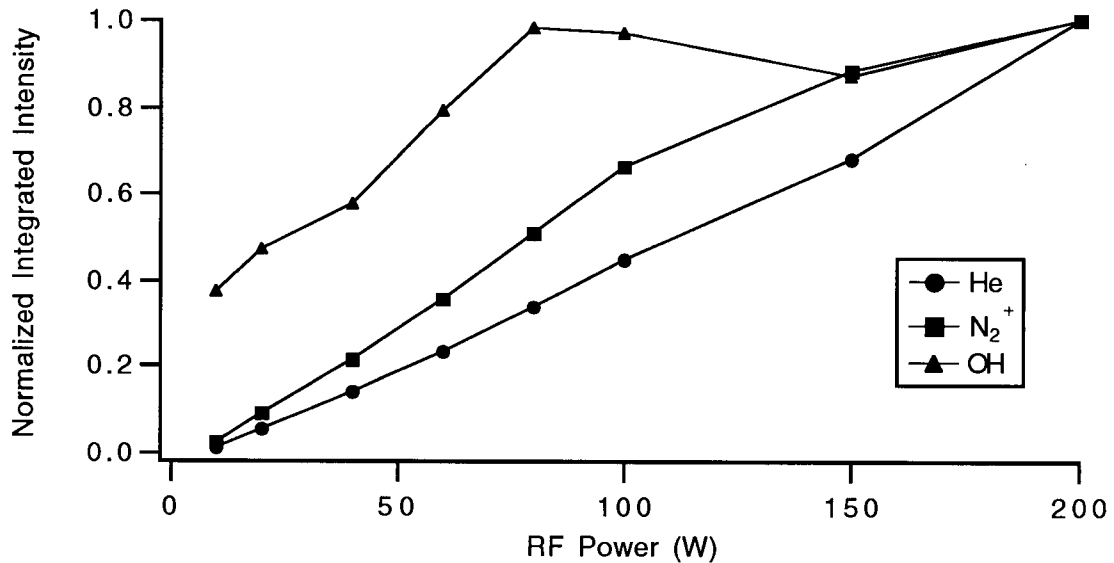


Fig. 3.3: Effect of r.f. power on the spatially integrated emission intensities from He(I), N₂⁺, and OH.

the spatial resolution used in this experimental setup (0.2 mm) which may not be adequate to resolve this effect. The increase in emission intensity does suggest an increase in the plasma energy at higher r.f. powers. It also suggests an increase in the excitation temperature of helium, noted by Sturgeon *et al.* [7], since an increase in the measured emission intensity means an increase in excitation temperature if there is no change in the plasma volume.

The sum of the emission intensities, as a function of position and r.f. power applied to the center electrode, from seven N₂⁺ lines and six OH lines identified earlier, are shown in Figs. 3.5 and 3.6 respectively. In these plots it can be seen that the maximum emission from these molecules occurs, as expected, where the plasma has the greatest excitation ability, or highest excitation temperature, as defined by maxima in the emission from helium.

However, there are two significant differences. The maximum emission from each molecule does not increase as much as did the helium emission upon increasing the r.f. power and the relative emission in the intermediate region between the center electrode and the cuvette wall, when compared to that from adjacent to the center electrode, is much greater at higher r.f. powers. The maximum emission intensity from N_2^+ increases only about 7 fold from 20 Watts to 200 Watts while that from OH increases less than 2 fold. In fact, there is no significant increase in the OH emission next to the center electrode above 60 Watts. Both of these observations reflect the same effect and can be explained readily by considering the stability of the two molecules.

Emission intensity from species in spectroscopic plasmas is a function of excitation temperature and a linear function of the population density of the emitting species; a property which is used in the application of optical emission sources as analytical tools. Since the population of helium atoms is fairly constant throughout the volume of the cuvette, the emission profile of helium is representative of the excitation temperature in the FAPES source (see equations 1.1 and 1.2). For N_2^+ and OH this is not the case. If we compare the emission profiles from N_2^+ and OH with those from helium we see that there is an attenuation in the molecular emission relative to the atomic emission at higher r.f. powers. Furthermore this attenuation appears to be correlated with the helium emission; the greatest attenuation occurs at positions where helium emission is most intense. The cause of this relative attenuation can be attributed to a dissociation of the N_2^+ and OH molecules which is greatest where the plasma has the most energy. This conclusion is additionally supported by the plot of the spatially integrated emission profiles from He, N_2^+ , and OH as a function of r.f. power, shown in Fig. 3.3. This plot shows a fairly linear relationship between the

r.f. power and the helium emission intensity. Both N_2^+ and OH possess this linear relationship at low r.f. powers however at higher r.f. powers both curves bend towards the r.f. power axis. This attenuation is much more pronounced and occurs at lower r.f. powers for OH than for N_2^+ suggesting that OH is dissociated more easily than N_2^+ by the plasma. In fact, the OH emission intensity does not increase significantly above 80 Watts r.f. power. These observations correlate well with the dissociation energies of these two molecules. The OH molecule with a dissociation energy of 4.39 eV is easier to atomize than N_2^+ whose dissociation energy is 8.713 eV [81]. Pavski *et al.*'s spatially resolved emission data from CO^+ , N_2 , NO, and OH at 50 Watts r.f. power in a FAPES source shows a similar trend [22].

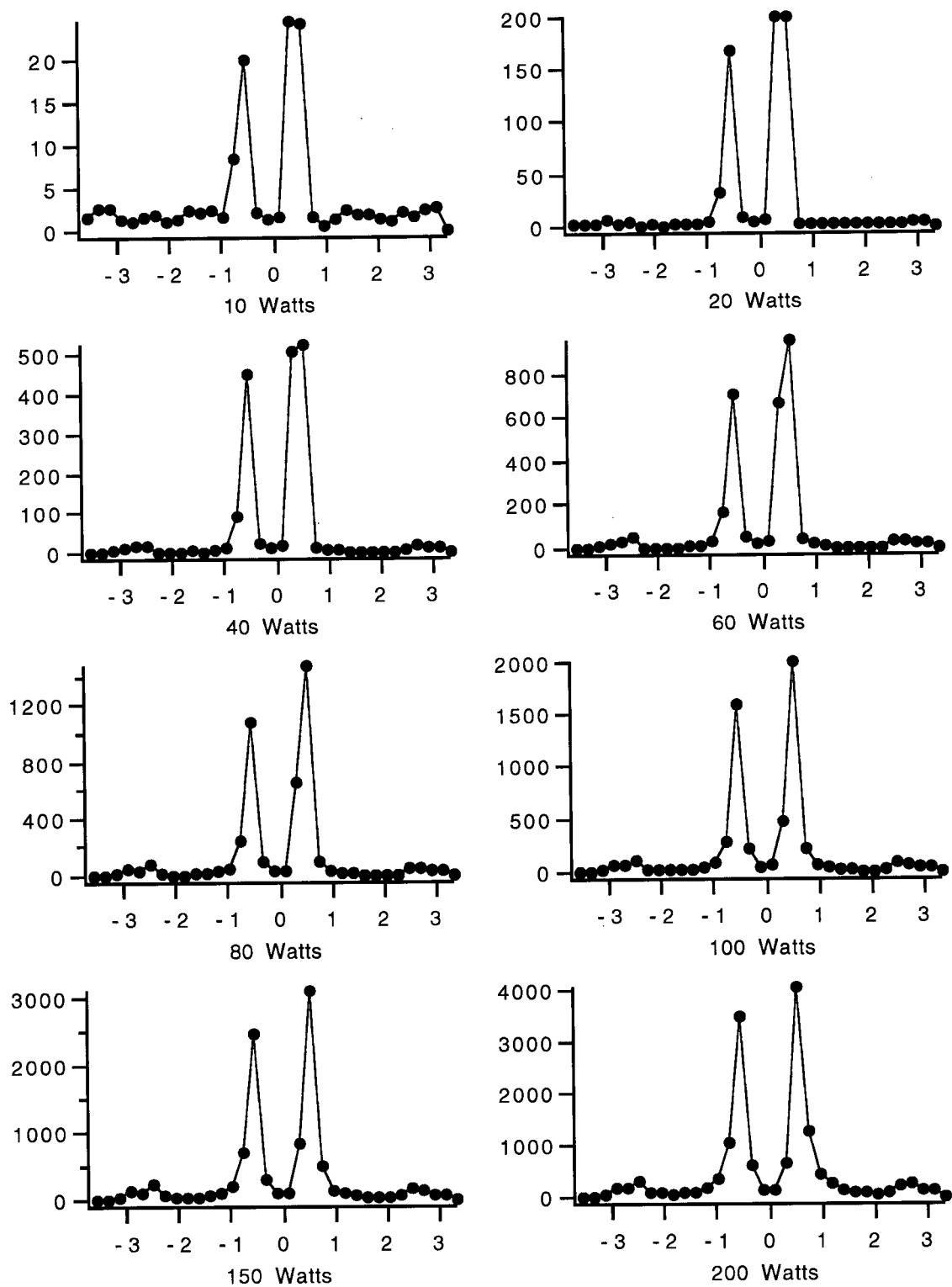


Fig. 3.4: He(I) 388.86 nm emission intensity spatial profiles measured at different r.f. powers. Plots are of emission intensity (in Counts Pixel⁻¹ s⁻¹) versus vertical position (in mm).

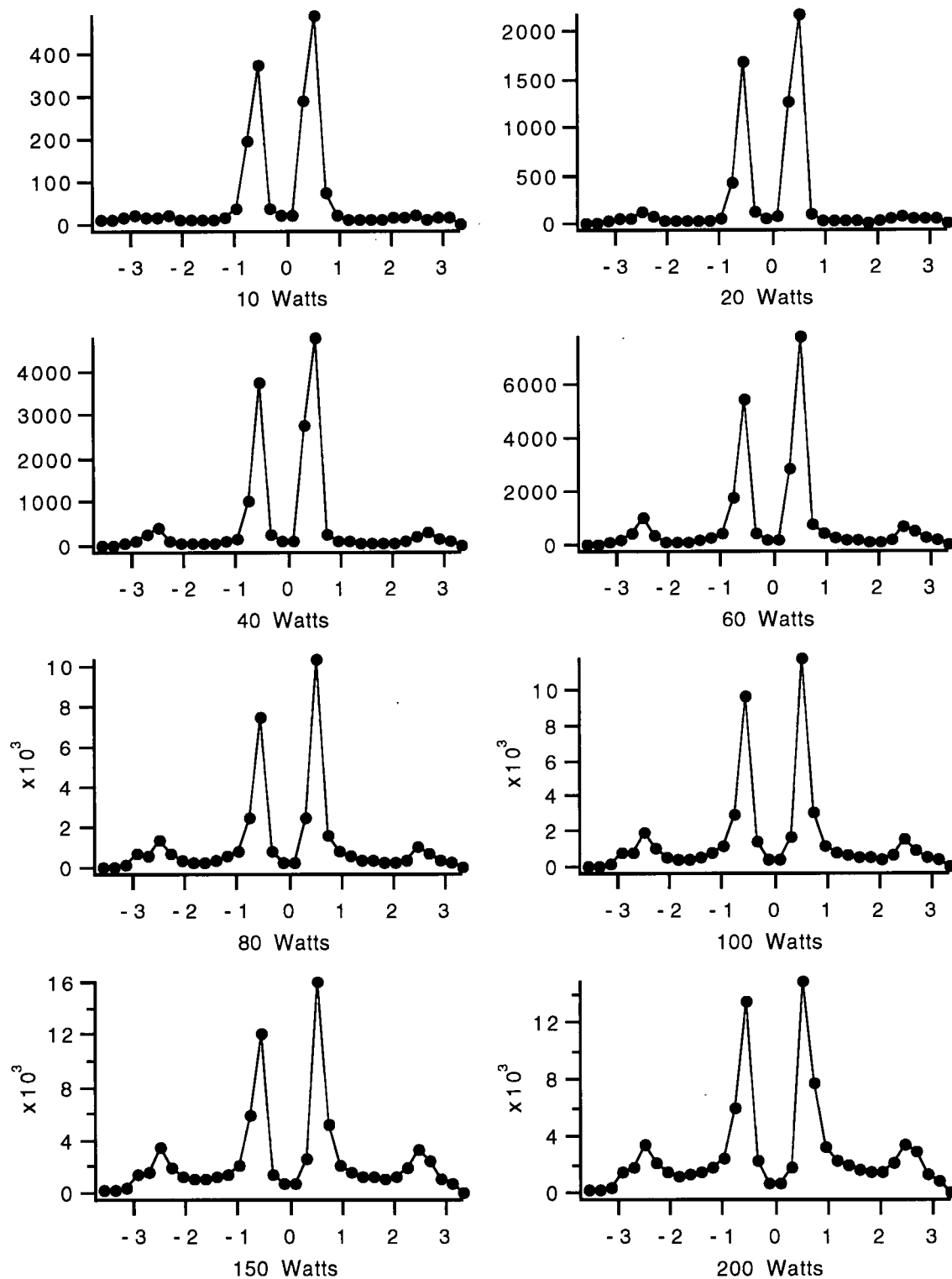


Fig. 3.5: Vertical emission profiles of the sum of the N_2^+ lines measured at different r.f. powers. Plots are of emission intensity (in Counts Pixel $^{-1}$ s $^{-1}$) versus vertical position (in mm).

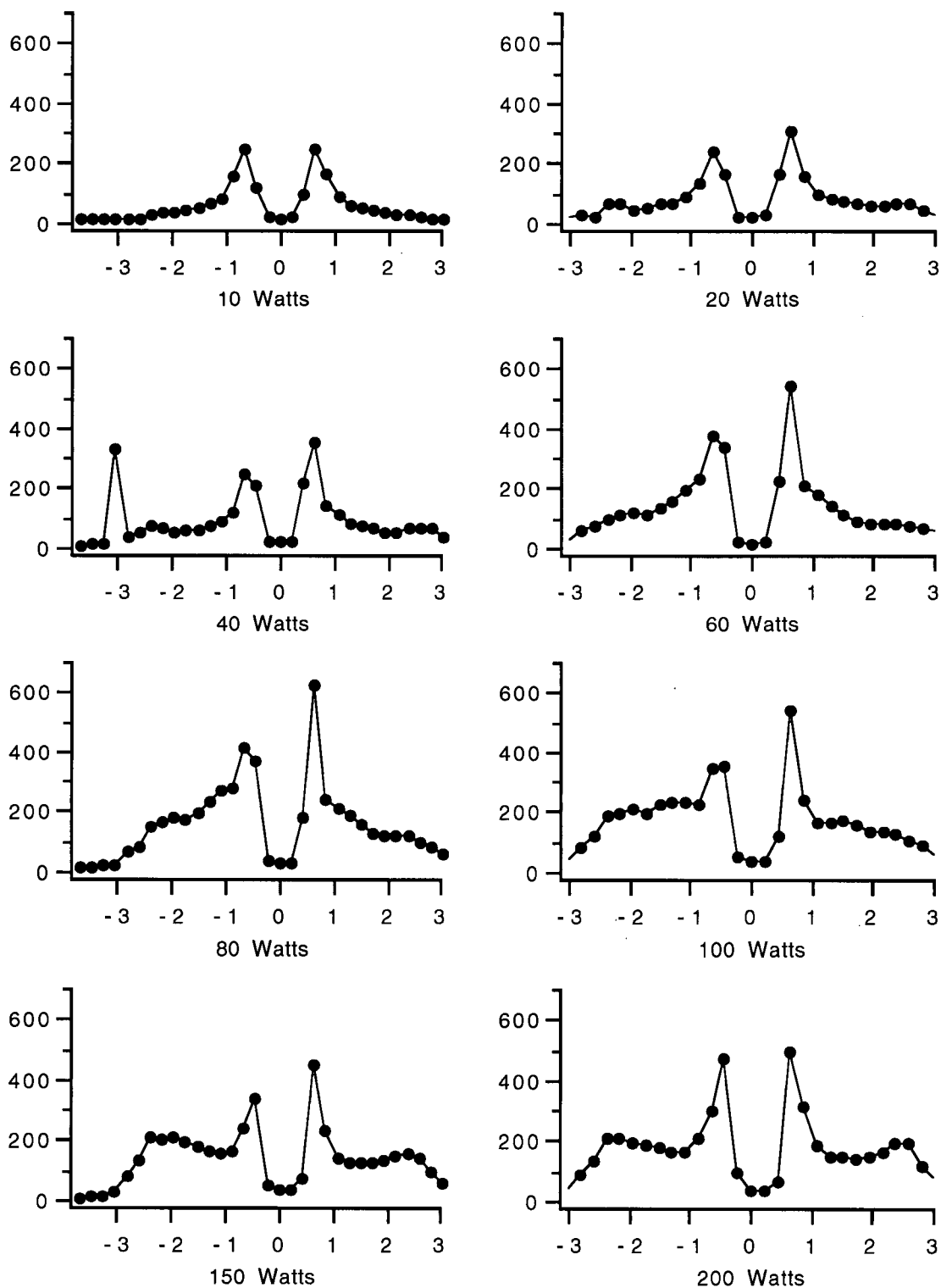


Fig. 3.6: Vertical emission profiles of the sum of the OH lines measured at different r.f. powers. Plots are of emission intensity (in $\text{Counts Pixel}^{-1} \text{ s}^{-1}$) versus vertical position (in mm).

3.3.2 Rotational Temperature Profiles of OH and N₂⁺

Rotational temperatures of OH and N₂⁺ were calculated from the molecular emission measurements discussed above. Figs. 3.7 and 3.8 are plots of the spatially resolved rotational temperatures of these two molecules in the FAPES source at 60 Watts r.f. power. The precision shown in the temperature values are based on the reproducibility of five repeat measurements.

The rotational temperature of OH in the FAPES, at this power, ranges between 680 K and 1050 K, excluding the temperature values where the emission measurements coincide with viewing the center electrode. The maximum rotational temperature occurs near the center electrode with a gradual decrease towards the minimum at 2.4 mm from the center of the source. The temperature then increases slightly next to the graphite cuvette wall. The N₂⁺ rotational temperature at 60 Watts forward r.f. power ranges between 580 K and 1920 K. The spatial structure of this temperature is similar to that of the OH rotational temperature profile with maxima and minima at the same positions, within the experimental spatial resolution. The most significant difference between the two profiles is the sharp increase in the rotational temperature of N₂⁺ next to the center electrode. The magnitude of the rotational temperature range for N₂⁺ is also approximately 3.6 times higher than that for OH with most of this difference accounted for by the relatively high N₂⁺ rotational temperatures next to the center electrode.

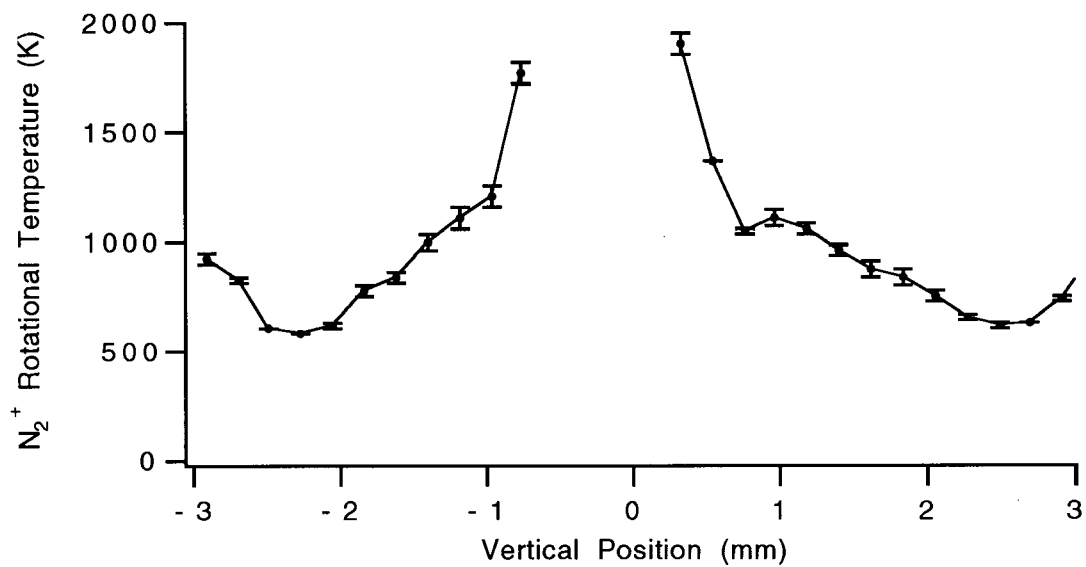


Fig. 3.7: N_2^+ rotational temperature vertical profile at 60 Watts r.f. power. Error bars represent ± 1 standard deviation (5 samples).

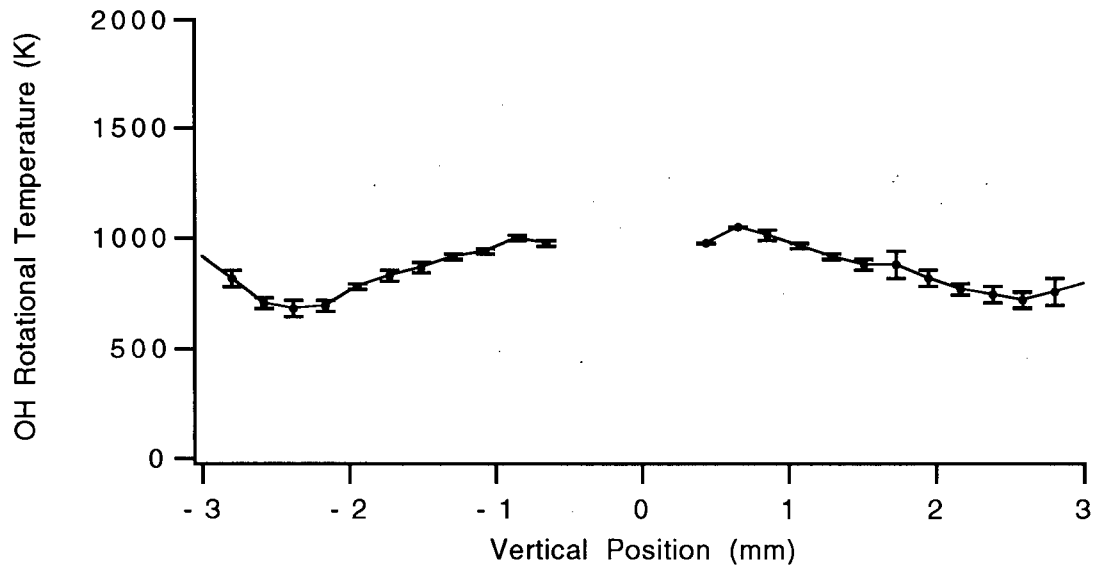
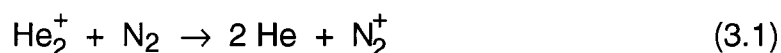


Fig. 3.8: OH rotational temperature vertical profile at 60 Watts r.f. power. Error bars represent ± 1 standard deviation (5 samples).

Figs. 3.9 and 3.10 are plots of the effect of increasing the r.f. power on the spatially resolved rotational temperatures for OH and N_2^+ respectively. The precision of these measurements can be assumed to be the same as those reported in Figs. 3.7 and 3.8 since the same experimental conditions were used. These plots show that the molecular rotational temperatures of OH and N_2^+ increase throughout the volume of the FAPES source as the r.f. power applied to the center electrode is increased. From 1 mm outwards, the rotational temperatures of both molecules appears to be fairly similar. The most dramatic difference occurs for the N_2^+ adjacent to the center electrode. The OH molecule does not show such a dramatic increase at that position. From 1 mm outwards the rotational temperatures of OH and N_2^+ reflect the gas kinetic temperature within the cuvette [68]. Adjacent to the center electrode this is still the case for OH but not for N_2^+ . As can be seen in Fig. 3.10, the N_2^+ rotational temperature shows a steep increase adjacent to the center electrode. This increase is most likely due to the mechanism by which N_2^+ is formed. It has been shown [82] that in He discharges, N_2^+ is formed *via* a charge transfer reaction with He_2^+ .



This reaction is possible because the wide recombination energy of He_2^+ is resonant with the $B^2\Sigma_u^+$ energy level of N_2^+ as shown in Fig. 3.11. The result is an N_2^+ population whose rotational energy distribution is affected not only by the gas kinetic temperature but also by the energies resulting from the charge transfer reaction. This results in a higher rotational temperature for N_2^+ .

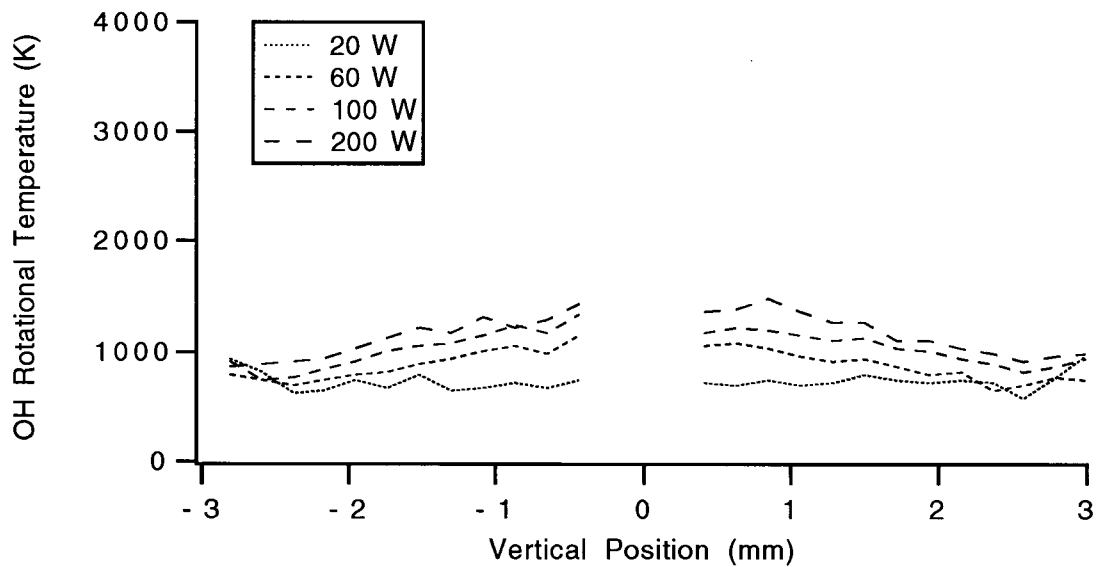


Fig. 3.9: Effect of r.f. power on the spatial profile of the OH rotational temperature.

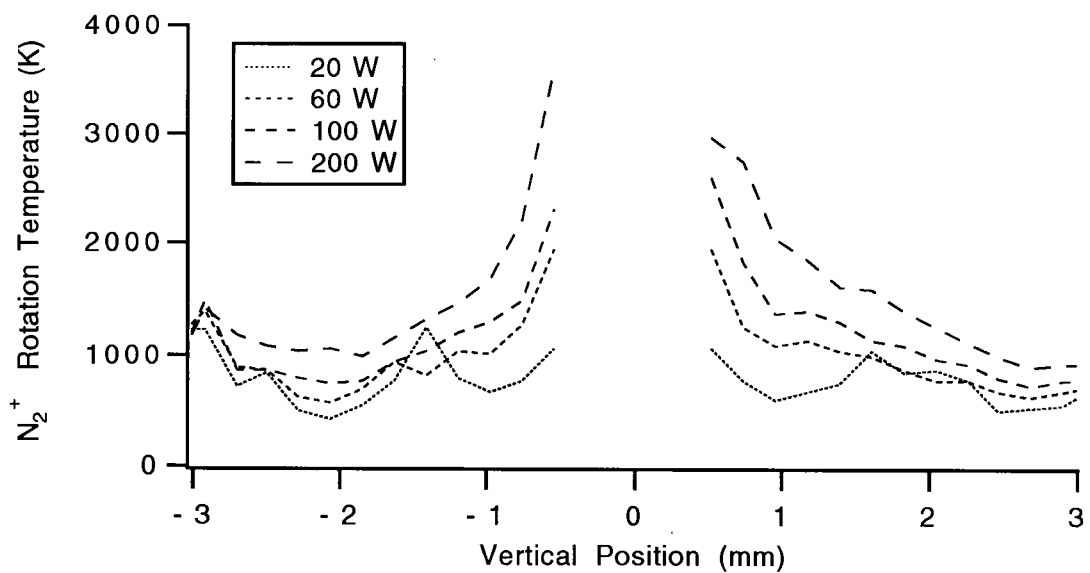


Fig. 3.10: Effect of r.f. power on the spatial profile of the N₂⁺ rotational temperature.

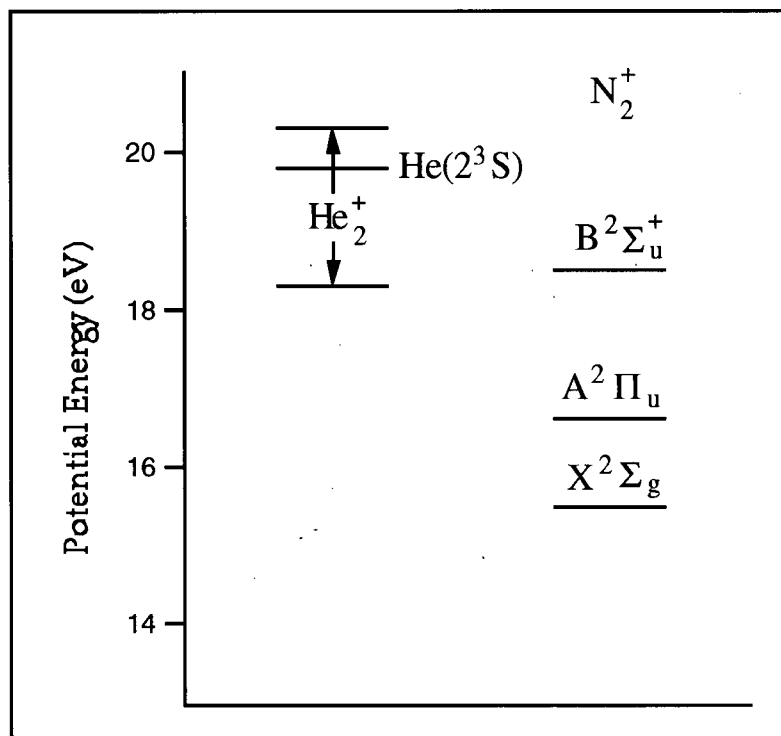


Fig. 3.11: Partial energy level diagram for He₂⁺, He(2³S) and N₂⁺.

Spencer *et al.* [83] have summarized some OH and N₂⁺ rotational temperatures reported for other atmospheric pressure helium plasmas. The rotational temperatures for the helium FAPES source reported above are well below those in the inductively coupled plasma, slightly less than those in the capacitively coupled microwave plasma and similar to those found in the microwave induced plasma.

3.3.3 Pb(I) Excitation Temperatures

The spatially resolved emission profile of the Pb(I) 280.20 nm line for an r.f. power of 25 Watts is shown in Fig. 3.12. As with the background species, there is a minimum that coincides with viewing the central electrode as expected. Compared with the spatial distribution of the emission from the plasma gas species, He(I), OH, and N_2^+ , the spatial distribution of Pb(I) emission is much more uniform though some spatial structure is present. There are maxima adjacent to the center electrode and cuvette wall and one at a radius of 1.25 mm. The two maxima adjacent to the center electrode and cuvette wall coincide with the He(I) emission maxima and reflect analyte excitation temperatures described below. The maximum at a radius of 1.25 mm cannot be explained simply in terms of excitation temperatures. Emission and absorption studies were performed in order to explain this maximum and the entire analyte emission spatial structure. These are described in later chapters of this thesis.

The spatially resolved excitation temperature of Pb(I) in the FAPES source at 25 Watts r.f. power is shown in Fig. 3.13. The error bars shown represent ± 1 standard deviation of five measurements. Ignoring the regions where the emission, seen in Fig. 3.12, is relatively low, we see that the excitation temperature of Pb(I) is fairly constant in the volume of the plasma and rises slightly adjacent to both the graphite cuvette wall and center electrode. This is also consistent with the discussion above regarding the spatial distribution of the helium emission, namely that this source operates similarly to a radio frequency glow discharge with the cathode glow shifting from one electrode to the other in alternating half-cycles. Pb(I) excitation temperature profiles have also been measured for r.f. powers of 35, 50, 65, and 75 Watts. These profiles have similar

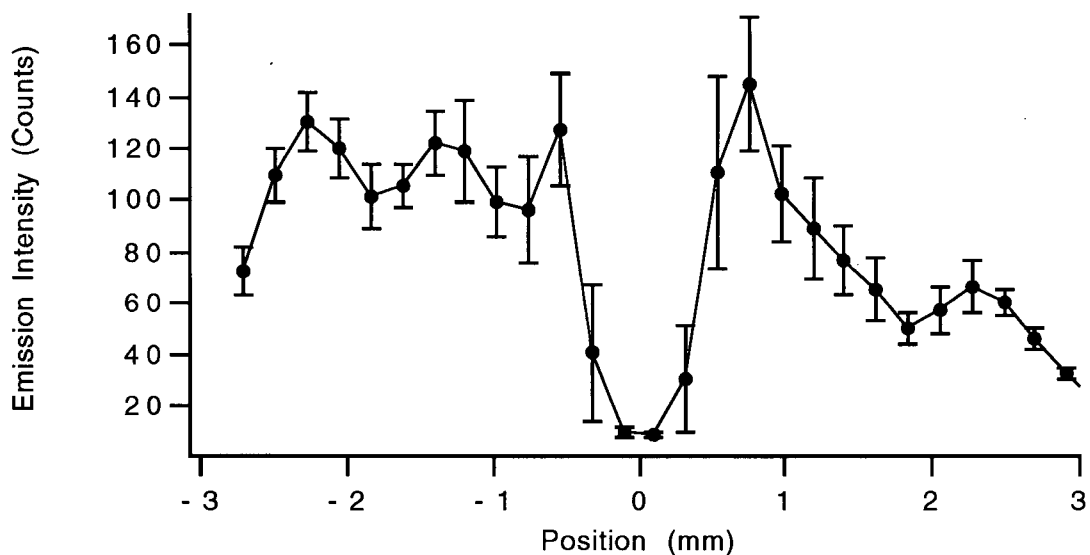


Fig. 3.12: Spatial emission profile of the Pb(I) 280.20 nm line for a 10 ng lead sample with 25 Watts r.f. power.

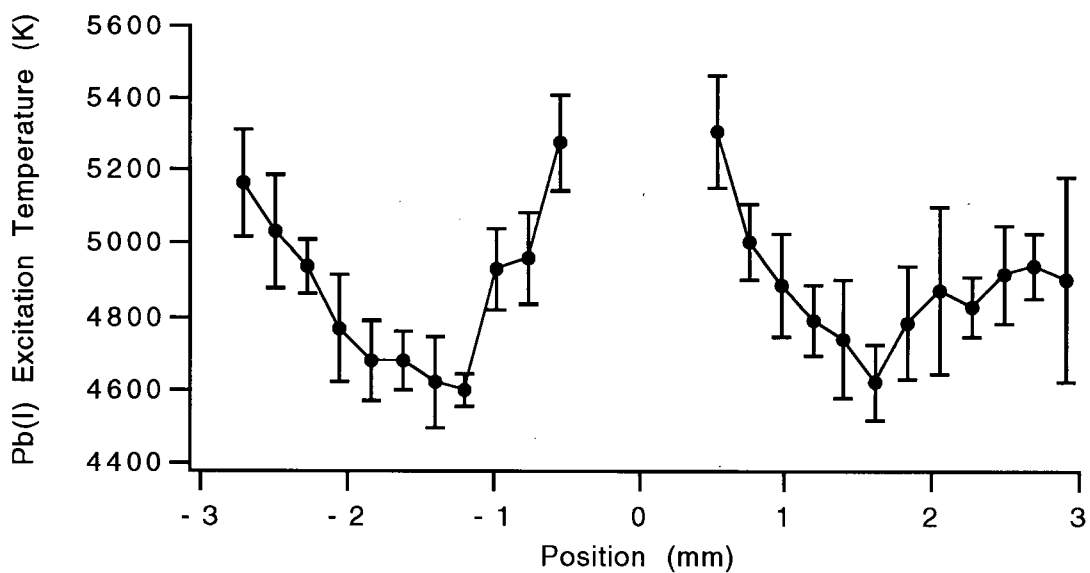


Fig. 3.13: Spatial profile of Pb(I) excitation temperature at 25 Watts r.f. power.

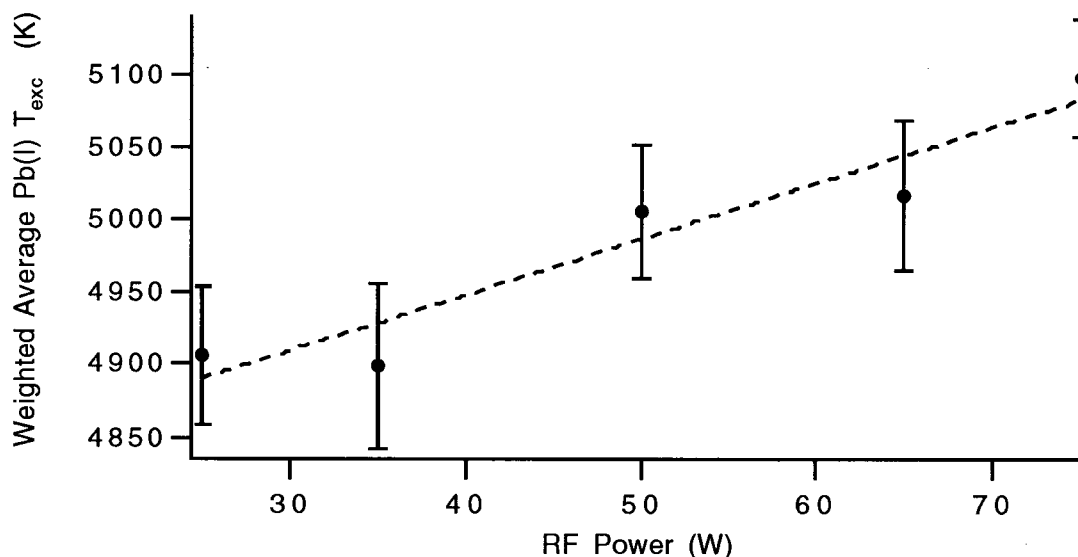


Fig. 3.14: Effect of r.f. power on Pb(I) excitation temperature.

appearances to the profiles for the 25 Watts plasma with minima in the Pb(I) excitation temperature around 1.5 mm and maxima adjacent to the cuvette wall and center electrode however, at higher r.f. powers there is a trend towards higher excitation temperatures.

This trend can be seen most clearly if the emission data is spatially integrated before calculating excitation temperatures thus giving a single value for each r.f. power level. This integration yields results equivalent to those that would be obtained by spatially integrated emission measurements. Fig. 3.14 shows the result of this calculation. Again the error bars represent ± 1 standard deviation of five repeat measurements. A least squares linear regression fit to the data results in a slope of 3.8 ± 0.7 K/Watt and an intercept of 4790 ± 40 K. This degree of dependence of excitation temperature on r.f. power agrees well with previously published data by Sturgeon *et al.* [9]. A calculation on their He(I) excitation temperature data shows a slope of 4.1 K/Watt r.f. power.

3.4 Summary and Conclusions

Spatially resolved atomic emission intensities from helium, and molecular emission intensities from OH and N_2^+ were measured in a FAPES source. He(I) emission at 388.86 nm was used to monitor the spatial structure of the plasma in the source while increasing the r.f. power applied to its center electrode. At higher r.f. powers the He(I) emission intensity increased significantly while its spatial structure remained relatively unchanged. The He(I) emission was found to be most intense adjacent to the center electrode. Some less intense emission was observed adjacent to the graphite cuvette wall and some very weak emission was seen throughout the volume of the source. These observations suggest that the FAPES source operates as an r.f. glow discharge.

Emission intensities from the OH (0-0) rotational $A^2\Sigma^+ \rightarrow X^2\Pi_i$ and N_2^+ (0-0) rotational $B^2\Sigma_u^+ \rightarrow X^2\Sigma_g^+$ bands were used to monitor the effects of increasing the r.f. power applied to the center electrode of the source. From these measurements, rotational temperatures for these molecules were calculated. The intensity measurements showed that there is a significant thermal gradient in the source with OH rotational temperatures ranging between 680 K and 1050 K and N_2^+ rotational temperatures ranging between 580 and 1920 K with 60 Watts r.f. power applied to the center electrode. At higher r.f. powers there is an increase in rotational temperatures and an increase in the dissociation of molecular species in the FAPES source.

Lead excitation temperatures were calculated using the line ratio method by measuring the emission of the Pb(I) 280.20 nm and 283.31 nm lines at different r.f. powers. The temperature was found to increase monotonically with r.f. power over the range of 25 to 75 Watts.

CHAPTER 4

ANALYTE SPATIAL AND TEMPORAL PROFILES

“Good emitters are good absorbers.”

Gary Horlick

4.1 Introduction

The data presented in the previous chapter shows that the spatial emission profile of atoms, ions and molecules in the FAPES source is far from uniform. Equation 1.1 shows that this emission intensity is proportional to the population of the emitting species, in this case excited state atoms, ions and molecules. The populations of these excited states are related to the total number density of the species under study and to the excitation temperature according to equation 1.1. Thus the inhomogeneity seen in the emission profiles of these species may be caused by an inhomogeneity in the total number density of the species or in the excitation conditions of the FAPES source. In this chapter, the spatial profile of an analyte, indium, was probed in the source using both emission and absorption in order to gain a better understanding on which of the two effects noted above is the main cause of the spatial emission structure observed in the previous chapter.

While no study reported thus far has looked into the spatial distribution of ground state analyte atoms in the FAPES source, such studies have been done in graphite furnaces using a variety of techniques. Holcombe *et al.* [84, 85] used a rotating spatial isolation wheel with a series of radial slits in front of the entrance slit of a monochromator to gain spatially and temporally resolved absorption profiles in a graphite furnace atomizer. Huie and Curran [86] used a dye laser together with a vidicon camera to collect similar spatially and temporally resolved absorption profiles. Stafford and Holcombe [87] used a Schlieren optical design to obtain ground state analyte distributions in a graphite furnace. Gilmutdinov *et al.* [88-90] used shadow spectral filming where a CCD camera was used as the detector attached to a Czerny-Turner monochromator operated in the slitless mode to obtain monochromatic absorption images. These studies agree quite well with one another in that analyte atoms were found to first appear adjacent to the cuvette wall where the sample had been placed. Later, the analyte atom concentration was found to have a maximum adjacent to the cuvette wall and a minimum at the center of the cuvette atomization chamber. The information from these studies that is most relevant to understanding the spatial structure of the emission in the FAPES source is that these profiles exhibit only one maximum and one minimum as opposed to the more complex spatial structure observed in the FAPES source. Such a situation in the FAPES source would indicate that the spatial structure observed in the emission profiles is due to the excitation conditions. The studies described in this chapter were aimed at gathering such information.

4.2 Experimental

Indium was chosen as the spectrometric species in the studies reported in this chapter for two reasons. First, indium's typical appearance temperature of 917 °C [91] in GFAAS was well within the operating range of the FAPES source used. Second, indium has a fairly sensitive resonance line at 303.94 nm which could be used for both atomic emission and absorption studies.

4.2.1 Background

For the experimental condition used in GFAAS, atomic absorption follows Beer's law which can be written:

$$A = -\log T = -\log \frac{I}{I_0} = abc \quad (4.1)$$

where A is the absorbance, T is the transmittance, a is the absorptivity, b is the pathlength of absorption and c is the concentration of the absorbing species. In GFAAS, absorbance values are calculated from the intensity of the incident radiation, I_0 , and that of the transmitted radiation I usually measured simultaneously. Hollow cathode lamps are usually used to provide the incident radiation in atomic absorption studies. These provide fairly intense emission lines from resonance transitions and atomic absorption is normally used to measure ground state atom population densities.

4.2.2 Instrumental Parameters

The Cube source described in section 2.1.1.2 and an indium hollow cathode lamp (Aurora Instruments, Ltd. Vancouver, B.C., Canada) light source were used to conduct the absorption studies described in this chapter. The lamp was powered by a direct current power supply built in-house which provided 5 milliamperes of current to the lamp. A 75 mm focal length biconvex fused silica lens, FL2 in Fig. 2.1, was used to focus the light from the indium hollow cathode lamp onto the center of the graphite cuvette through the back quartz window of the source. The biconvex lens was positioned such that the emission zone of the hollow cathode lamp was magnified by a factor of 4. At this magnification, the emission from the hollow cathode lamp was found to illuminate the entire cross section of the graphite cuvette.

This image was focused onto the entrance slit of the monochromator using a collimating lens and a focusing lens, CL and FL1 in Fig. 2.1 respectively. The spatial resolution of the imaging system was determined by an aperture placed on the collimating lens, CL in Fig. 2.1, and by the hardware binning of the CCD pixels. The pixels were not binned along the spectral, or horizontal, domain but 4 pixels were binned along the spatial, or vertical domain resulting in an effective pixel 0.108 mm high and 0.027 mm wide. This super pixel size, together with the magnification factor of the focusing lens system and the 1:1 internal imaging optics of the Czerny-Turner monochromator, resulted in a vertical spatial resolution of 0.18 mm at the graphite cuvette. A 3 mm diameter aperture, resulting in f/50 optics, was placed on the collimating lens. Since the graphite cuvette used in this study was 18 mm long and the collimating lens was positioned such that the center of

the cuvette was at its focal point, f/50 optics resulted in a spatial resolution of 0.18 mm at the end of the graphite furnace which matched the vertical spatial resolution at the CCD detector. The entrance slit width of the monochromator was set to 100 μm and the 3600 lines/mm grating was used. These provided sufficient spectral resolution for the indium line intensity measurements.

The 303.94 nm resonance line of indium was used for the emission and absorption measurements. Attempts to measure absorption profiles in the FAPES source with r.f. power applied to the center electrode were not successful. Since the FAPES is an emission source, the intensity of the measured indium line was given by

$$I_{\text{total}} = I_{\text{emission}} + I_{\text{lamp}} - I_{\text{absorption}} \quad (4.2)$$

where $(I_{\text{lamp}} - I_{\text{absorption}})$ is the net transmitted intensity, I , used in equation 4.1 to calculate absorbance values. Even at r.f. powers as low as 10 Watts, the emission intensity, I_{emission} , combined with the flicker noise, made absorption profiles measured with the r.f. power on unreliable. Attempts at using other indium lines to fix this problem were also unsuccessful for similar reasons; good absorbers are good emitters. Absorption profiles were therefore obtained with no r.f. power applied to the center electrode.

4.2.3 Procedure

The indium solutions used in this study were prepared by dissolving $\text{InCl}_3 \cdot 2\text{H}_2\text{O}$ in deionized water followed by serial dilutions. 10 μL indium aliquots were pipetted into the graphite cuvette and the furnace temperature program was initiated. The graphite cuvette temperature was increased from

room temperature to 110 °C over a 10 s ramp then kept at 110 °C for a 30 s drying cycle. The graphite furnace supply's temperature setting at these low temperatures was calibrated using a thermocouple temperature meter (thermocouple module Model 80K with multimeter model 77, John Fluke Mfg. Co. Inc., Everett, WA, U.S.A.) since this temperature was below the range of the optical temperature sensor. For the emission measurements, the r.f. power was applied to the center electrode at 25 s along the drying cycle and left on throughout the entire atomization cycle. The atomization cycle was 5 s long and consisted of heating the cuvette to 1450 °C at the maximum heating rate provided by the furnace power supply, approximately 300 K/s, then held at that temperature for the remainder of the heating cycle.

Integration, or exposure, times of 0.3 s and a sampling frequency of 2 Hz were used in obtaining the spatially resolved studies reported in this chapter. Integration times of 5 s were used to obtain the temporally integrated results since temporally resolved studies showed that no significant amount of indium remained in the cuvette beyond 5 s.

4.3 Results and Discussion

Figs. 4.1A and B show the 303.94 nm line emission intensity from 10 ng indium samples in the FAPES source at different r.f. powers collected as described in section 4.2. For Fig. 4.1A, the emission data have been both spatially and temporally integrated to show the effect of r.f. power on the total analyte emission signal. For Fig. 4.1B, the emission data have been spatially integrated and the temporal evolution of the signal is shown for a series of r.f. powers.

These plots show that as the r.f. power is increased, there is an increase in the relative emission intensity of the indium line up to 40 Watts. Above 40 Watts, the emission intensity decreases as the r.f. power is increased. Hettipathirana [15] observed a similar trend for the emission from the Pb(I) 283.30 nm line. His data also showed an increase in emission intensity as r.f. power was increased to 50 Watts and a slight decrease in emission intensity as r.f. power was increased further. The main difference is that the Pb(I) emission intensity did not vary as much as the In(I) emission does with respect to power. Sturgeon et al. [5] found that the emission intensities for cadmium, copper and iron increased with increases in r.f. powers between 50 and 75 Watts.

The observation that emission intensities increase with r.f. power is consistent with equations 1.1 and 1.2 when the effect of r.f. power on the excitation temperature is taken into consideration. These equations show that emission intensity is proportional to the population of the excited state species from which the emission originates. The population of this excited state, in this case the $5d(2D_{3/2})$ state of indium, should be proportional to the Boltzmann factor, $e^{-(E_k/k_B T_{exc})}$ in equation 1.1, in the FAPES source. The Boltzmann factor is also shown as a function of r.f. power in Fig. 4.1A. The least-squares-line fitted to the Pb(I) excitation temperatures shown in Chapter 3, Fig. 3.14, were used to calculate the excitation temperatures as a function of r.f. power. Using these temperatures, the Boltzmann factor for the In(I) 303.94 nm line, whose E_k value is 32892 cm^{-1} [80], was then calculated as a function of r.f. power. Since the Boltzmann factor increases exponentially with r.f. power (though the curvature at these r.f. powers is minimal), the emission intensity should also increase with an increase in r.f. power. This is seen up to 40 Watts r.f. power.

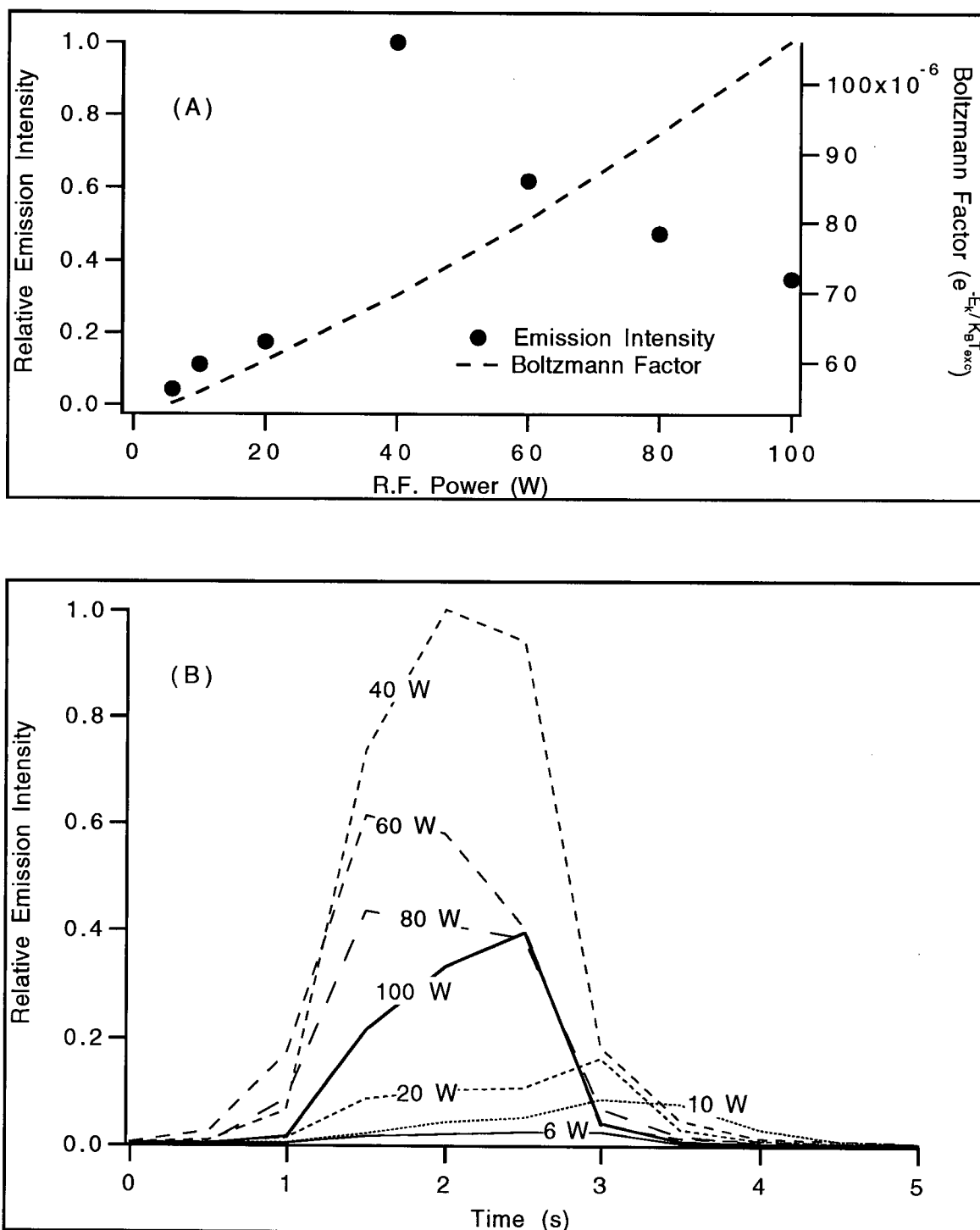


Fig. 4.1: Effect of r.f. power on the emission intensity of the In(I) 303.94 nm line from 10 ng of indium and on its Boltzmann factor.
 (A) shows the emission intensity as a function of r.f. power.
 (B) shows the emission intensity as a function of time.

At higher r.f. powers the excited state population can no longer be proportional to the Boltzmann factor since higher r.f. powers produce higher Boltzmann factors but lower $\ln(I)$ emission intensities. Thus the excited state population must be lowered by some other process. This attenuation was not caused by a detuning of the r.f. power supply since the reflected power remained below 2 Watts for the duration of the atomization cycle.

Hettipathirana [15] has postulated several possibilities to explain this signal attenuation at higher r.f. powers: analyte losses during pre-atomization, analyte loss during atomization, changes in excitation conditions and increases in analyte ionization. Experimental results reported in Chapter 5 show that analyte ionization is indeed a major cause of this signal attenuation and are discussed in detail in that chapter.

The temporal profiles of indium emission intensities plotted in Fig. 4.1B, while limited to a resolution of 0.5 s, show that increasing the r.f. power up to 40 Watts caused the indium signal to occur earlier. When the r.f. power was increased above 40 Watts, no further temporal shifts were observed in the emission signal. Temporal shifts in analyte emission peaks have been observed by Sturgeon et al. [5] who found that raising the r.f. power shifted emission signals from copper, beryllium and nickel to earlier times while a slight shift to later times was observed for cadmium. Hettipathirana and Blades [11] conducted a series of emission and absorption studies in order to explain temporal shifts in analyte signals as a function of r.f. power. Higher r.f. powers generally shifted emission peaks to earlier times. They concluded that this was caused by plasma assisted heating of the graphite surfaces and some possible increase in the excitation volume as a result of an expansion of the plasma. Double peaks were also observed and they concluded that silver, lead and

manganese condense on the center electrode at lower r.f. powers and higher concentration. This condensation-vaporization process has also been observed in GFAAS using platform atomization [90]. In Hettipathirana and Blades' FAPES source, higher r.f. powers were seen to reduce this condensation most likely by r.f. heating of the center electrode thus preventing it from being a condensation site.

Spatially and temporally resolved emission profiles for indium in the FAPES source are plotted in Figs. 4.2 to 4.8. These give a more detailed view of the analyte's behavior. The center electrode is seen as the minimum at the origin of the x-axis in these figures. It is clear from these profiles that the emission is not spatially homogenous and has a spatial structure that is time dependent. At each r.f. power setting used, the emission profile does not simply increase in intensity then decrease through the atomization cycle as shown in Fig. 4.1B. Initially, the analyte emission intensity increases at the lower half of the cuvette, represented as the negative side of the x-axis in the plots. The emission then evolves to fill the cuvette, though not uniformly, then decreases back to zero. There is a significant amount of spatial inhomogeneity at each temporal position.

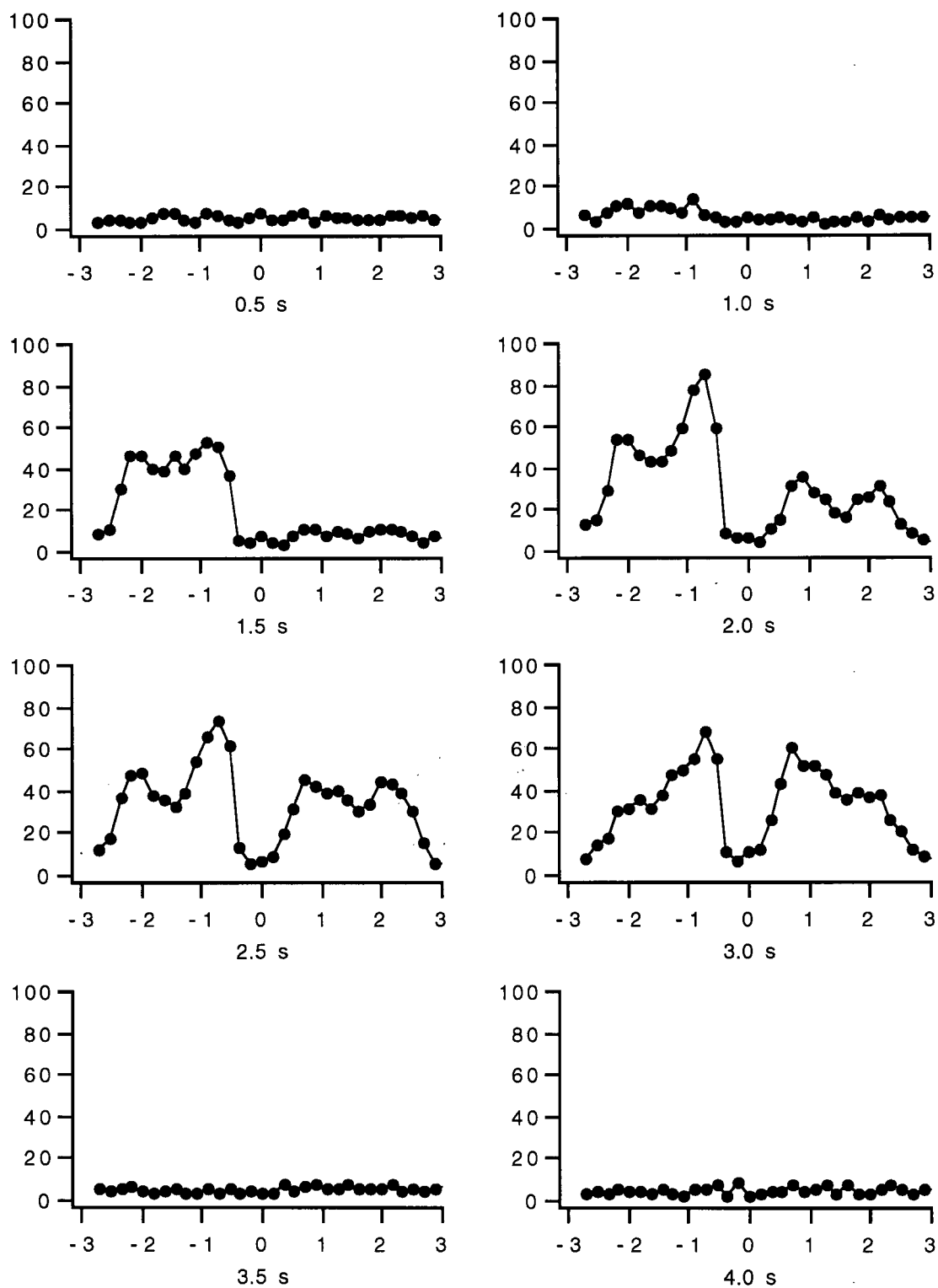


Fig. 4.2: Spatially and temporally resolved In(I) 303.94 nm line emission profiles from 10 ng indium with 6 Watts r.f. power. Plots are of emission intensity (in Counts Pixel⁻¹ s⁻¹) versus vertical position (in mm).

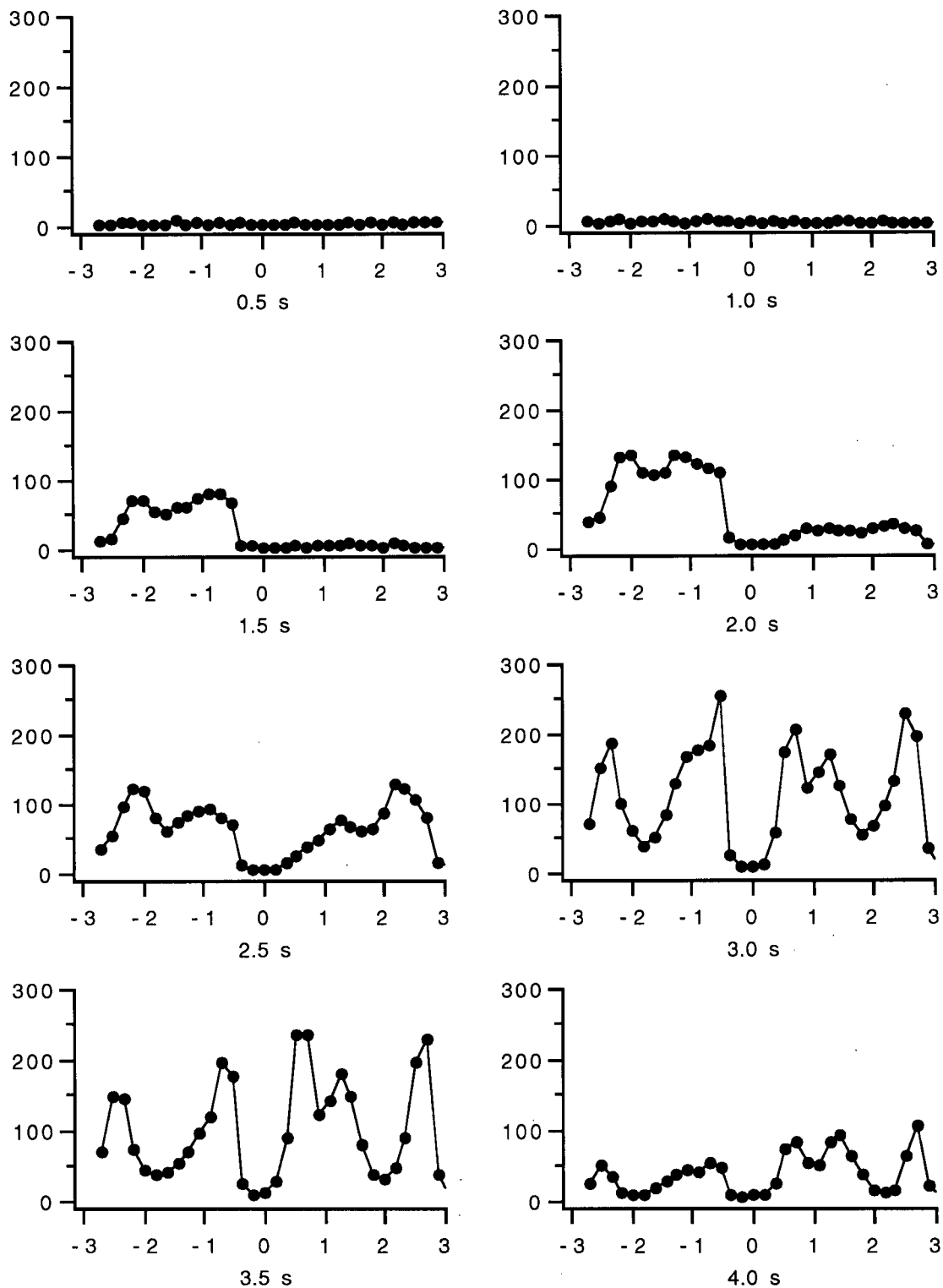


Fig. 4.3: Spatially and temporally resolved $\ln(I)$ 303.94 nm line emission profiles from 10 ng indium with 10 Watts r.f. power. Plots are of emission intensity (in $\text{Counts Pixel}^{-1} \text{ s}^{-1}$) versus vertical position (in mm).

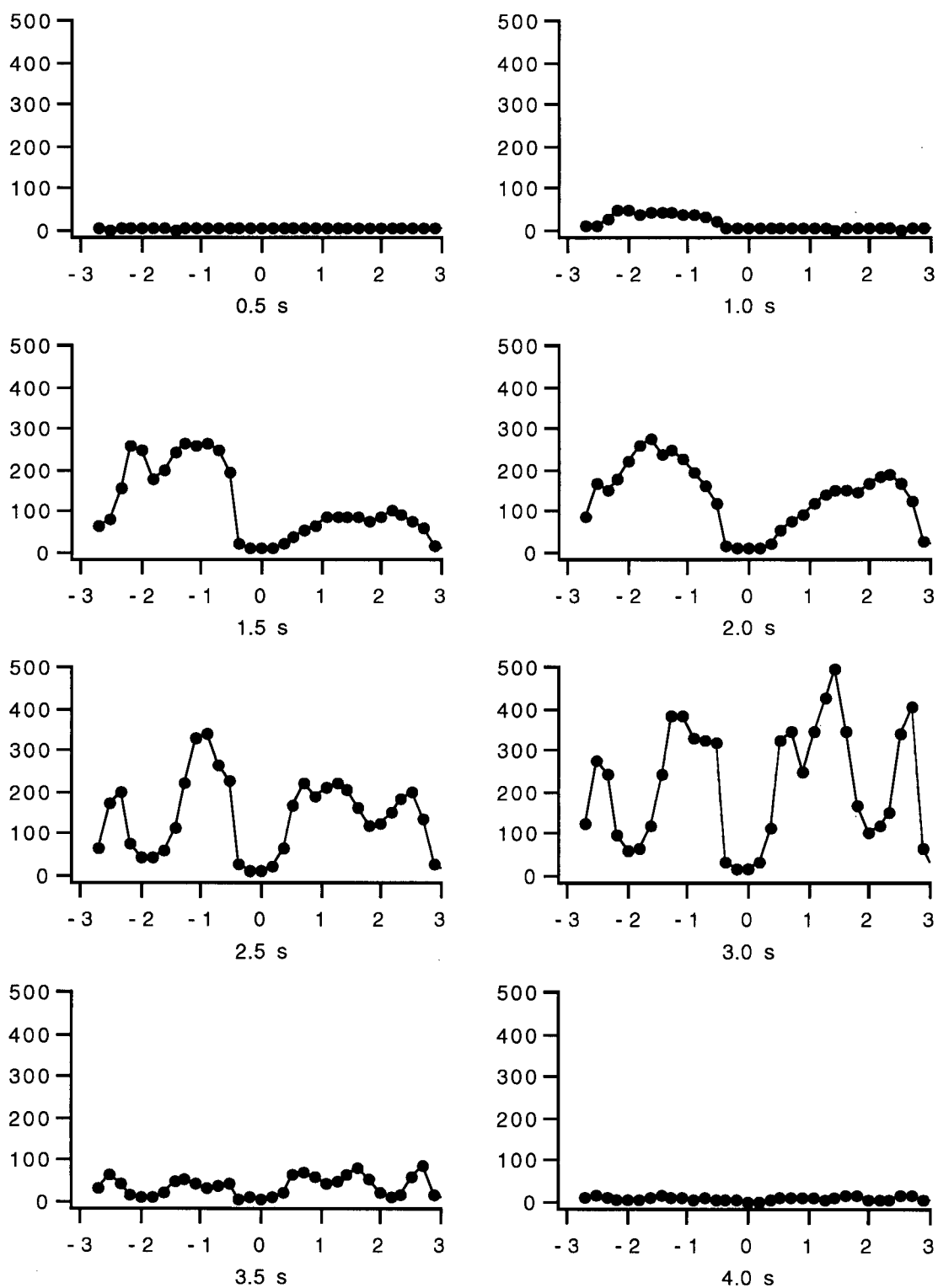


Fig. 4.4: Spatially and temporally resolved $\ln(I)$ 303.94 nm line emission profiles from 10 ng indium with 20 Watts r.f. power. Plots are of emission intensity (in Counts Pixel⁻¹ s⁻¹) versus vertical position (in mm).

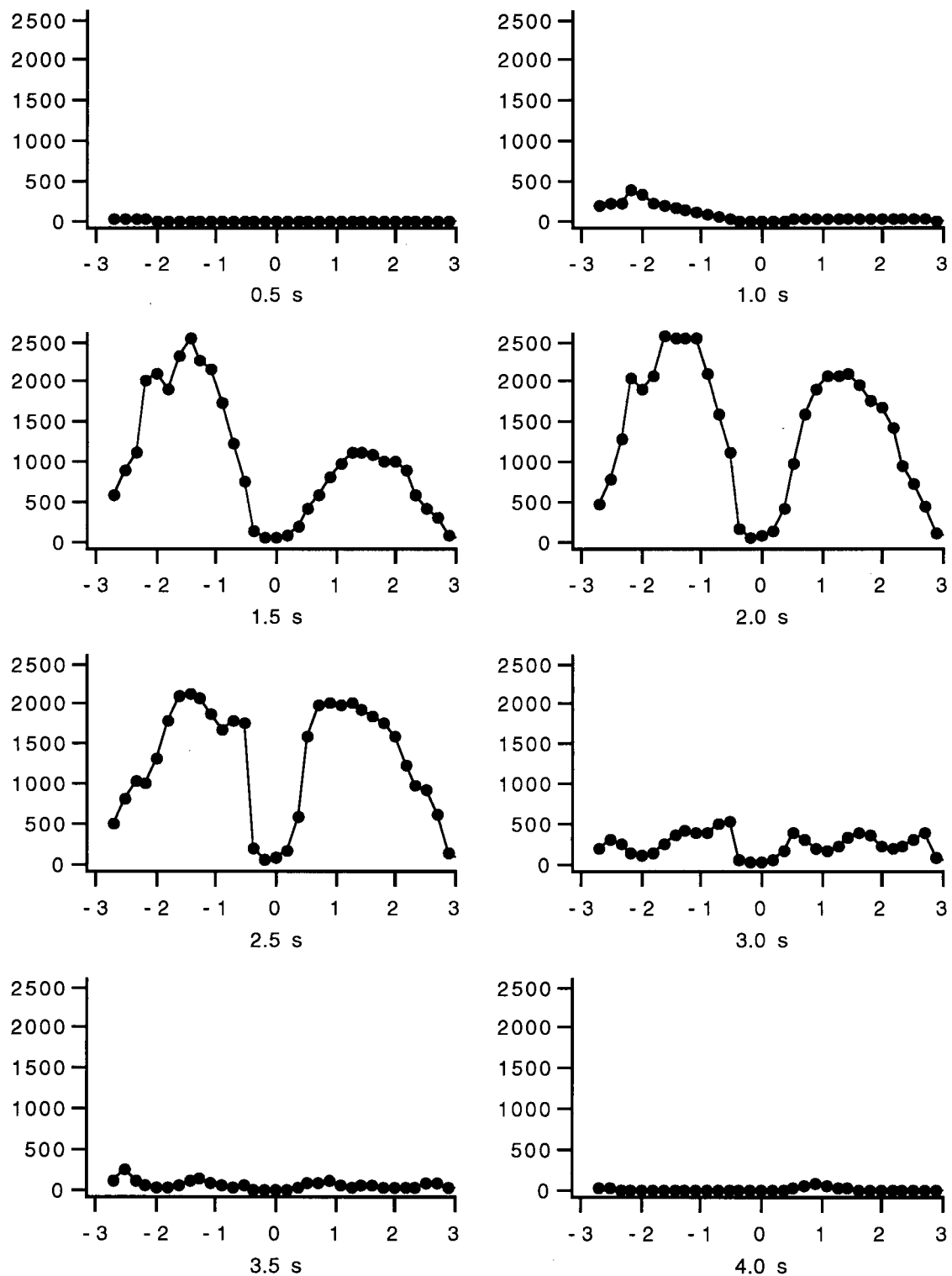


Fig. 4.5: Spatially and temporally resolved In(I) 303.94 nm line emission profiles from 10 ng indium with 40 Watts r.f. power. Plots are of emission intensity (in Counts Pixel⁻¹ s⁻¹) versus vertical position (in mm).

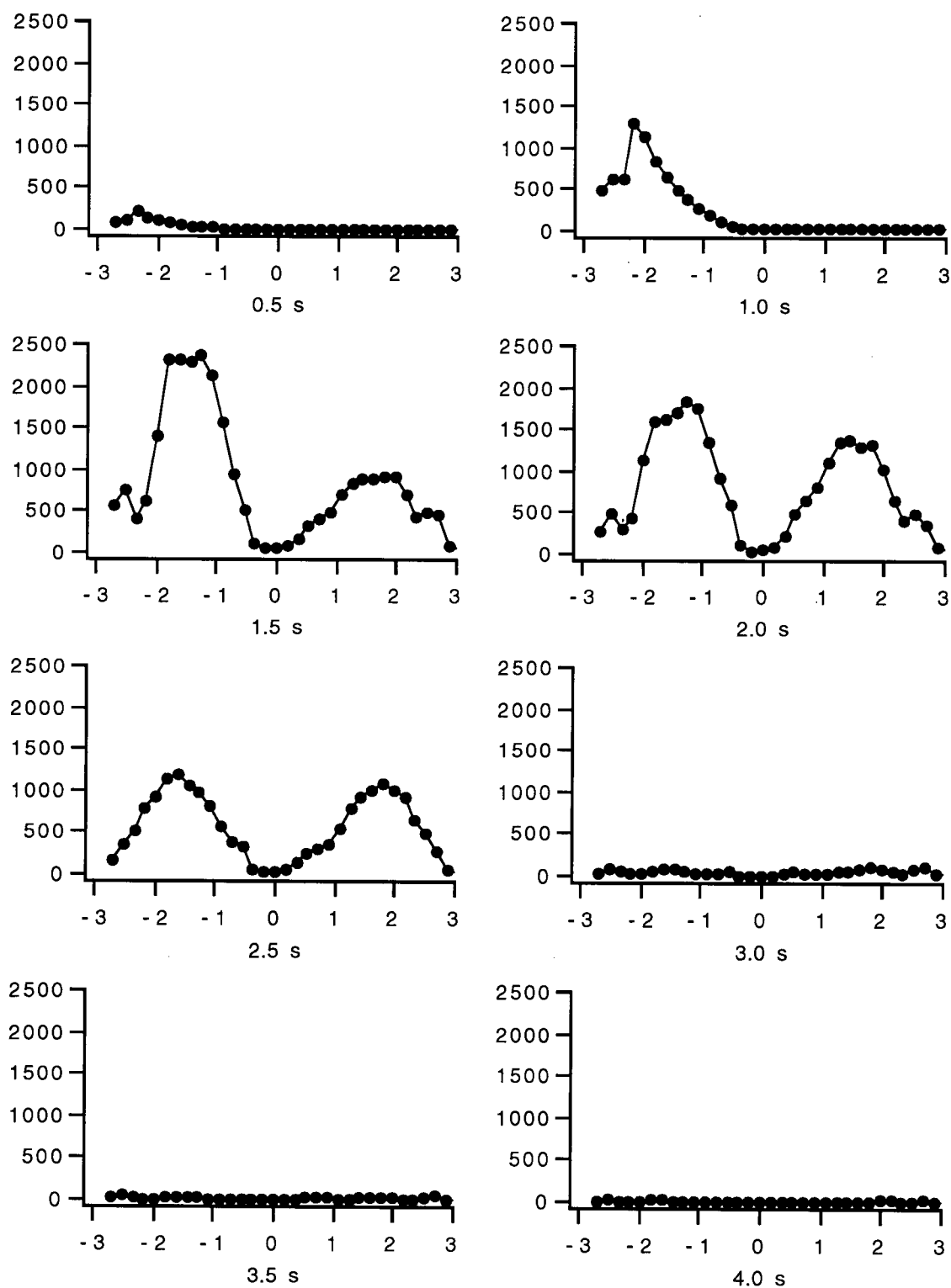


Fig. 4.6: Spatially and temporally resolved In(I) 303.94 nm line emission profiles from 10 ng indium with 60 Watts r.f. power. Plots are of emission intensity (in Counts Pixel⁻¹ s⁻¹) versus vertical position (in mm).

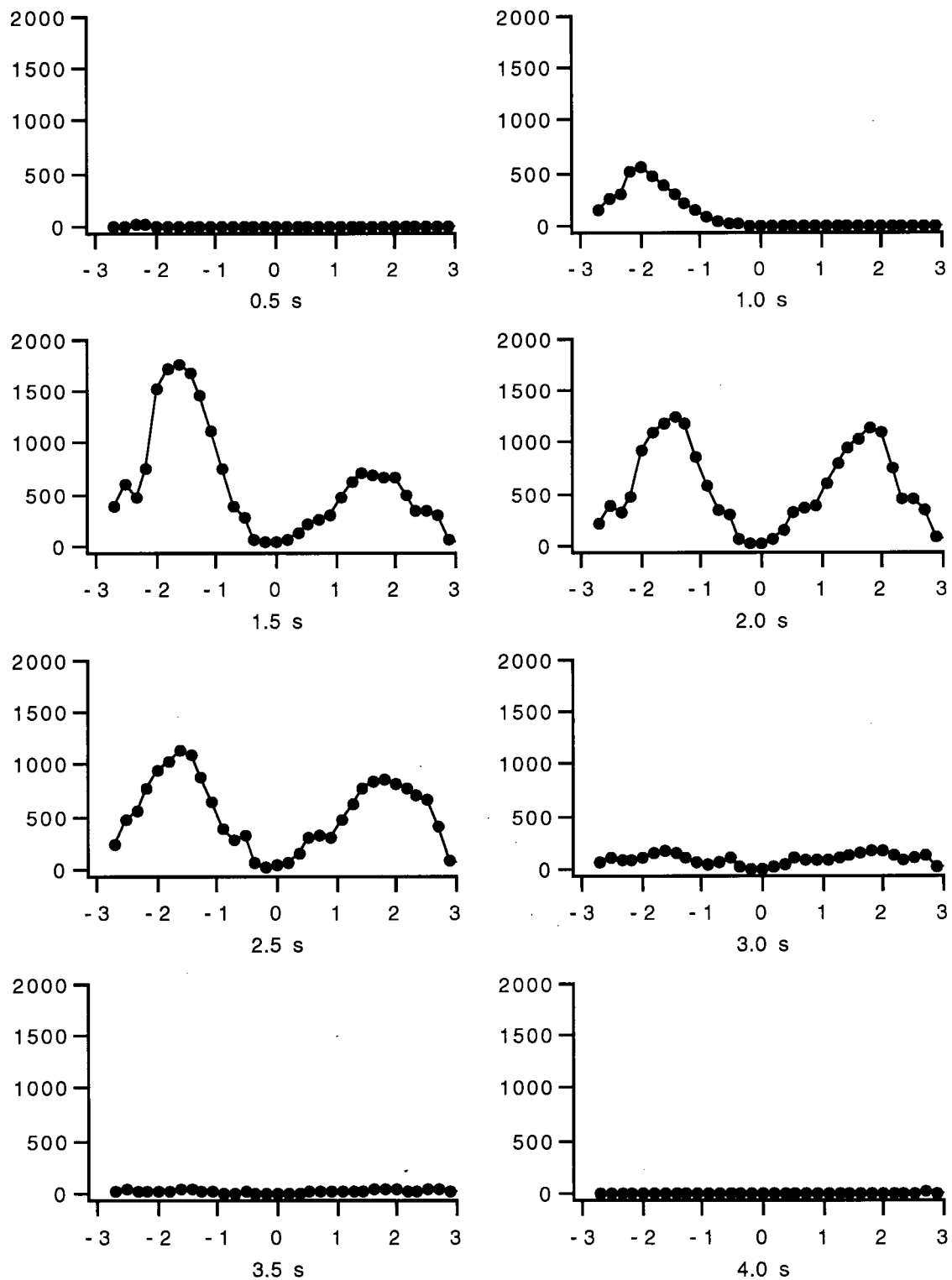


Fig. 4.7: Spatially and temporally resolved In(I) 303.94 nm line emission profiles from 10 ng indium with 80 Watts r.f. power. Plots are of emission intensity (in Counts Pixel⁻¹ s⁻¹) versus vertical position (in mm).

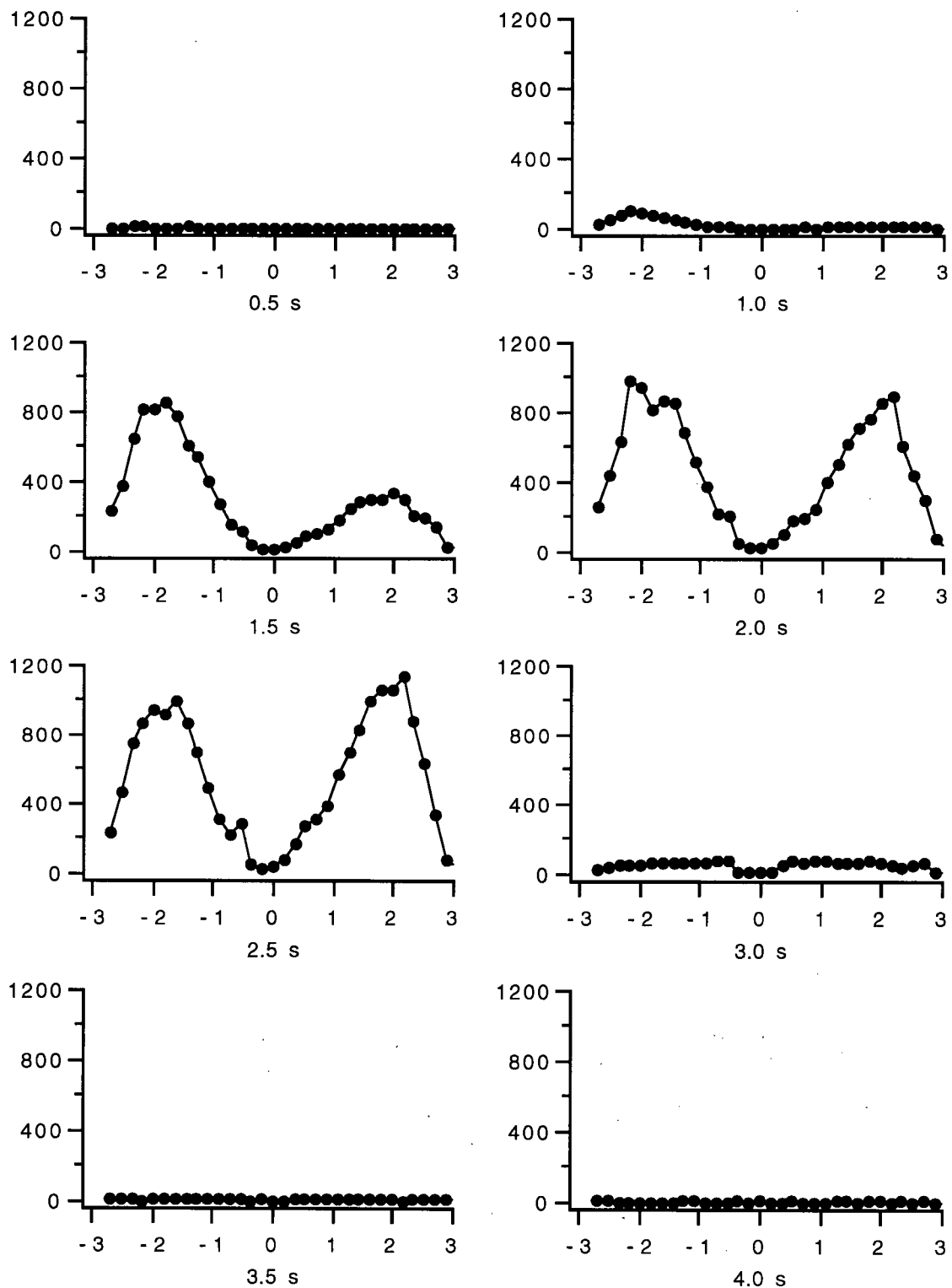


Fig. 4.8: Spatially and temporally resolved In(I) 303.94 nm line emission profiles from 10 ng indium with 100 Watts r.f. power. Plots are of emission intensity (in Counts Pixel⁻¹ s⁻¹) versus vertical position (in mm).

Fig. 4.2. is a series of plots of the spatially resolved temporal evolution of the indium emission signal in the FAPES source with 6 Watts r.f. power applied to the center electrode. The emission signal increases first at the bottom of the cuvette. At 1 s this signal appears to have three maxima. One maximum is adjacent to the center electrode, a second is adjacent to the cuvette wall and a third is halfway between these two at a radius of about 1.5 mm. At 1.5 s, the emission from the bottom of the cuvette has increased while retaining its spatial structure containing three maxima. There is some slight emission from the top half of the cuvette though this is only about 10% as intense as the emission from the bottom half of the cuvette. At 2.0 s, the emission adjacent to the center electrode and adjacent to the cuvette wall has increased and the maximum at a radius of 1.5 mm is no longer apparent. A similar emission structure occurs above the center electrode though its intensity is still only about one quarter that of the emission below the center electrode. At 2.5 s, the emission has remained essentially the same with the emission above the center electrode now almost equal to that below the center electrode. At 3.0 s, the emission seems to be located more adjacent to the center electrode decreasing in intensity with increasing radius. A slight maximum is still seen adjacent to the cuvette wall. The emission signal is essentially gone by 3.5 s.

Fig. 4.3 shows the spatially resolved temporal evolution of the indium emission signal with 10 Watts r.f. power. At this slightly higher r.f. power, the temporal evolution of the emission intensity signal shows a similar trend to the emission intensity in the 6 Watt plasma. The emission intensity first increases below the center electrode before filling the cuvette. The emission intensity at 4.5 s is not shown on this figure for consistency but was essentially at the background level. At this r.f. power the maxima adjacent to the center electrode

and cuvette wall are sharper, namely the relative intensity differences between the maxima and minima are greater than in the 6 Watt plasma. The maximum which was at a radius of about 1.5 mm in the 6 Watt plasma is at a radius of about 1.25 mm and does not get buried by the other two maxima at 2.0 s. It is seen clearly throughout the temporal evolution of the emission signal.

Fig. 4.4 shows the spatially resolved temporal evolution of the indium emission signal with 20 Watts r.f. power. At this r.f. power the emission intensity from the maximum at a radius of 1.25 mm becomes slightly higher than that of the maxima adjacent to the center electrode and cuvette wall. The emission above the center electrode occurs earlier than in the lower power plasmas. At 40 Watts r.f. power, Fig. 4.5, the maximum at a radius of 1.25 mm is quite broad and is extended further outwards towards the emission intensity maximum adjacent to the cuvette wall compared to the 20 Watt plasma. At 60 Watts r.f. power, Fig. 4.6, this intermediate maximum has essentially enveloped the maximum adjacent to the center electrode at all times and has enveloped the emission maximum adjacent to the cuvette wall at 2.5 s. At earlier times its intensity is about 3 times that of the maximum adjacent to the cuvette wall. Pavski *et al.* [22] have collected temporally resolved emission images of the atomization of silver in a FAPES source at 30, 50 and 70 Watts r.f. power. While their study was aimed at investigating the effects of r.f. power on the condensation of analyte on the center electrode, their data do show similar spatial and temporal structure as that shown here.

At higher r.f. powers of 80 and 100 Watts, shown in Figs. 4.7 and 4.8, the same trend can be seen. The intensity of the intermediately located peak is much greater than that of the two peaks adjacent to the center electrode and cuvette wall. This intermediate peak is now located nearer the cuvette wall than

its location at lower r.f. powers. Fig. 4.9 shows this effect more clearly; it contains two plots of the same data shown in Figs. 4.1 to 4.8 though in this figure the spatially resolved data has been summed over each acquisition time. Fig. 4.9A shows the relative intensity of the analyte emission at different r.f. powers; Fig. 4.9B shows the same data after it has been area normalized. This figure also shows, as does Fig. 4.1, that as the r.f. power is increased up to 40 Watts there is an increase in emission intensity from the In(I) 303.94 nm line. Increasing the r.f. power further up to 100 Watts causes a decrease in the emission intensity. Besides causing a change in the magnitude of the emission intensity, increasing the r.f. power also causes a change in the emission intensity's spatial profile within the cuvette. As the r.f. power is increased the emission from the analyte moves away from the center electrode towards the cuvette wall.

The spatial inhomogeneity of the intensity of the analyte emission and its dependence on the r.f. power must be caused by a change in the spatial distribution of the analyte's excited state population. This is obvious from equation 1.2 which shows that emission intensity is proportional to N_k , the population of the excited state. This population is in turn proportional to the ground state analyte population and dependent on the excitation ability of the plasma. Thus the complex spatial structure observed in the In(I) emission profiles shown previously must be due to the ground state distribution of analyte atoms or to non-homogeneous excitation within the source. The former can be checked by determining the spatial distribution of the analyte ground state atoms. This distribution was determined by measuring spatially resolved atomic absorption profiles of indium using the 303.94 nm resonance line as described in the experimental section of this chapter.

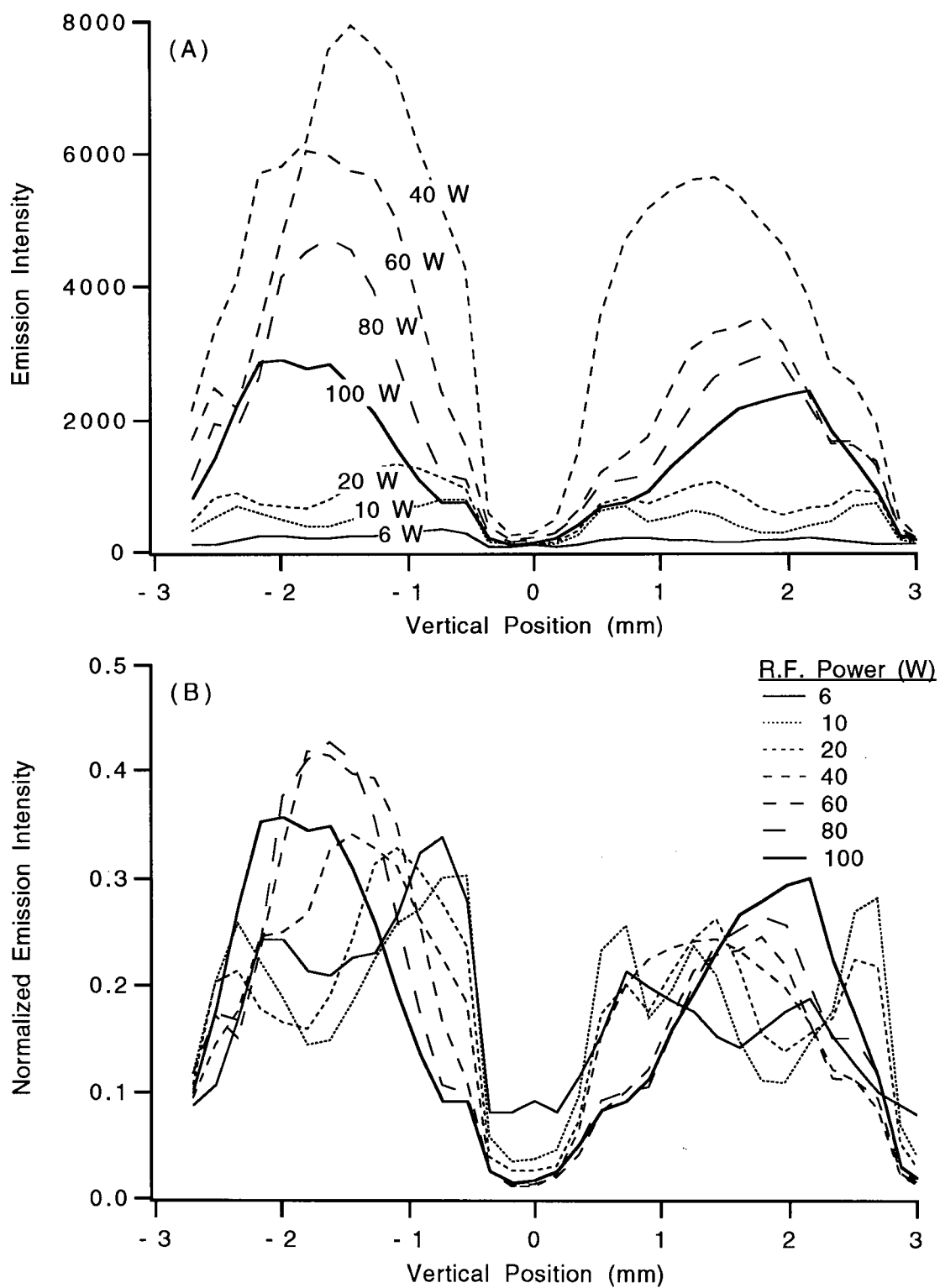


Fig. 4.9: Temporally integrated spatially resolved In(I) 303.94 nm emission intensity at various r.f. powers. (A) represents relative emission intensity and (B) represents the area normalized emission intensity.

Spatially and temporally resolved absorbance profiles for 10 ng of indium in a 20 Watt plasma were measured as described in section 4.2. The first data set collected was the emission from the 303.34 nm In(I) line and is shown in Fig. 4.10. It should be noted that for this set of data the plasma remained on throughout the entire atomization cycle and the reflected power only rose after the current to the graphite cuvette was turned off. This figure is similar to Fig. 4.4 described above but represents data collected several weeks later with a different center electrode and graphite cuvette. The slight variations in the spatial profiles compared to Fig. 4.4 were caused mainly by the fact that a new cuvette and center electrode were used and by the long term drift in atomization temperature used. The spatial profile of the indium hollow cathode lamp intensity was then measured through the atomization cycle with no indium sample. Fig. 4.11 is a plot showing a typical resulting spatial profile, the net lamp intensity profile, for the data collected at 3.0 s in the atomization cycle. The net lamp intensity spatial profile for each atomization time was essentially the same as that shown for 3.0 s.

The inhomogeneity in this profile can be caused either by the spatial structure of the emission intensity from the indium hollow cathode lamp or by the blocking off of the incident beam by the graphite cuvette, center electrode and its holding clamp. Gilmudinov *et al.* [92] have shown that the spatial profile for hollow cathode lamps with small diameters, as was used in this study, is approximately parabolic with maximum intensity at the center of the hollow cathode. Thus while this does contribute to the spatial structure observed, most of the detailed structure is more likely caused by the obstruction of the incident beam. The two sides of the profile are obviously attenuated by the cuvette wall. The center minimum is caused by the incident beam being blocked by the

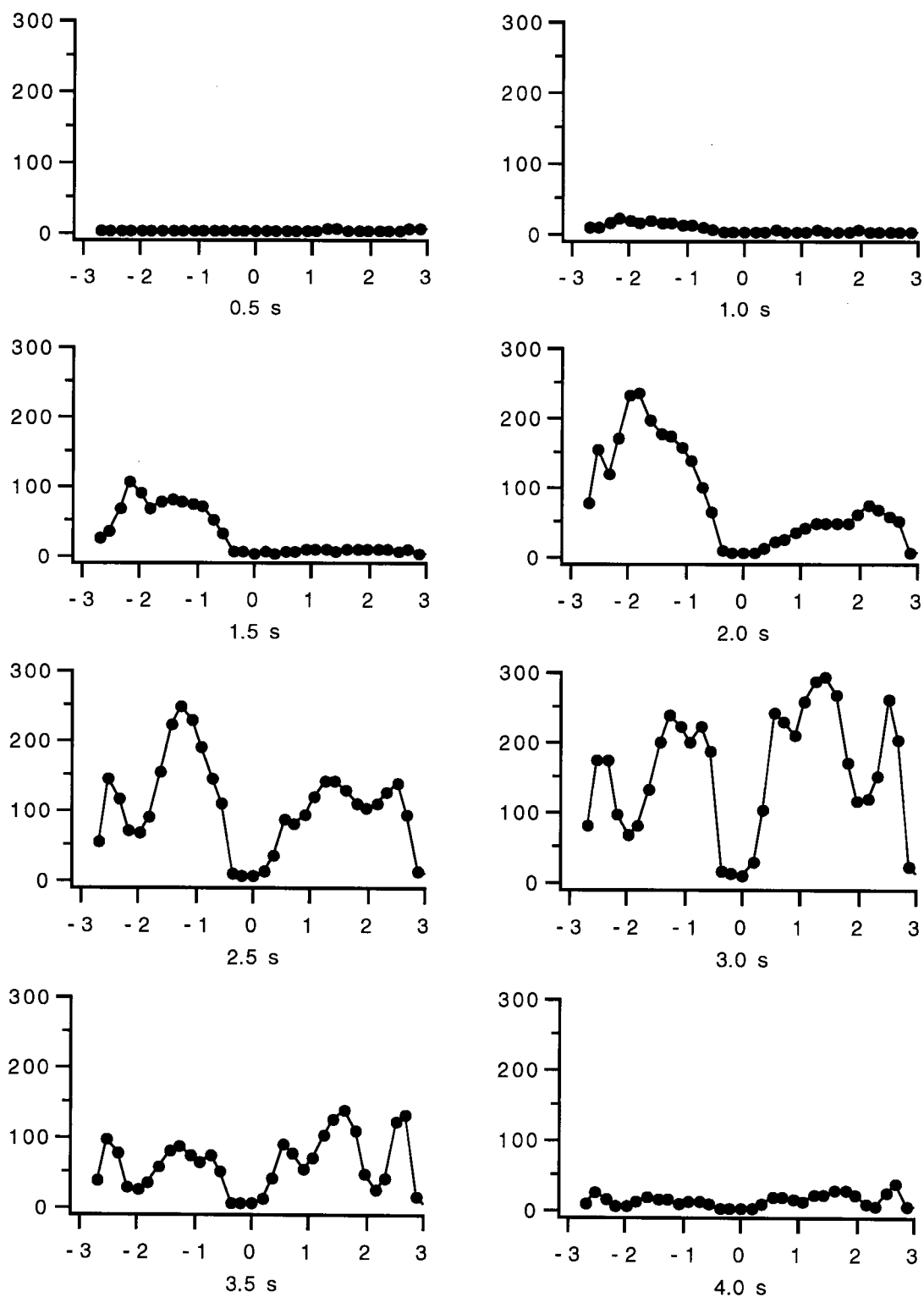


Fig. 4.10: Spatially and temporally resolved $\ln(I)$ 303.94 nm line emission profiles from 10 ng indium with 20 Watts r.f. power. Plots are of emission intensity (in Counts Pixel⁻¹ s⁻¹) versus vertical position (in mm).

center electrode. The center electrode clamp blocks out the incident beam as well resulting in a local intensity maximum at a vertical position of about 0.9 mm and a minimum adjacent to it at 1.25 mm.

The absorption profiles, which show the spatial distribution of the signal I in equation 4.1, were made more complex by the attenuation described above. Fig. 4.12 is a plot of a typical absorption profile obtained from 10 ng of indium in a 20 Watt plasma at 3.0 s in the atomization cycle. The absorption of the 303.94 nm lamp radiation is significant and can be seen in the difference between Fig. 4.11 and Fig. 4.12. Absorbance profiles were calculated from similar absorption profiles together with the net lamp intensity profile as described in section 4.2 using equation 4.1. These are shown in Fig. 4.13 and since the resonance line absorbance signal of an analyte is proportional to its ground state population, these represent the spatial and temporal distribution of the analyte ground state atoms.

One noticeable difference between the indium absorbance profiles and the emission profiles are the appearance times of the signal. Fig. 4.14, a plot of the temporally resolved spatially averaged absorbance and emission signals, shows that the emission signals occurs earlier than the absorbance signal. The reason for this difference is that for the absorbance signals there was no r.f. power to the center electrode. With r.f. power applied to the center electrode, there must be some plasma heating of the cuvette thus causing the analyte to atomize earlier than when no r.f. power is applied to the electrode. This effect has been studied more thoroughly by Hettipathirana and Blades [11] as described earlier.

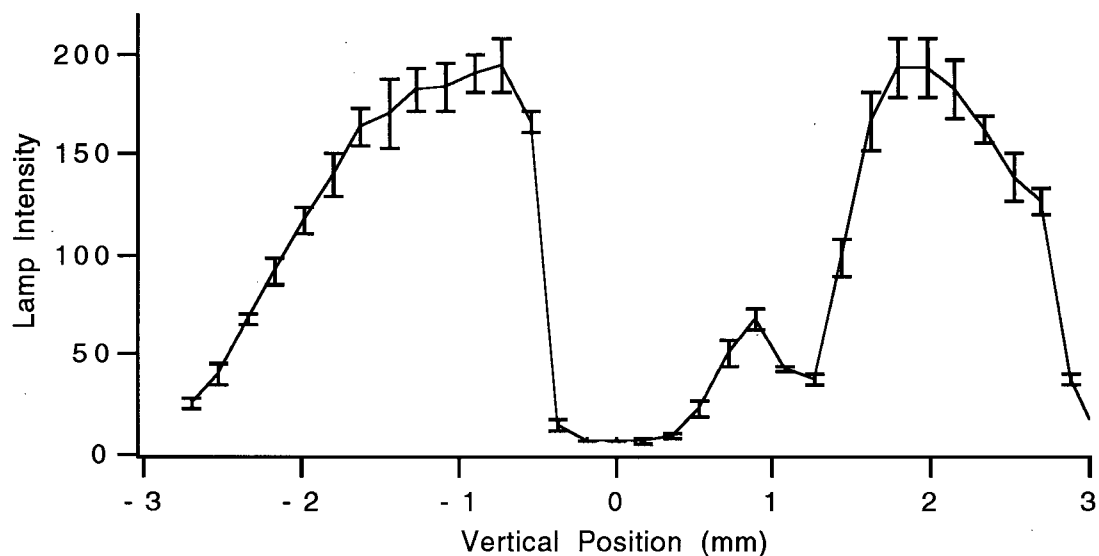


Fig. 4.11: Indium lamp 303.94 nm spatial emission profile after passing through the furnace. Plot is of emission intensity (in Counts Pixel⁻¹ s⁻¹) versus vertical position (in mm).

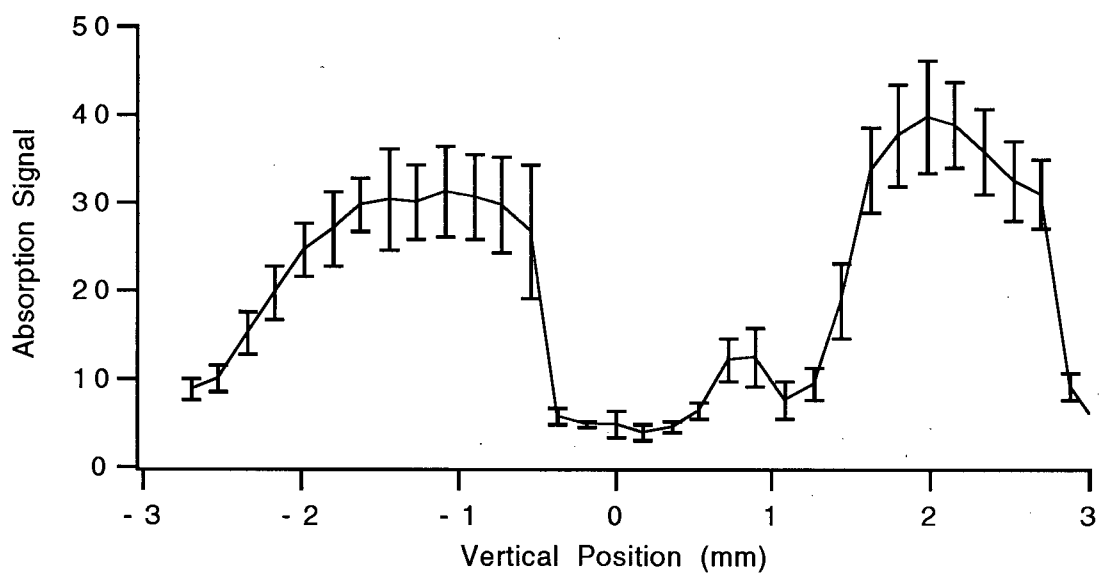


Fig. 4.12: Indium absorption profile at 303.94 nm for 0.3 s integration at 3.0 s in the atomization cycle. Error bars represent ± 1 standard deviation (5 samples).

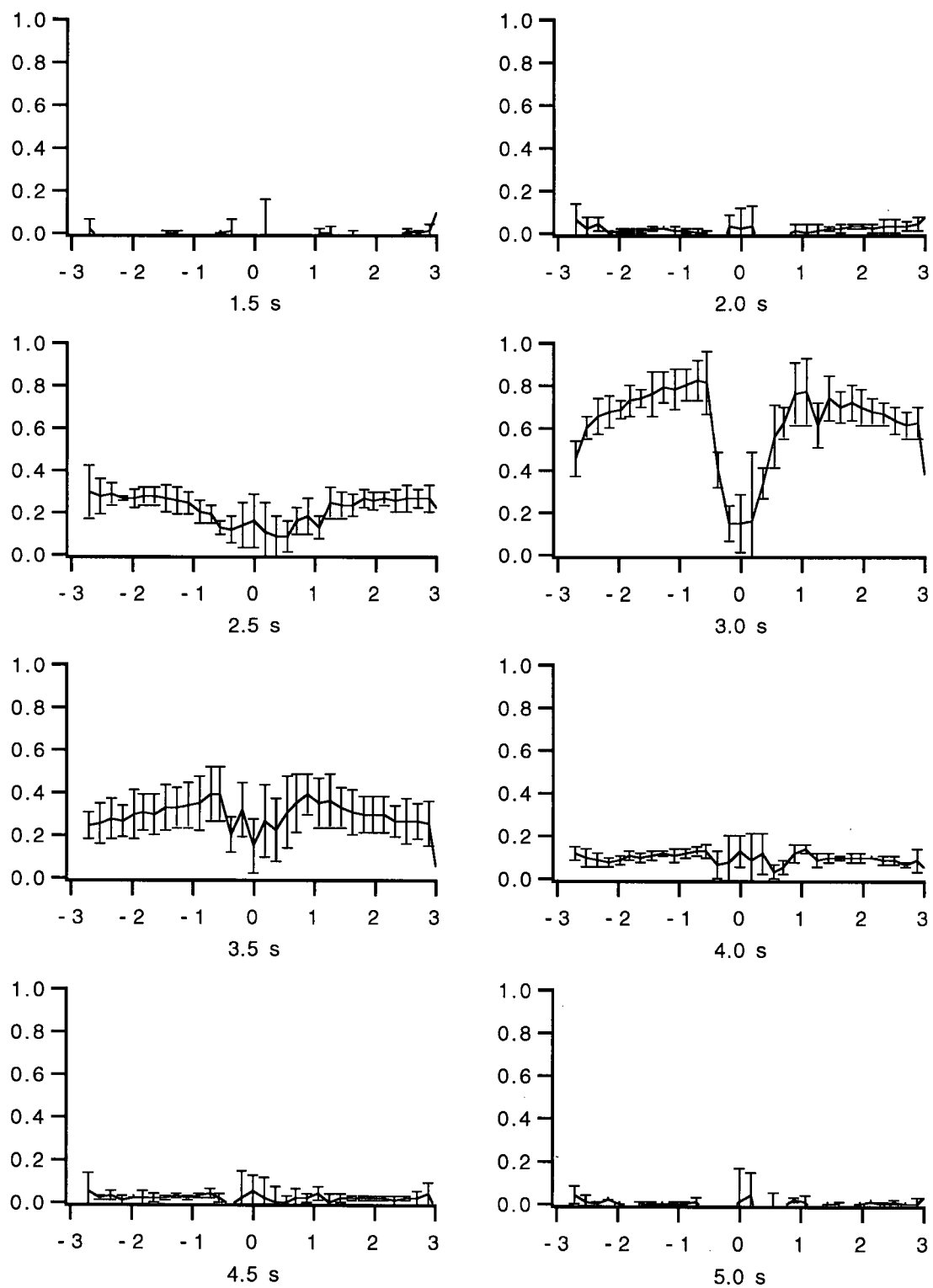


Fig. 4.13: Absorbance profiles for 10 ng indium samples at 303.94 nm. Integration time was 0.3 s. Plots are of absorbance versus vertical position in mm. Error bars represent ± 1 standard deviation (5 samples).

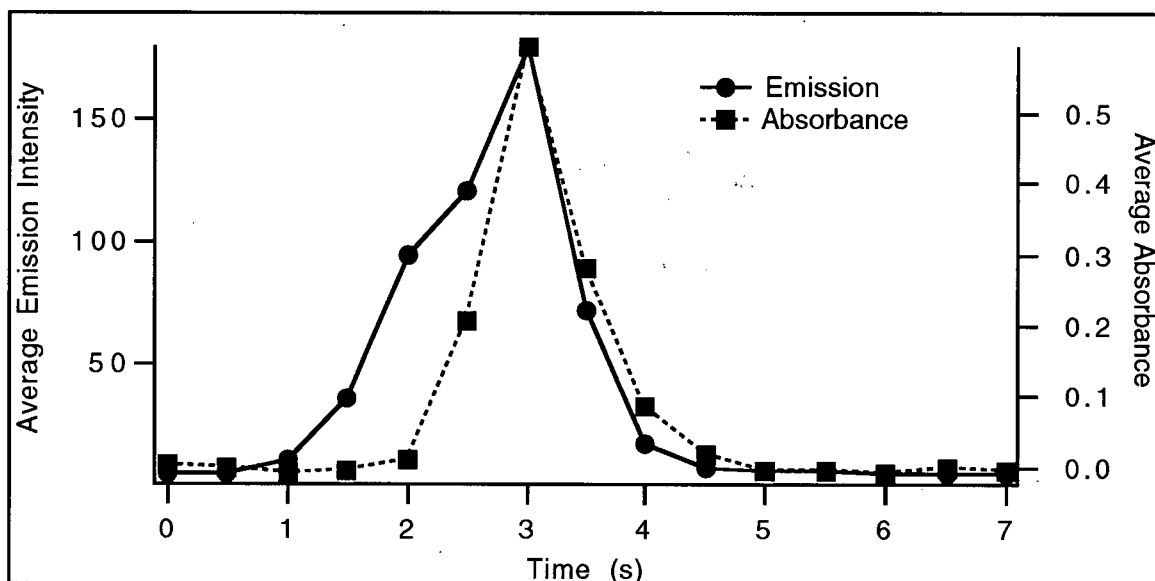


Fig. 4.14: Spatially averaged emission and absorbance signal as a function of time for 10 ng of indium in a 20 Watt FAPES.

In the absorbance profiles, as with the emission profiles, there is also some degree of spatial inhomogeneity, however, the absorbance profiles are significantly different than the emission profiles. The absorbance profiles have much less structure. At 3.0 s into the atomization cycle, where the maximum absorbance occurs, the analyte's spatial distribution within the cuvette is quite uniform. There is a maximum adjacent to the center electrode that drops off only slightly at higher radii. The absorbance profiles are much more uniform than the emission profiles. Since these absorbance profiles are essentially indium ground state population profiles, the inhomogeneity, or structure, in the analyte emission profiles must reflect the excitation conditions within the plasma.

If the FAPES source is considered a r.f. glow discharge, as proposed in Chapter 3, then the emission maxima adjacent to the center electrode and cuvette wall correspond to the negative glow [53]. No cathode dark space is seen between this glow and the electrodes which is expected for an atmospheric pressure source [54]. Adjacent to these negative glows are Faraday dark spaces. The intermediate emission zone between the Faraday dark spaces corresponds to the positive column.

4.4 Summary and Conclusions

The indium emission and absorption plots shown in Figs. 4.1 to 4.14 make it clear that the spatial structure observed in the analyte emission intensities is due to two effects. The first is the analyte population distribution within the source. This has been shown to have a slight gradient which is not very significant. The second effect is the dependence of the excitation ability of the plasma on position within the cuvette. The plasma's structure reflects the fact that it appears to operate as an atmospheric pressure r.f. glow discharge. As such, there are certain characteristics that glow discharges have that can be readily measured spectroscopically. One is the emission intensity from analyte atoms which has been shown in this chapter. Another characteristic is the spatial distribution of ionized particles within the source. This will be shown in Chapter 5. A third characteristic of glow discharges is the dependence of their geometry on the pressure. Chapter 6 contains the result of reduced pressure studies which agree with the proposal that the FAPES source operates as a glow discharge.

CHAPTER 5

ANALYTE IONIZATION IN THE FAPES SOURCE

5.1 Introduction

In Chapter 3 it was shown that increasing the r.f. power applied to the center electrode increased both the atomic excitation and the molecular rotational temperature within the FAPES source. This increase in temperature has a complex effect on the emission intensity from atomic and molecular species that is spatially dependent. In Chapter 4, the effect of r.f. power on the temporal and spatial profiles of indium atomic emission was shown. The spatially and temporally integrated indium atomic emission was found to increase with increasing r.f. power up to about 40 Watts. Further increases in applied r.f. power resulted in a decrease in the atomic emission signal. One possible explanation for this observation is that at higher r.f. powers there may be an increase in the ionization of analyte atoms. In order to determine if this is the case, the relationship between the degree of ionization of an analyte and r.f. power applied to the center electrode was investigated.

5.2 Experimental

5.2.1 Background

The degree of ionization of an analyte in an analytical plasma can be calculated from the relative intensity of atomic and ionic emission lines from this analyte. If equations 1.1 and 1.2 are applied to an ionic and atomic emission line from this element, the following can be derived:

$$\frac{N_o \text{ ion}}{N_o \text{ atom}} = \left(\frac{I\lambda g_o}{gA} \right)_{\text{ion}} \left(\frac{gA}{I\lambda g_o} \right)_{\text{atom}} e^{(E_{\text{ion}} - E_{\text{atom}}) / k_B T} \quad (5.1)$$

From the value of this ratio the degree of ionization of the analyte can be calculated as:

$$\% \text{ Ionization} = \frac{\left(\frac{N_o \text{ ion}}{N_o \text{ atom}} \right)}{\left(1 + \frac{N_o \text{ ion}}{N_o \text{ atom}} \right)} \times 100 \quad (5.2)$$

Knowledge of the degree of ionization in an analytical plasma is useful since it is very sensitive to changes in operating conditions. Once the plasma has been optimized for use, the degree of ionization can be used to monitor, and in fact verify, the operating parameters of spectrochemical analytical r.f. plasmas.

5.2.2 Instrumental Parameters

The imaging lens system used to image the source onto the entrance slit of the monochromator was the same as that described in sections 2.1.2.1 and 4.2.2 using the two plano-convex lenses with a 3 mm diameter aperture placed on the collimating lens. The CCD pixels were also binned as in the studies

reported in Chapter 4 resulting in f/50 imaging optics. With this instrumental arrangement, it was possible to collect spectrally, spatially, and temporally resolved emission data simultaneously for three magnesium emission lines. The 1200 lines/mm grating was installed in the monochromator for the emission measurements and its slit width was set to 30 μm except for the data shown in Fig. 5.4 where the 3600 lines/mm grating was used since increased spectral resolution was desired. The slit width of 30 μm was maintained.

5.2.3 Procedure

Magnesium was chosen as the spectrometric species to investigate ionization in the FAPES source for both practical and fundamental reasons. First, it was necessary to choose an element whose appearance temperature in the FAPES source was within the operating range of the experimental instrumentation used for this study. Second, an element which possesses both an atomic and ionic emission line in the FAPES source with wavelengths that fell within one spectral window of the CCD detector was required. Finally, calculations of the degree of ionization of an element requires the use of several parameters, shown in equation 5.1, whose values must be known with sufficient accuracy. Magnesium fulfills these requirements having an atomic emission line at 285.21 nm and two ionic emission lines at 280.27 nm and 279.55 nm whose transition probabilities are known with sufficient accuracy [93]. The appearance temperature of magnesium in graphite furnaces is approximately 1530 K [91] which is within the operating range of this FAPES source.

The Cube source described in section 2.1.1.2 was used in the measurements reported in this chapter. For all of the magnesium emission

measurements, 10 μL aliquots of a magnesium solution of the appropriate concentration were pipetted onto the inside wall of the graphite cuvette. These were prepared by dissolving MgO in deionized water. The graphite furnace temperature program was then initiated. The magnesium emission measurements were made using the same FAPES technique as the one used to measure indium emission and has been described earlier in section 4.2.3. Integration times of 5 s were used to measure the emission intensities.

5.3 Results and Discussion

5.3.1 Effect of Magnesium Load on Mg(I) and Mg(II) Emission Line Intensities

Magnesium calibration plots for the Mg(I) 285.21 nm and the Mg(II) 280.27 nm and 279.55 nm emission lines are shown in Figs. 5.1 and 5.2. While detection limits and linear dynamic ranges can be deduced from these plots it should be noted that the experimental system was optimized for the measurement of spatial profiles and not for the determination of analytical figures of merit. Under these conditions, described in section 5.2, the calibration plot for the Mg(I) 285.21 nm emission line bends towards the Mg load axis at loads as low as 1 ng. A log-log calibration plot, shown in Fig. 5.2, can be used to quantify the degree of non-linearity in the response function measured, in this case the emission intensity from Mg(I) and Mg(II) versus magnesium load.

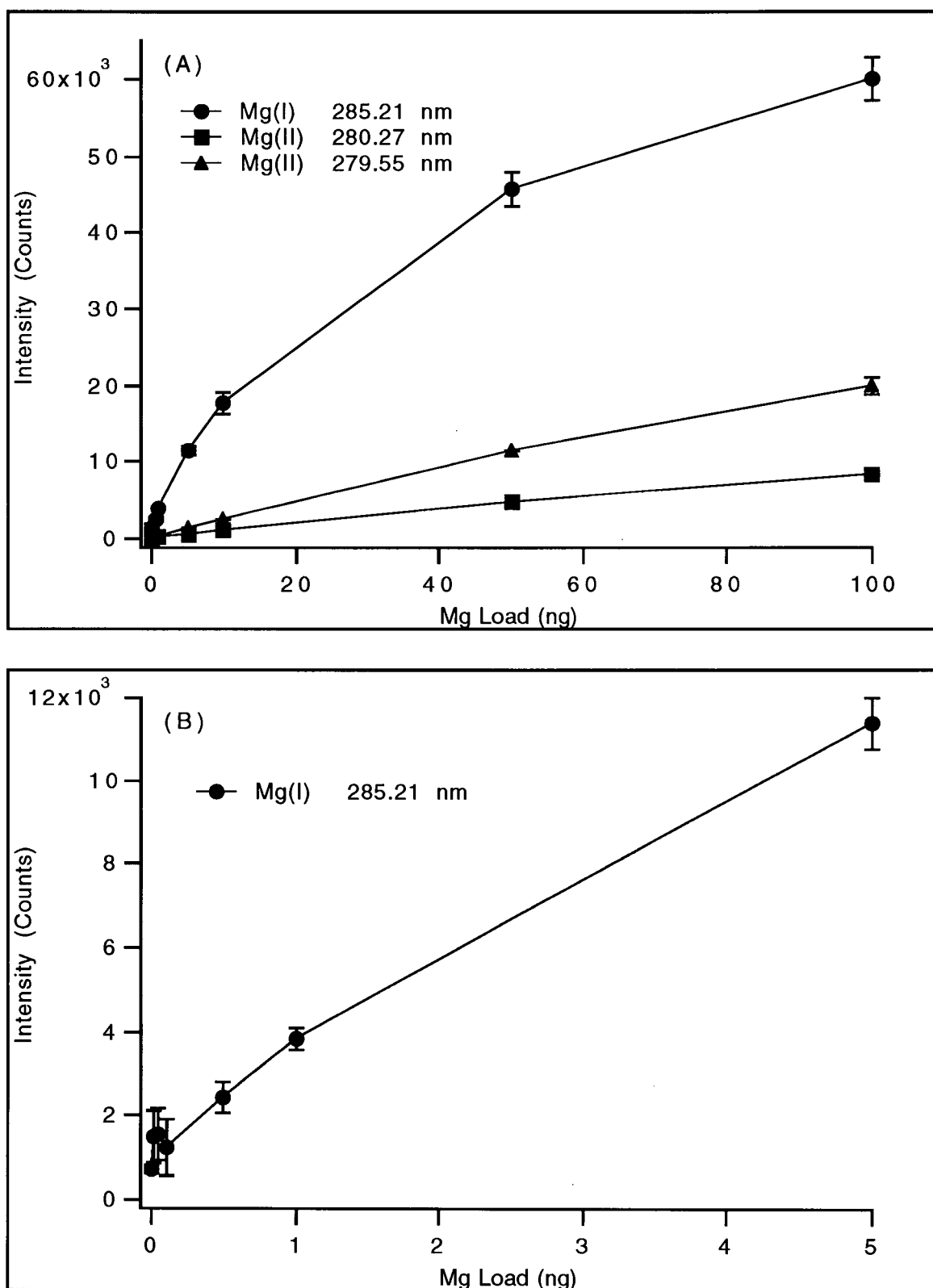


Fig. 5.1: Calibration plots for magnesium with 20 Watts r.f. power. Error bars represent ± 1 standard deviation (5 samples).

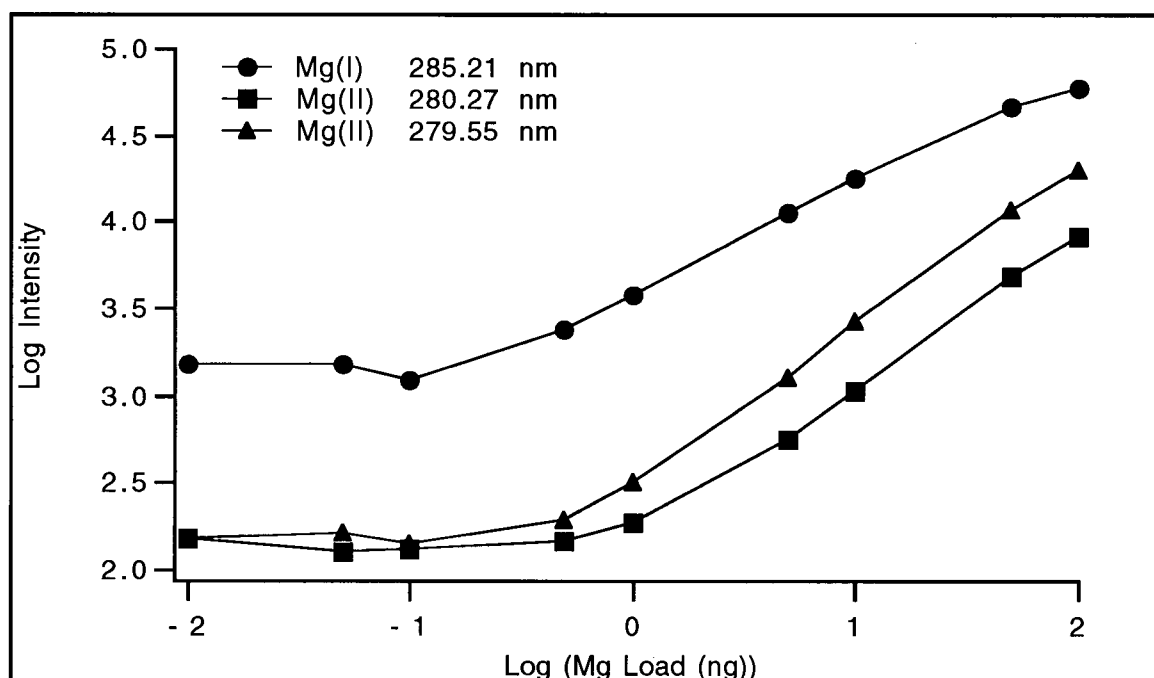


Fig. 5.2: Log-log magnesium calibration plots with 20 Watts r.f. power.

For data that result in a straight line with a positive slope, a log-log plot results in a straight line whose slope is equal to 1. A straight line log-log plot can also result from data whose two variables are proportional to powers of each other. In this case the slope of the line is equal to the ratio of these powers and can be used as a measure of the degree of curvature in the original plots. In Fig. 5.2 the log-log plots have two linear sections. Below 0.5 ng these plots have a slope of approximately 0. This was caused by magnesium contamination in the samples and is discussed further below. Above 0.5 ng, the slope of the log-log plots for the Mg(I) 285.21 nm line is equal to 0.62 and slopes of the log-log plots for the Mg(II) lines at 279.55 nm and 280.27 nm are 0.89 and 0.79 respectively. Since the curvature in the atomic emission line is greater than the curvature in the ionic emission calibration curves, there must be some degree of self-

absorption in this source at higher concentrations. Self-absorption of the magnesium 285.21 nm line is a likely explanation because this is a resonance line of an atomic species whose ground state populations at the typical excitation temperatures found in the FAPES source is likely much higher than that of the ground state ion. This self-absorption effect can be seen more clearly in Fig. 5.3 which shows the magnesium ion/atom emission intensity ratios as a function of magnesium load. This ratio should be independent of the magnesium load unless these magnesium loads change the plasma characteristics significantly. Hettipathirana [15] concluded that this was not the case by measuring the time resolved Pb(I) excitation temperature in the FAPES source and found it to be insensitive to the amount of lead present in the cuvette. The ion/atom ratios, Fig. 5.3, remain fairly constant up to a magnesium load of about 0.5 ng. Above this magnesium load the ratio increases. An increase in this ratio means that the emission from the atomic line is decreasing relative to the emission from the ion lines. This is consistent with self-absorption of the magnesium atomic resonance line which would decrease the emission from the atom line relative to the ion line as the magnesium load is increased.

The spectral linewidth of an emission line can be broadened by self-absorption. Absorption is strongest at the line center thus self-absorption will lower the measured intensity at the line center [94]. In the extreme case, this results in a dip at the line center. Lowering the intensity at the line center flattens the line profile thus broadening the measured linewidth. The spectral line profile of the Mg(I) 285.21 nm line was measured in a 20 Watt plasma using a 30 μm slit in the experimental system described earlier for different magnesium loads. These spectral line profiles for magnesium loads of 0.1 to 100 ng in a 20 Watt plasma are shown in Fig. 5.4. Line broadening can clearly be seen in this figure

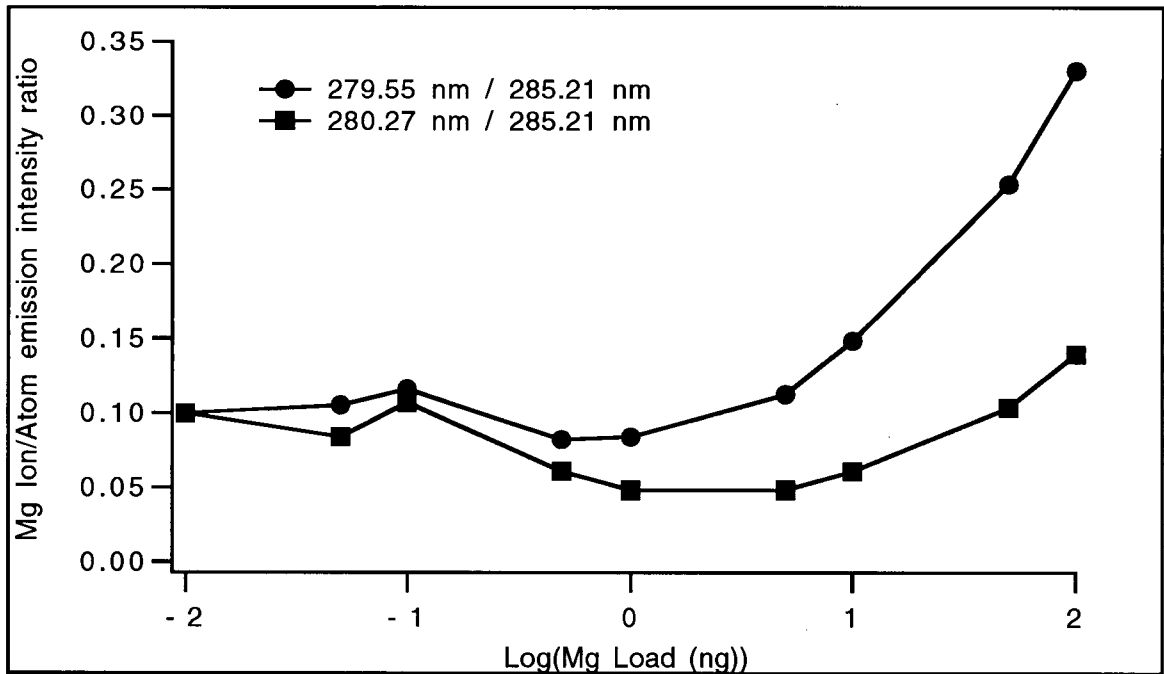


Fig. 5.3: Magnesium ion/atom emission intensity ratio as a function of magnesium load with 20 Watts r.f. power.

at higher magnesium loads where the full width at half maximum goes from the instrumentally limited 0.01 nm with low magnesium loads up to 0.04 nm with a 100 ng magnesium load. At 100 ng the self-absorption is sufficient to cause a dip in the line center characteristic of strong self-absorption. It can therefore be concluded that self-absorption occurs in the FAPES source at higher analyte concentrations. A similar effect was not observed for the Mg(II) lines. Increasing the magnesium load up to 100 ng had no effect on the spectral width of the Mg(II) line whose full width at half maximum remained at the instrumentally limited 0.01 nm. Other researchers have also seen self-absorption in the FAPES source as a curvature in atomic emission calibration curves whose onset determines the linear dynamic range of the source. Smith *et al.* [3] saw the onset of self-absorption for the Ag(I) 328.1 nm resonance line with silver loads as low as 1 pg.

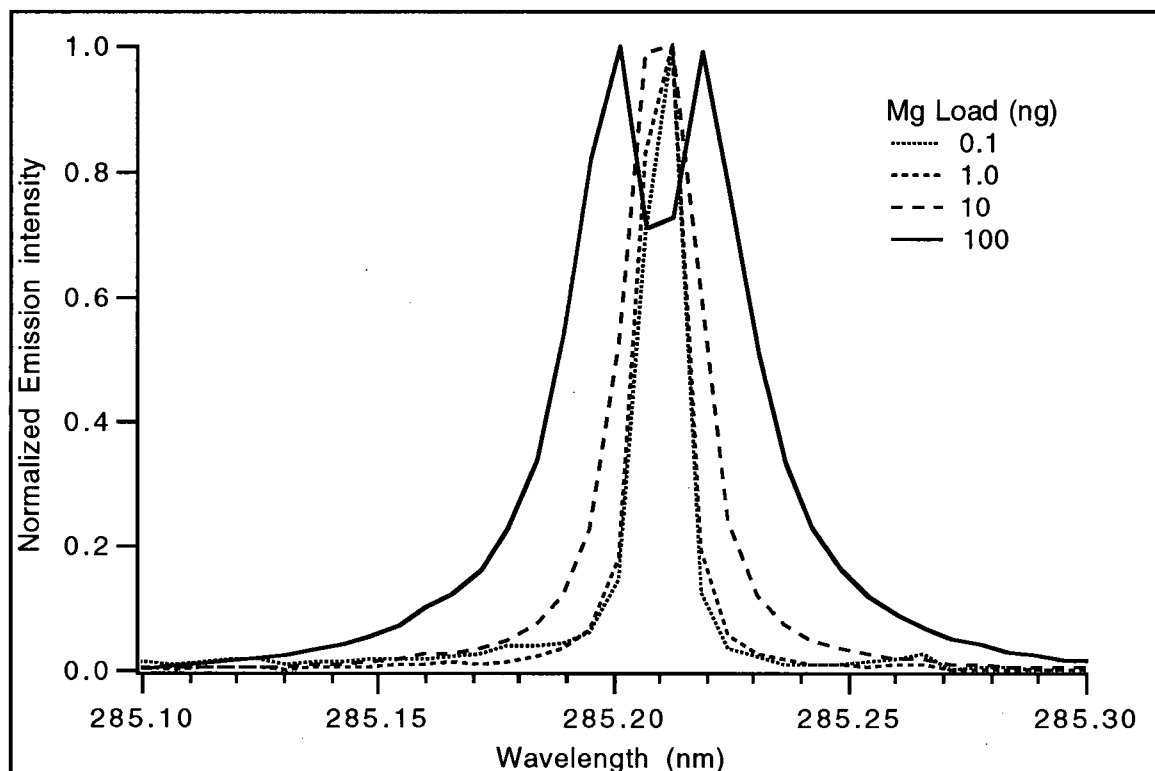


Fig. 5.4: Mg(I) 285.21 nm spectral line profile for several magnesium loads in a 20 Watts plasma.

The calibration plots, Figs. 5.1 and 5.2, show that there was some degree of magnesium contamination in the preparation of the samples. Since the focus of this study was not analytical figures of merit, the source of this contamination was not tracked down rigorously however it was likely present in either the deionized water or on one of the glassware surfaces used to prepare the samples. This contamination can be quantified by using standard addition calculations on the calibration plots. These show that the contamination was equivalent to a magnesium load of 0.33 ng, or 33 ppb since 10 μ L samples were used. A detection limit based on a signal-to-noise ratio equal to three times the

Technique	Mg Detection Limit (pg)	Reference
FAPES	170	this study
ETA-AES	135	[95]
GFAAS	1.5	[96]
ICP-OES	200	[96]
ICP-MS	100	[96]

Table 5.1: Magnesium detection limits for various techniques. Values were calculated as 3σ of the background intensity except for the GFAAS result which represents an absorbance value of 0.025.

standard deviation of a blank using the Mg(I) line equals 0.17 ng or 17 ppb similarly. Table 5.1 shows the detection limits for magnesium using several spectrochemical techniques. The detection limit found in this study is on the same order as those for the optical emission techniques listed however graphite furnace atomic absorption spectrometry has a detection limit two orders of magnitude smaller. It should be noted that the results from the present study are based on the measurement of only five samples per magnesium load value.

5.3.2 Effect of R.F. Power on Mg(I) and Mg(II) Emission Line Intensities.

In the following sections of this chapter, the effect of r.f. power on the emission intensities from the Mg(I) 285.21 nm and Mg(II) 279.55 nm lines are shown. A magnesium load of 0.5 ng was chosen for these studies because this

was the highest magnesium load where self-absorption was not yet apparent. For monitoring the ion emission, the 279.55 line was chosen because its intensity was greater than that of the 280.27 nm line thus increasing the signal-to-noise ratio in the results. This was especially important at low r.f. powers where the emission intensity of these ion lines was quite weak.

The temporally and spatially integrated emission from the Mg(I) 285.21 nm and the Mg(II) 279.55 nm lines is shown in Fig. 5.5 as a function of r.f. power. Emission from the Mg(I) line increases with an increase in r.f. power up to an r.f. power of 60 Watts. At higher r.f. powers the emission intensity from the atom decreases slightly. This behavior is similar to that of the indium atomic emission line discussed in Chapter 4 (see Fig. 4.1). The main difference is that the r.f. power at which the atomic emission intensity is a maximum is higher for magnesium than for lead. The intensity from the Mg(II) line, shown in Fig. 5.5, on the other hand, continues to increase as the r.f. power is increased. This suggests that increasing the r.f. power increases the degree of ionization of the analyte in the FAPES source.

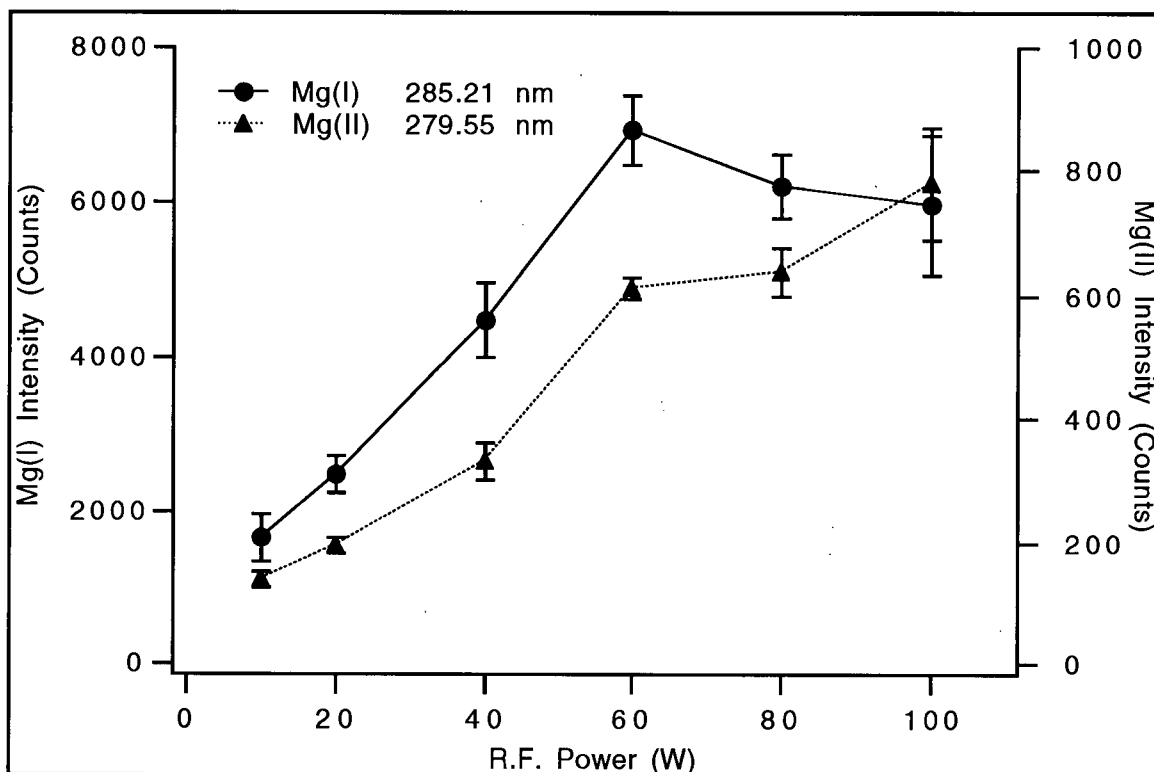


Fig. 5.5: Spatially and temporally integrated magnesium atom and ion emission intensities from 0.5 ng magnesium samples at different r.f. powers. Error bars represent ± 1 standard deviation (5 samples).

If ionization of analyte atoms is one of the main factors causing the emission intensity from atom lines to decrease at higher r.f. powers in this source, then it should be possible to see a trend with respect to the ionization potential of the atoms. Table 5.2 is a list of the ionization potentials and r.f. powers of analyte atoms where the maximum emission occurs. A trend is evident in this table; analytes with higher ionization potentials have emission intensity maxima at higher r.f. powers. At present the only other data available of this sort is from Sturgeon *et al.* [5]. They found that for r.f. powers between 50 and 75 Watts the emission intensity from Cd(I), Cu(I), and Fe(I) lines increased.

Element	Ionization Potential (eV)	R.F. Power (W)
In	5.7864	40
Pb	7.4167	50
Mg	7.6463	60

Table 5.2: R.F. power where the atomic emission intensity is a maximum in the FAPES and analyte ionization potentials.

* Pb data taken from [15].

The ionization potentials of these elements are 8.99 eV, 7.73 eV, and 7.90 eV respectively[81]. If these ionization potentials are compared to those in Table 5.2, it is likely that decreases in the emission intensities from these atoms due to ionization would only occur at r.f. powers higher than the 75 Watts used in that study. It can be concluded that ionization is a likely cause of the decrease in atomic emission in the FAPES source at higher r.f. powers and a closer investigation is warranted.

Spatially and temporally integrated emission intensity ratios of the Mg(II) 279.55 nm and Mg(I) 285.21 nm lines are shown as a function of r.f. power in Fig. 5.6. Within the precision of the results, the ion/atom emission line intensity ratio for these two lines remains essentially constant up to an r.f. power of 40 Watts. At higher powers, the ratio increases with increasing r.f. power. As discussed in the introduction to this chapter, ion/atom emission line intensity ratios give us an indication of the character of the plasma. In this case, the ion/atom magnesium emission intensity ratio on the order of 0.08 to 0.13 indicates that the plasma does not favor ionization at these r.f. powers.

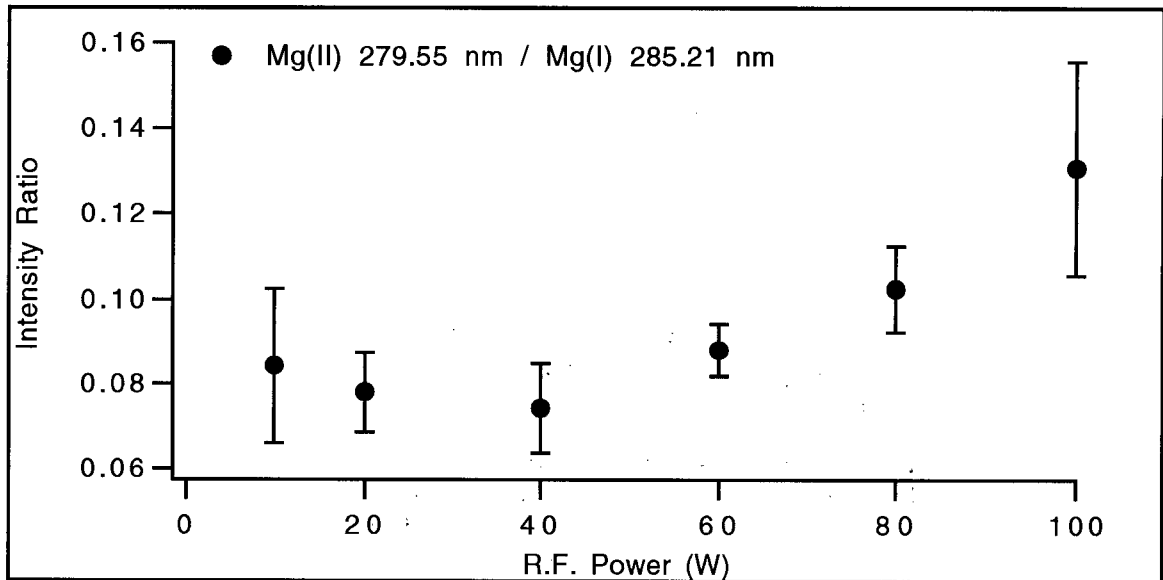


Fig. 5.6: Mg(II)/Mg(I) emission intensity ratio for 0.5 ng magnesium samples as a function of r.f. power. Error bars represent ± 1 standard deviation (5 samples).

This observation applies to the spatially and temporally integrated signals.

Spatially resolved ion/atom emission intensity profiles, shown below, show that there are spatial zones where ionization is more favored.

The degree of ionization of magnesium in the FAPES source can be calculated from these Mg(II) and Mg(I) line emission intensity ratios using equations 5.1 and 5.2. The values of the parameters used for this calculations are summarized in Table 5.3.

In order to calculate the degree of ionization of magnesium from ion/atom emission intensity ratios, it is necessary to know the ionization temperature. Pb(I) excitation temperatures were used for this purpose. These were interpolated from a least squares line fitted to the Pb(I) excitation temperatures

Species	Wavelength (nm)	g_o	g_k	$A (10^8 s^{-1})$	$E_k (cm^{-1})$
Mg(I)	285.213	1	3	4.95	35051
Mg(II)	279.553	2	4	2.68	35761

Table 5.3: Parameters used for calculating magnesium ion/atom population ratios from ion/atom emission intensity ratios [93].

calculated in Chapter 3. The assumption made is that the excitation temperature in the FAPES source is equal to the ionization temperature. While this assumption may not be valid, a close look at equation 5.2 shows that the degree of ionization has only a weak dependence on the temperature used to calculate it from the ion/atom emission intensity ratio in this case. In fact a 1000 K change in temperature (from 4000 K to 5000 K) only changes the calculated degree of ionization by about 5% of its value. Thus a calculated degree of magnesium ionization using the Pb(I) excitation temperature should yield sufficiently accurate results.

Fig. 5.7 is a plot of the spatially and temporally integrated degree of ionization of magnesium as a function of r.f. power in the FAPES source. At r.f. powers up to 40 Watts, the degree of ionization remains around 20%. Above 40 Watts, increasing the r.f. power increases the degree of ionization such that at 100 Watts the degree of ionization is about 30%. If the data are fitted to a second order polynomial, 100% ionization corresponds to an r.f. power of about 200 Watts. If the data for the four highest r.f. powers used are fitted to a straight line then 100% ionization corresponds to an r.f. power of about 500 Watts. While the precision and accuracy of these extrapolations make these values

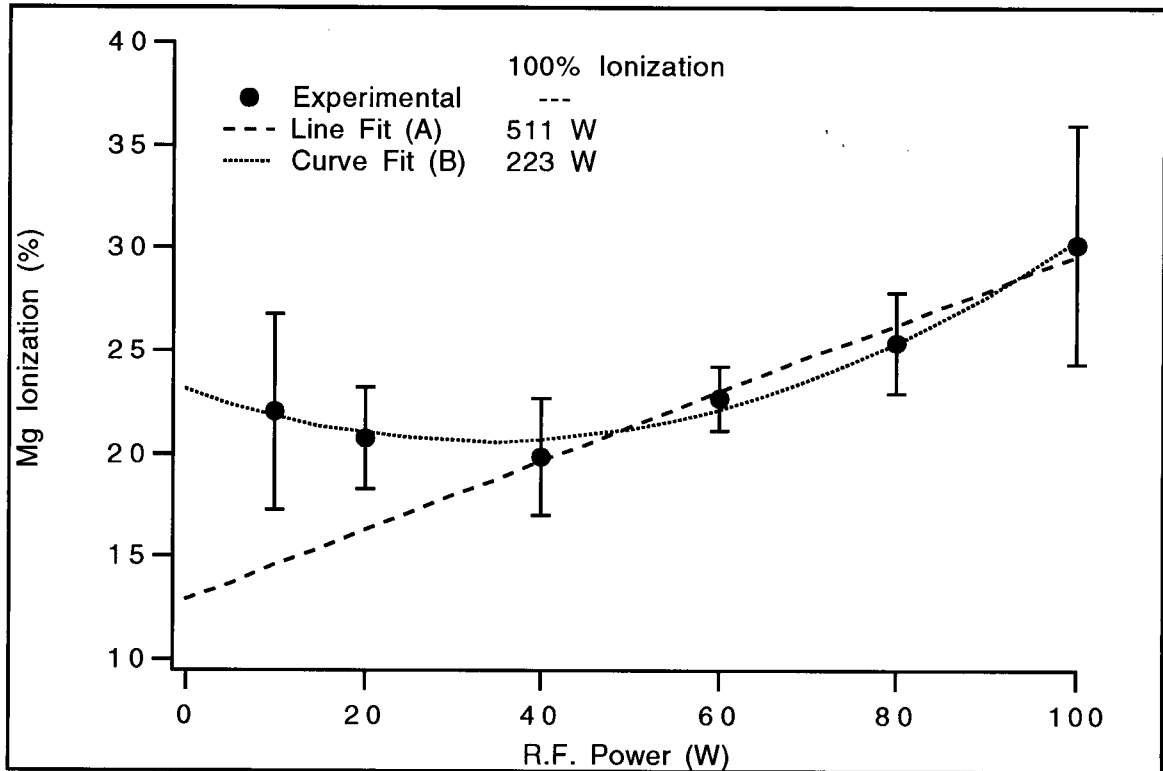


Fig. 5.7: Degree of magnesium ionization at different r.f. powers. Error bars represent ± 1 standard deviation (5 samples). Equations for the Curve Fit (A) to all data points and for the Line Fit (B) to the data points for the four highest r.f. powers shown are:
 (A) Ionization (%) = $12.8 + 0.168 \times \text{r.f.p. (W)}$
 (B) Ionization (%) = $23.0 - 0.149 \times \text{r.f.p. (W)} + 0.00223 \times (\text{r.f.p. (W)})^2$

quantitatively questionable, some qualitative information can be inferred from them. For example, if Mermet's [97] condition for a robust ICP is applied to the FAPES source, namely one where the degree of ionization of magnesium is above 95%, then this would require sustaining a plasma in the FAPES source with an r.f. power on the order of several hundred Watts. The FAPES source used in these studies has been operated at these higher r.f. powers however even at 200 Watts the center electrode was consumed fairly quickly thus making the use of such high r.f. powers impractical using the current methodologies.

Spatially resolved emission profiles of the Mg(I) 285.21 nm and Mg(II) 279.55 nm lines were measured as a function of r.f. power and are shown in Figs. 5.8A and B respectively. The spatial characteristics of the magnesium atom and ion emission is similar to that from the indium atom shown in Chapter 4. There are maxima adjacent to the center electrode and adjacent to the cuvette wall at each r.f. power used. There is also a maximum at a radius of about 1.25 mm at 10 Watts that moves further away from the center electrode and becomes relatively more intense at higher r.f. powers. In the emission profile of the Mg(II) line, the maximum adjacent to the center electrode relative to the intermediate volume is much higher than that of the Mg(I) line. In fact, at r.f. powers of 80 and 100 Watts, the decrease in spatially integrated emission intensity is mainly due to a reduction in the emission adjacent to the center electrode. This zone also has a significant increase in Mg(II) emission at higher r.f. powers thus it is reasonable to conclude that the decrease in Mg(I) emission at higher r.f. powers is primarily due to an increase in the ionization of the analyte atom.

Magnesium ion /atom emission intensity ratio profiles at several r.f. powers are shown in Fig. 5.9A. These show that the Mg(II) emission intensity increases relative to the Mg(I) emission intensity as the r.f. power is increased. This increase is most significant adjacent to the center electrode. In the intermediate region of the plasma, at a radius of about 1 mm to 2 mm the ratio increases from about 0.05 to 0.1 for an increase in r.f. power from 10 to 100 Watts. Adjacent to the center electrode the ratio goes up to about 0.25 at 100 Watts. These results suggest that there is an increase in the ionization of magnesium throughout the cuvette as the r.f. power is increased. The ionization of magnesium is also

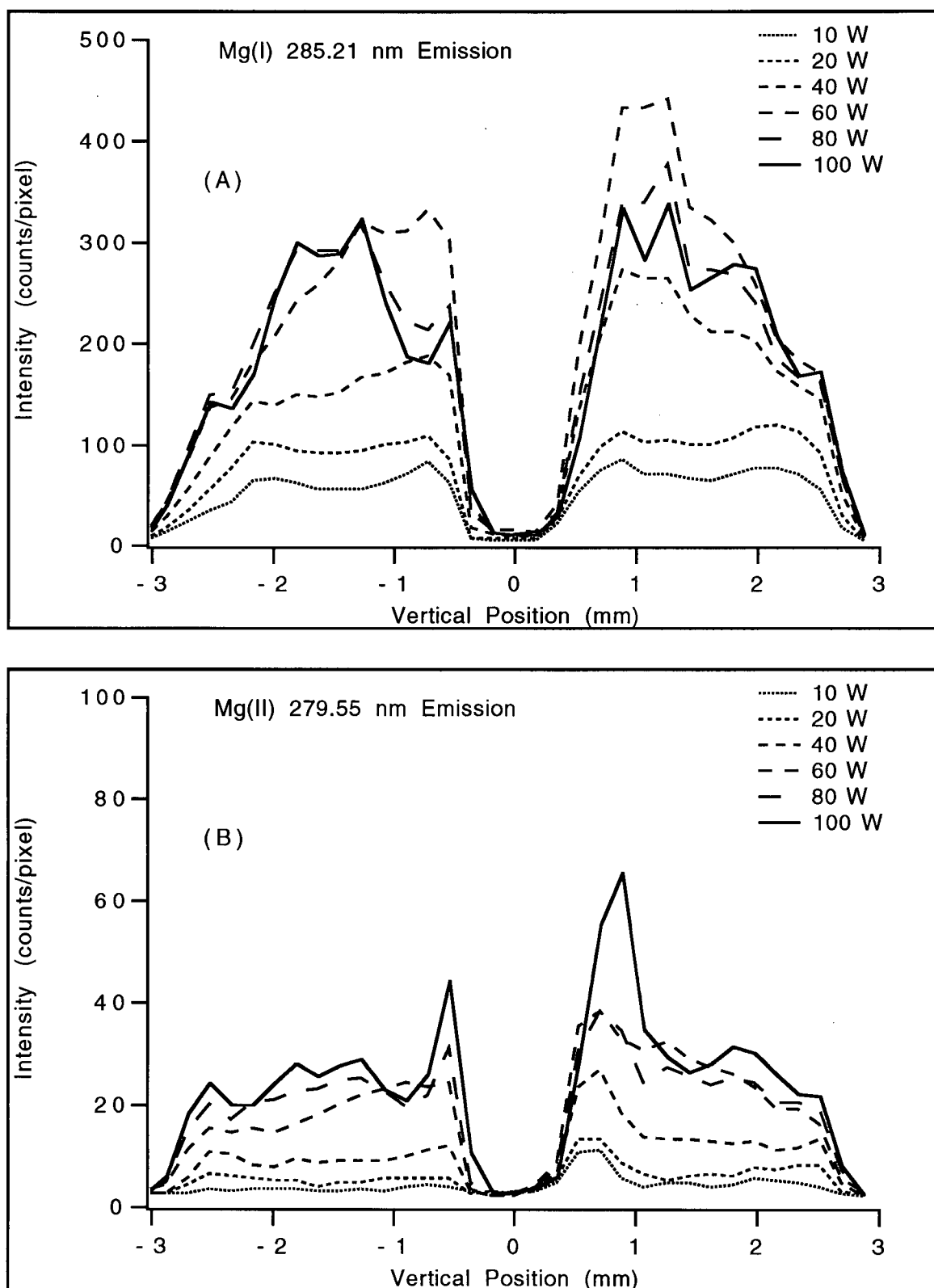


Fig. 5.8: Spatially resolved Mg(I) 285.21 nm (A) and Mg(II) 279.55 nm (B) emission profiles for 0.5 ng magnesium samples at several r.f. powers.

spatially dependent in that the highest degree of ionization occurs adjacent to the center electrode and adjacent to the cuvette wall.

Fig. 5.9B shows the spatially resolved degree of ionization of magnesium in the FAPES source calculated as described above for several r.f. powers. The maximum in ionization occurs adjacent to the center electrode. There is also a local maximum adjacent to the cuvette wall. A broad minimum is present at a radius of about 1.5 mm. The degree of ionization in this minimum varies from 12% to 25% for powers of 10 to 100 Watts respectively. The maximum in degree of ionization at 100 Watts reaches roughly 45% adjacent to the center electrode. These observations are consistent with the processes which occur in glow discharge sources [54, 56]. While the positive column contains some degree of ionization, the highest degree of ionization occurs in the negative glow region of the glow discharge.

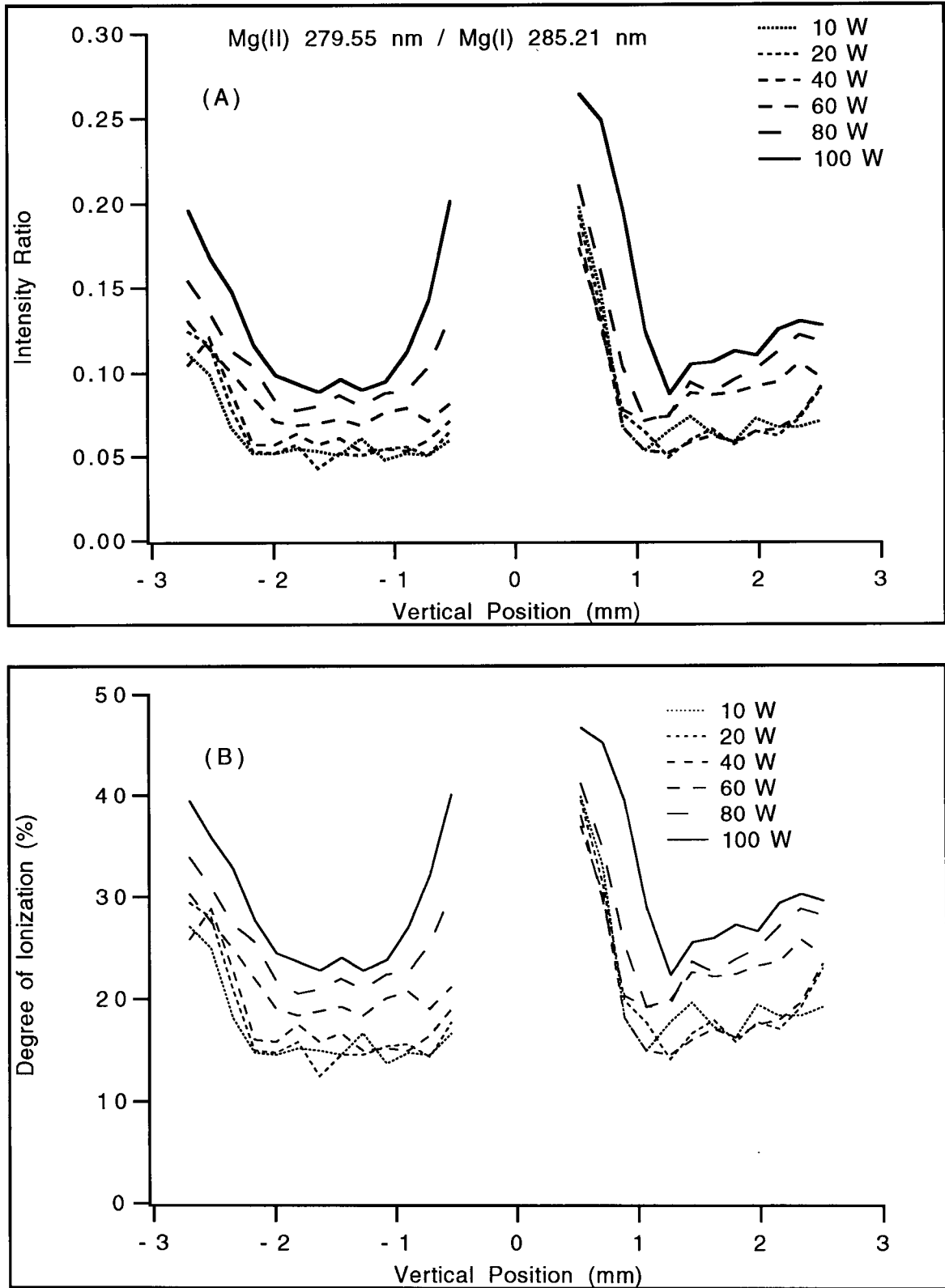


Fig. 5.9: Spatially resolved magnesium ion/atom emission intensity ratios (A) and degree of magnesium ionization (B) at several r.f. powers.

5.4 Summary and Conclusions

The results presented in this chapter show that there is a zone surrounding the center electrode and, to a lesser extent, one adjacent to the cuvette wall, where analyte atoms are ionized more strongly than in the rest of the plasma. This degree of ionization increases as the r.f. power is increased. If Mermet's [98] premise that a "robust" plasma free of matrix interferences is more likely in plasmas where the degree of ionization is higher (over 95% for ICP's) then the FAPES source should be more robust adjacent to the center electrode and this zone should be investigated as a possible location of the analytical zone in the FAPES source. Higher r.f. powers may also result in more robust plasmas but this will have to be weighed against the practicality of running the FAPES source at r.f. powers that may consume the center electrode rapidly. It may be possible to remedy this problem by using a different electrode material or by altering the methodology such that the plasma only remains on for a brief period during the atomization cycle. Higher r.f. powers also increase the degree of ionization and thus decrease the analyte atom populations, typically the analytical species used for spectrochemical quantitative analysis.

The spatial profile of the degree of ionization corroborates quite well with the analyte emission data in showing that the FAPES source operates as an atmospheric pressure r.f. glow discharge. The analyte emission maxima adjacent to the electrodes corresponds to the negative glow which has the highest degree of ionization in the discharge [56]. The intermediate region of the FAPES source, with a fairly low degree of ionization corresponds to the positive column.

There has been some recent interest in developing the FAPES source as an atomization and ionization source for analytical mass spectrometric analysis [99]. The results presented in this chapter suggest that this could be possible if certain experimental conditions were used. Namely, to maximize the ionization it would be necessary to operate the FAPES source with a fairly high r.f. power applied to the center electrode. Spatial selection of zones adjacent to the center electrode, where ionization is greatest, would provide the highest ion current to the mass spectrometer from the FAPES source.

CHAPTER 6

REDUCED PRESSURE STUDIES

“But the major features of the pattern of light and shade, so long as it subsists, are universal. It is like an organism, of which the different species are like fundamentals, while differing in details.”

K. K. Darrow [100]

6.1 Introduction

In the previous chapters it was shown that the FAPES source appears to operate as an atmospheric pressure r.f. glow discharge. In these studies it was proposed that the bright and dark concentric rings in the FAPES source correspond to the negative glow, the Faraday dark space and the positive column present in glow discharges. In the studies reported in this chapter, these concentric zones were investigated further by observing their behavior as the pressure inside the FAPES source was decreased. As was discussed in the introduction chapter, there are fairly good models that describe the geometry of the bright and dark zones in these discharges [56]. The behavior of these zones as the pressure is varied is also understood quite well and can be used to help in their proper identification in a source. Namely, as the pressure of a discharge is varied, the relative thickness of these zones changes. These changes are discussed below.

Reduced pressure studies in the FAPES source have only been reported in one previous publication by Imai *et al.* [21]. Their studies did not look at the spatial distribution of emission within the source but rather looked at the spatially integrated emission from analyte and background species. They found that the optimum pressure for analysis was 940 Torr reflecting a balance between collision frequency, analyte number density and excitation efficiency.

6.2 Experimental

6.2.1 Background

It is instructive at this point to reintroduce Fig. 1.5 found in section 1.4 of this thesis. It was briefly mentioned in that section that while this geometry occurs in most low pressure d.c. discharges, not all of the bright and dark zones, or spaces, are necessarily present in all configurations [101]. If the pressure of the gas in the discharge tube is raised from 1 Torr to about 100 Torr, the Aston, cathode and Faraday dark spaces and the cathode glow will shrink. The negative glow will move towards the cathode until it appears to come in contact with it. The positive column will also expand to partially fill in the Faraday dark space which will still be present, though much smaller. If the pressure in the discharge tube is instead reduced below 1 Torr, the cathode regions extend and the positive column shrinks until it eventually disappears entirely. If the electrode separation is increased, the geometry of the glow in the cathode region remains the same and the positive column expands to fill the space. If the electrode separation is decreased, the positive column shrinks and will eventually disappear altogether. Most analytical glow discharge devices operate in this mode with no positive column [53].

6.2.2 Instrumental Parameters

The Cube source, described in section 2.1.1.2, was used for the reduced pressure studies and was evacuated using a vacuum pump (W. M. Welch Mfg. Co., Chicago, IL, U.S.A.) connected to the plasma gas outlet with a four-way connector. The work-head's internal pressure was monitored using a mechanical pressure gauge (GAST Mfg. Co., Benton Harbor, MI, U.S.A.) coupled to this connector. The remaining outlet on the four-way connector was equipped with a needle valve. This was used as a helium exit port when the FAPES source was operated at atmospheric pressure with the vacuum pump turned off.

The imaging lens system used to image the source onto the entrance slit of the monochromator and the pixel binning were the same as that described in section 4.2.2. A 1 s CCD integration time was used for the He(I) and N_2^+ emission measurements. The 3600 lines/mm grating was installed in the monochromator whose entrance slit width was set to 30 μm providing sufficient resolution to resolve the lines of interest.

6.2.3 Procedure

The emission intensity profiles for the He(I) 388.86 nm line in the FAPES source discussed in this chapter were measured at various reduced helium pressures using the instrumental parameters discussed above. Specific reduced pressures were obtained by having the vacuum pump on and adjusting the helium gas supplied to the work-head using the needle valve on the graphite furnace power supply. A graphite furnace temperature program was not initiated

for the measurement of these He(I) emission profiles. Instead, the r.f. power was applied to the center electrode once the helium pressure had been stabilized to the desired value. After approximately 5 s, the data acquisition was triggered manually through the function generator.

6.3 Results and Discussion

Spatially resolved profiles for the emission from He(I) in a FAPES source operated with 20 Watts r.f. power are shown in Fig. 6.1 for several pressures. The vertical emission profile of this He(I) 388.86 nm line in the FAPES source at atmospheric pressure has been discussed in detail in Chapter 3 and consists of an intense emission maximum adjacent to the center electrode and another weaker emission maximum adjacent to the cuvette wall. There is also some relatively weaker He(I) emission throughout the volume of the cuvette. Since the emission maximum adjacent to the center electrode is concentric with the center electrode, its vertical profile, as shown in Fig. 6.1, would be expected to be symmetric given the coaxial geometry of the source. This is clearly not the case; the emission above the center electrode is greater than that below the center electrode. This asymmetry was either caused by an experimental artifact arising from a slight off-axis viewing of the source or it is representative of the spatial structure of the plasma.

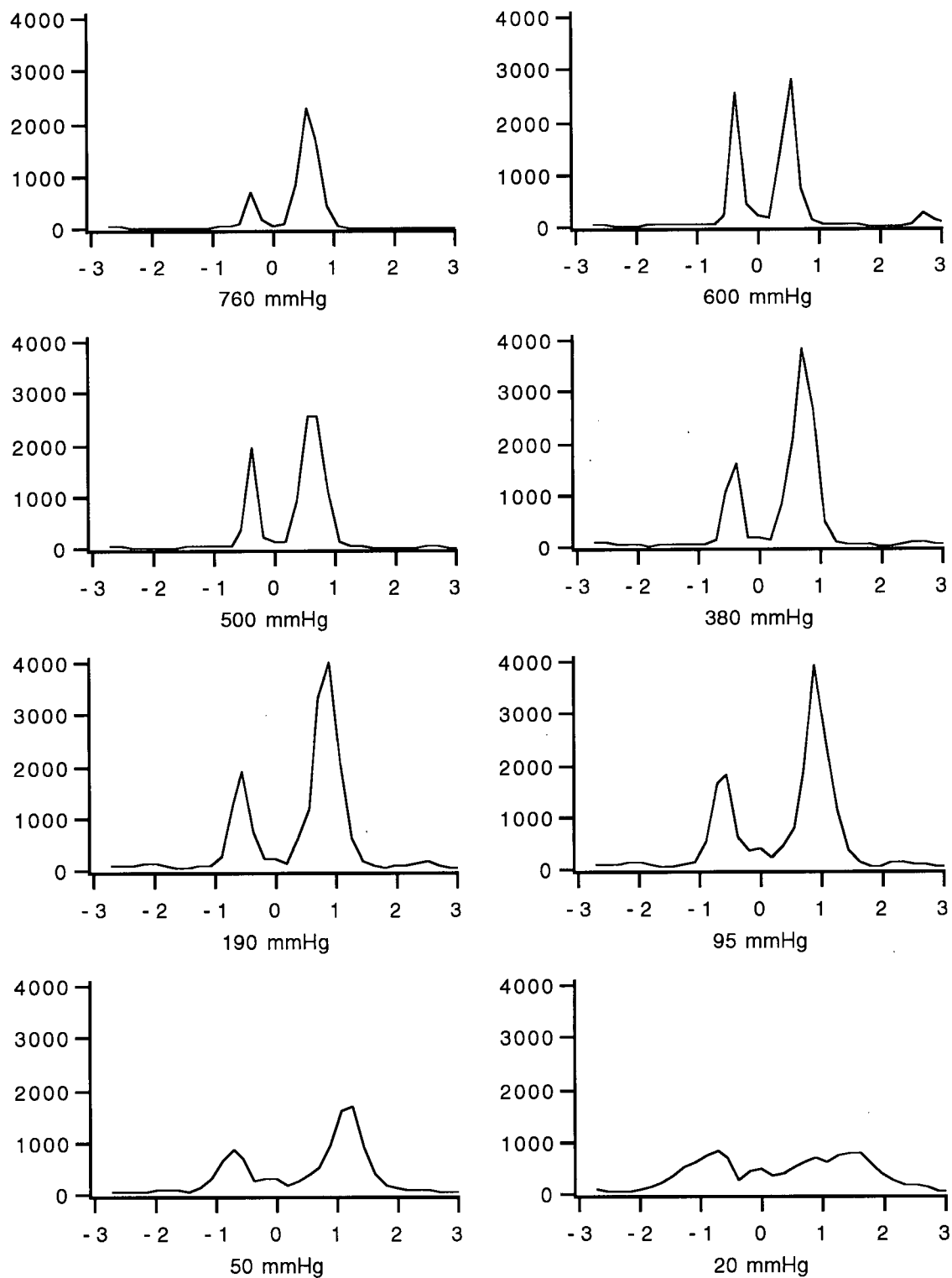


Fig. 6.1: Spatially resolved He(I) 388.86 nm emission in a 20 Watt plasma at several pressures. Intensities are in counts/pixel *versus* vertical position in mm.

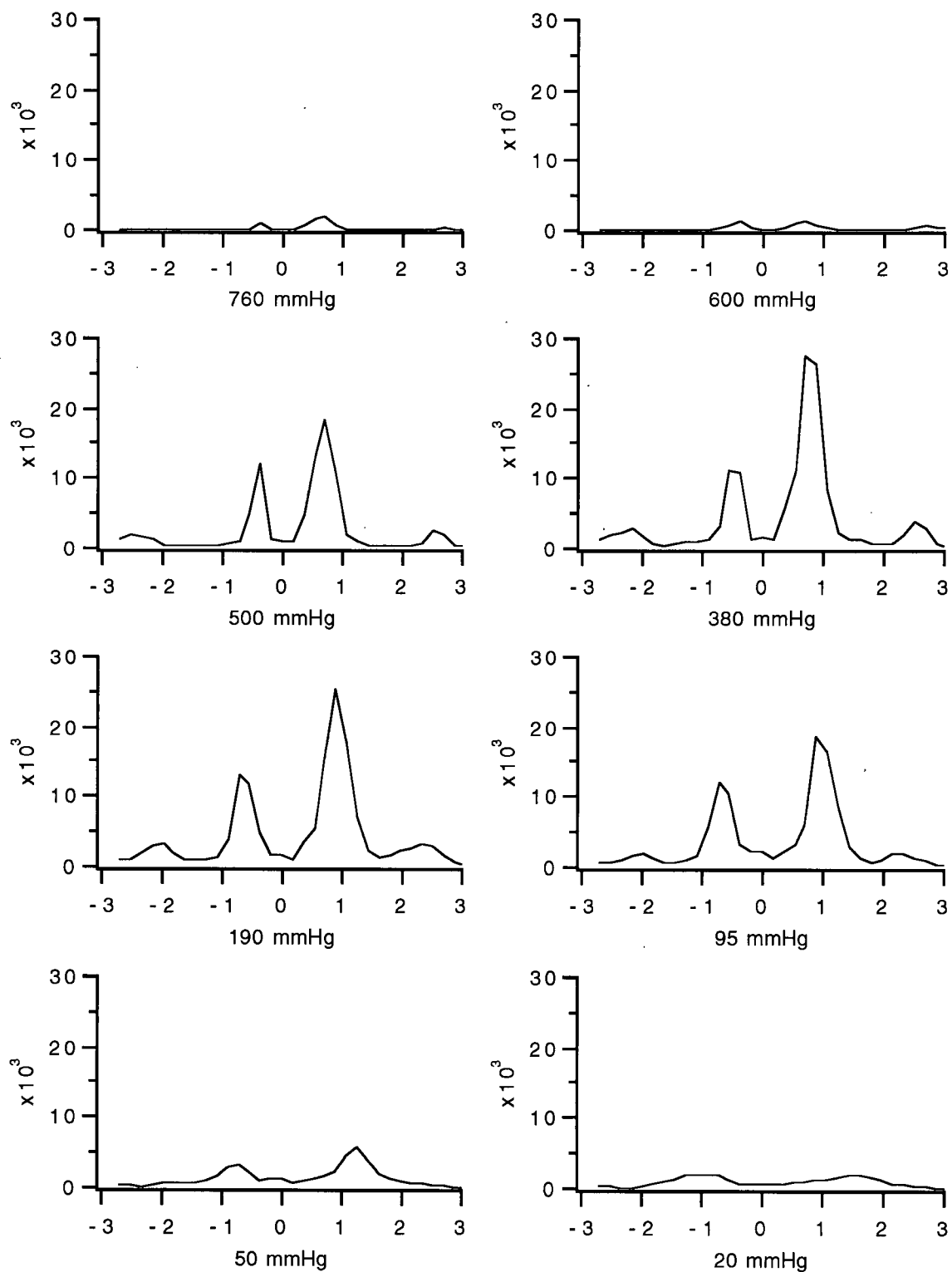


Fig. 6.2: Spatially resolved N_2^+ emission in a 20 Watt plasma at several pressures. Intensities are in counts/pixel versus vertical position in mm.

If the asymmetry was caused by viewing the source off-axis, a vertical emission profile as seen in Fig. 6.1 would only result if the source was viewed from above the center electrode axis. This would cause the emission from below the center electrode to be blocked off by the electrode resulting in the observed profile. In order to check for this possibility, the imaging lenses were moved such that the emission was observed purposefully off-axis from below the axis of the center electrode in gradual steps. The resulting emission profiles did not resemble those in Fig. 6.1 with the emission maximum below the center electrode being more intense than the emission maximum above the center electrode as would be expected if the asymmetry was caused by off-axis viewing. Viewing the emission off-axis, as described above, instead resulted in a similar asymmetry except that the emission minimum at the center, representing viewing the center electrode, was narrowed as the angle of viewing was increased until finally the maxima spatially overlapped each other. Thus the asymmetry measured in the He(I) emission profile must be representative of the structure of the plasma. There are several possible causes for the plasma being slightly asymmetric given the coaxial geometry of the source. One is the positioning of the center electrode, a second is the effect of the dosing hole, and a third is the possibility that the plasma emission maxima do not cover the entire surface of the electrodes.

It is possible that the center electrode was positioned slightly closer to the top of the cuvette wall causing the emission to be more intense above the electrode than below. This is because the electric field strength, and thus the plasma energy, between the electrodes is higher for electrodes that are closer together given an equal potential difference between the two [54]. To ensure that this was not the case, the center electrode was moved closer to the bottom of the

cuvette. The asymmetry in the source did shift such that the emission was more intense below the center electrode than above. The amount that the center electrode needed to be moved for this effect to account for the measured asymmetry in the He(I) emission intensity profile was much greater than the precision with which it was possible to position the center electrode. Thus the center electrode position was not a likely cause of the measured asymmetry.

The dosing hole may also affect the geometry of the plasma. Since the graphite cuvette acts as an electrode in this source, its geometry will affect the geometry of the electric field creating the plasma. While this was not studied systematically, a positive correlation between the degree of asymmetry in the plasma and the age of the graphite cuvette was observed. After continuous use, the dosing holes of the graphite cuvettes eventually became eroded and developed jagged edges. These sharper edges may increase the electric field nearby [54] thus causing the plasma to have a slightly higher energy between the center electrode and these edges. A skewing of the cylindrically shaped plasma would result and the He(I) emission would be asymmetric about the center electrode as observed.

A third possible cause of the plasma asymmetry about the center electrode is that the plasma emission maxima adjacent to the center electrode may not cover the entire surface of the electrode. In this case the plasma would be operating as a normal glow in glow discharge terminology. In a normal glow the surface of the electrode is not entirely covered by the plasma and an increase in power increases the size of the region of the electrode carrying current thus increasing the current while maintaining a constant potential [56]. If the plasma did not cover the entire surface of the center electrode, asymmetry in the emission profile could result. Under such an operating condition, increasing the

r.f. power to the center electrode should lessen, and ultimately remove, this asymmetry. Such an experiment was done and discussed in Chapter 3. Fig. 3.4 shows the results of this study. In this figure there is a similar asymmetry to that in Fig. 6.1, though the effect is not as pronounced (the graphite cuvette used here was new). The asymmetry in the He(I) emission remains fairly constant for r.f. powers as high as 200 Watts thus it is likely that the asymmetry in the emission is not caused by the plasma operating as a normal glow at the center electrode. It is possible to argue that the plasma must therefore be operating as an abnormal glow at the center electrode with the entire electrode surface carrying current. While this may indeed be the case, proof of such a situation would require monitoring the voltage and current between the center electrode and cuvette as the r.f. power is increased. Such a measurement would be complicated by the fact that there may also be a normal or abnormal glow on the cuvette wall depending on the magnitude of the r.f. power.

As the pressure in the FAPES work-head was decreased from atmospheric, there was a change in the geometry and intensity of the He(I) emission profile. This change in the emission intensity as a function of pressure is seen more clearly in Fig. 6.3 which shows the spatially integrated He(I) emission intensity as a function of pressure. As the pressure is decreased from 760 mmHg, the spatially integrated emission intensity increases until the pressure reaches approximately 100 mmHg. At this pressure, the He(I) line emission intensity is roughly three times what it is at atmospheric pressure. As the pressure is decreased from 100 mmHg to 40 mmHg, there is a decrease in the He(I) emission intensity. A further decrease in pressure results in an increase in emission intensity.

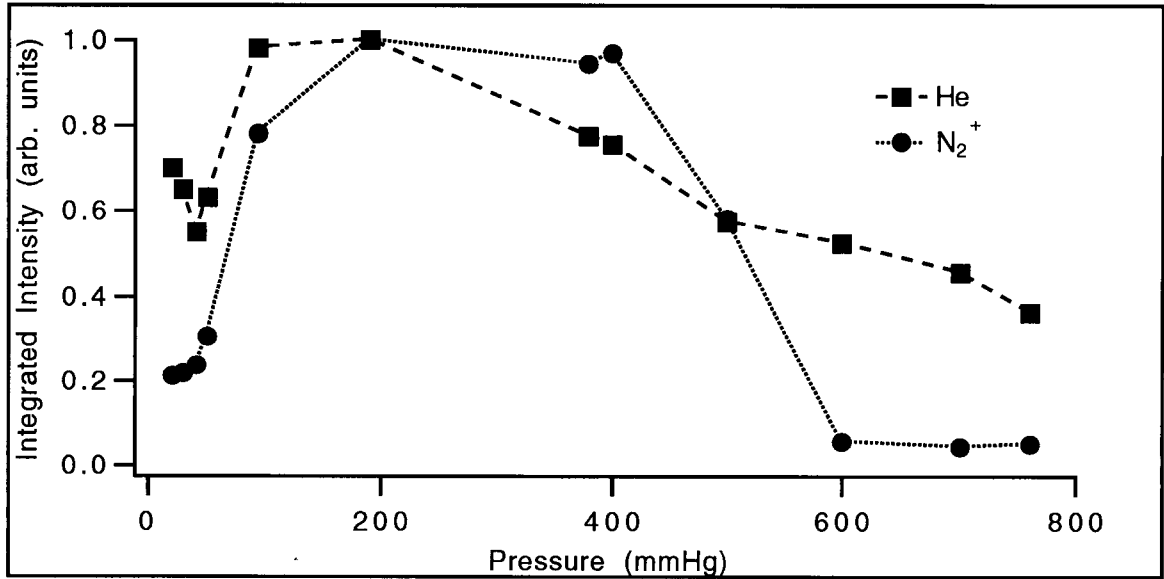


Fig. 6.3: Integrated emission intensities for He(I) and N₂⁺ emission lines in a 20 Watt plasma as a function of pressure.

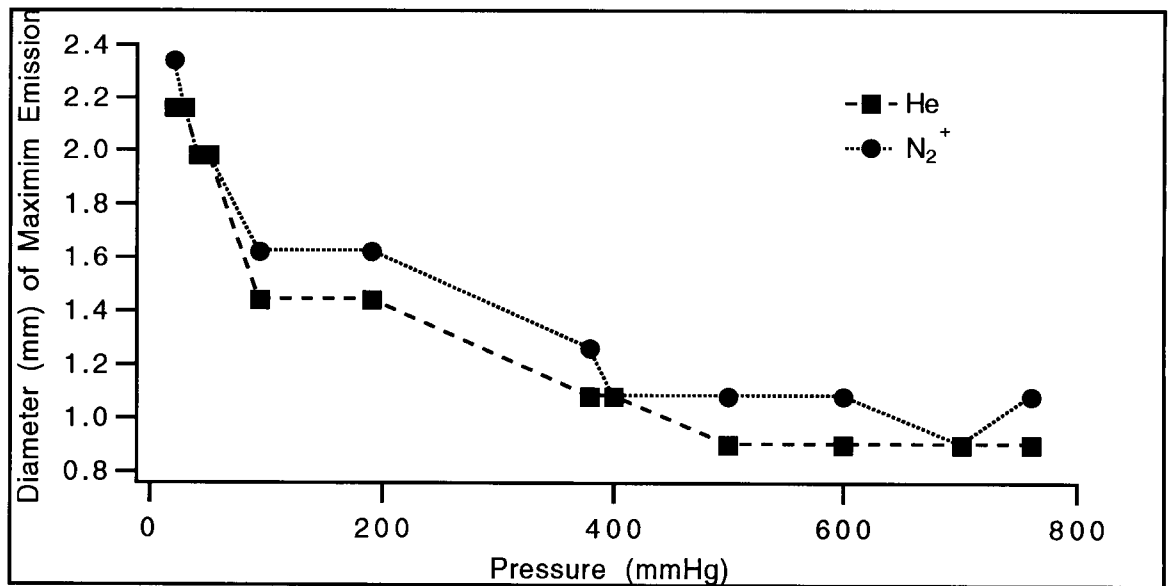


Fig. 6.4: Diameter of the emission intensity maximum for the He(I) and N₂⁺ lines in a 20 Watt plasma as a function of pressure.

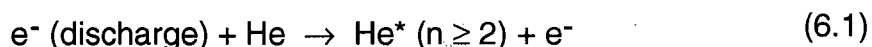
Decreasing the pressure also caused the He(I) emission intensity maxima to move away from the electrodes, here the center electrode and the cuvette wall. The separation of the two emission maxima adjacent to the center electrode is a measure of the diameter of the maximum emission intensity zone surrounding this electrode. A plot of this diameter as a function of pressure, Fig. 6.4, clearly shows that as the pressure is decreased this diameter increases. The result is due to the formation of a dark space adjacent to the center electrode. The thickness of this dark space is correlated to the diameter of the emission maximum and therefore increases as the pressure is decreased.

The spatially resolved emission profile for the N_2^+ lines described earlier is shown for series of pressures in Fig. 6.2 at 20 Watts r.f. power. The spatial profile of the N_2^+ emission at atmospheric pressure has also been discussed in detail in Chapter 3 for various r.f. powers. At 20 Watts, the emission has two maxima: one maximum adjacent to the center electrode and one less intense maximum adjacent to the cuvette wall. As with the He(I) emission intensity, the emission intensity profile of the N_2^+ emission is dependent on the pressure within the source. The spatially integrated emission intensity changes quite significantly as the pressure of the source is varied. Fig. 6.3 shows this quantitatively. As the pressure is decreased from atmospheric to 600 mmHg, the N_2^+ emission intensity remains fairly constant. A further decrease in pressure to 400 mmHg causes a sharp increase in the emission intensity which remains relatively constant down to approximately 200 mmHg. In this pressure range the emission intensity is approximately 20 times that at atmospheric pressure. Lowering the pressure below 200 mmHg caused the emission intensity to decrease asymptotically with the intensity approaching a constant value approximately 4 times the intensity at atmospheric pressure.

The geometry of the N_2^+ emission intensity was also dependent on pressure. A decrease in pressure from atmospheric created a dark space between the electrodes and the emission maxima. Fig. 6.4 shows this effect quite clearly for the emission maxima adjacent to the center electrode. It is a measure of the diameter of that emission maxima. A decrease in pressure increased the diameter of this maximum similarly to the diameter of the He(I) emission maximum thus increasing the thickness of the dark space.

During the course of these measurements visual observations of the source were made which agreed with the measured emission intensities. Besides observing a radial expansion of the inner emission maximum and a radial contraction of the outer emission maximum, the plasma was also seen to expand outside the cuvette at reduced pressures. As the pressure was decreased from atmospheric, the plasma began expanding outside the cuvette volume. At 400 mmHg the plasma formed a thin layer on the outside surface of the cuvette which extended approximately 2 mm along the cuvette wings. Reducing the pressure to 100 mmHg caused the emission maxima adjacent to the cuvette wall and center electrode to move towards each other. When the pressure reached 50 mmHg, the two maxima had essentially become one diffuse glow slightly closer to the center electrode than to the cuvette wall. At this pressure, the diffuse glow outside the cuvette had essentially grown beyond the entire graphite cuvette holding electrodes and along the r.f. electrode holder filling the entire volume of the Cube source with a low intensity glow.

The He(I) and N_2^+ emission intensity versus pressure curves, Fig. 6.3, can be explained in terms of collision frequency within the FAPES source. In helium plasmas, He^* (excited state helium) is created mainly by collisions with electrons [102].



N_2^+ is created *via* a charge transfer reaction (equation 3.1) with He_2^+ which itself can be created by several different collisional processes involving electrons, ground state and excited state He, excited state He_2^+ , and ground state He^+ [102]. The kinetic energy of charged particles in an electric field increase with increasing E/p values where E is the electric field and the p is the pressure [103] thus as the pressure is decreased from atmospheric, the kinetic energy of the charged particles in the FAPES source increases. This tends to increase the collisional products in the source, including excited state He and N_2^+ , as the pressure is decreased. Conversely, the collision frequency of particles in a certain volume decreases with decreasing pressure. These two competing effects can account for most of the effects of pressure on the intensity of the He(I) and N_2^+ emission in the FAPES source. As the pressure is decreased from atmospheric pressure down to roughly 100 mmHg, the increased electron energy causes an increase in the populations and thus emission from these species. As the pressure is decreased further the collision frequency is reduced sufficiently to counter this effect and the emission intensity decreases.

The seemingly anomalous increase in He(I) emission when the pressure was decreased below 40 mmHg was likely caused by a mode change in the plasma at these pressures. As was described above, at pressures below 50 mmHg the plasma inside the Cube source was no longer confined within the graphite cuvette but permeated the entire volume of the Cube work-head. As the pressure was reduced below 50 mmHg, the emission intensity throughout the Cube increased. Due to the geometry used in measuring the emission from the source, the volume actually viewed by the detection system necessarily included everything in the line of sight of the detection system. While the transfer

efficiency of the emission is greatest at the cuvette center [76], emission from outside the cuvette is also transferred to the detector. The increase in the measured emission intensity of the He(I) line below 50 mmHg likely resulted from this light transfer.

If the FAPES source is considered as a r.f. glow discharge then the dark space that develops between the electrodes (the cuvette and the center electrode) and the emission maxima can be readily explained as the cathode-fall thickness [104]. This zone is commonly referred to as the cathode or Crookes dark space by English authors and as the Hittorf dark space by German authors [105]. The thickness of this dark space corresponds to the distance which the electrons must travel before they have enough energy to produce excitation and ionization. It is approximately five times the thickness of the electron mean free path [105] and depends on electron collision phenomena thus its thickness increases as the pressure decreases [104]. This is consistent with the observations summarized in Fig. 6.4. These show that as the pressure of the FAPES source was decreased, the emission maxima moved away from the electrodes resulting in the creation of a dark space between these maxima and the electrodes which expanded as the pressure was decreased.

6.4 Summary and Conclusions

In this chapter the results of reduced pressure studies in the FAPES source have been shown. Variations in pressure inside the source changed the intensity of the optical emission as well as the geometry of plasma within the FAPES source.

A reduction in pressure from atmospheric to approximately 200 mmHg was seen to increase the emission intensity of the He(I) and N_2^+ lines. A further decrease below 200 mmHg caused the optical emission from these background species to decrease. These observations were explained in terms of the kinetic energy of the charged particles in the FAPES source. As the pressure was decreased the kinetic energy of the charged particles increased. These in turn were more effective at creating excited state species from which emission was measured. Further decreases in pressure simply reduced the population density of the emitting, and in fact all, species thus the emission intensity was attenuated.

A reduction in pressure caused the geometry of the plasma in the FAPES source to change similarly to other glow discharge geometries. As the pressure was decreased a dark space appeared adjacent to the electrodes, in this case the center electrode and cuvette wall. The thickness of this dark space was shown to be inversely correlated with pressure which is characteristic of the cathode dark space in glow discharges.

CHAPTER 7

ADDITIONAL OBSERVATIONS

“No data are worthless.”

Gary Horlick

7.1 Introduction

This chapter shows the results from observations and studies aimed at gaining some additional information on the characteristics of the FAPES source that were conducted throughout the course of the research presented in this thesis. While some of the studies reported were not totally successful, they did yield useful information which should not be overlooked.

7.2 Visual Observations in the FAPES Source

Initial visual observation of the FAPES source indicated that the source was not spatially homogenous and the data shown in the previous chapters has helped in explaining this spatial structure. In this section, the initial visual observation which led to spatially resolved emission studies are presented.

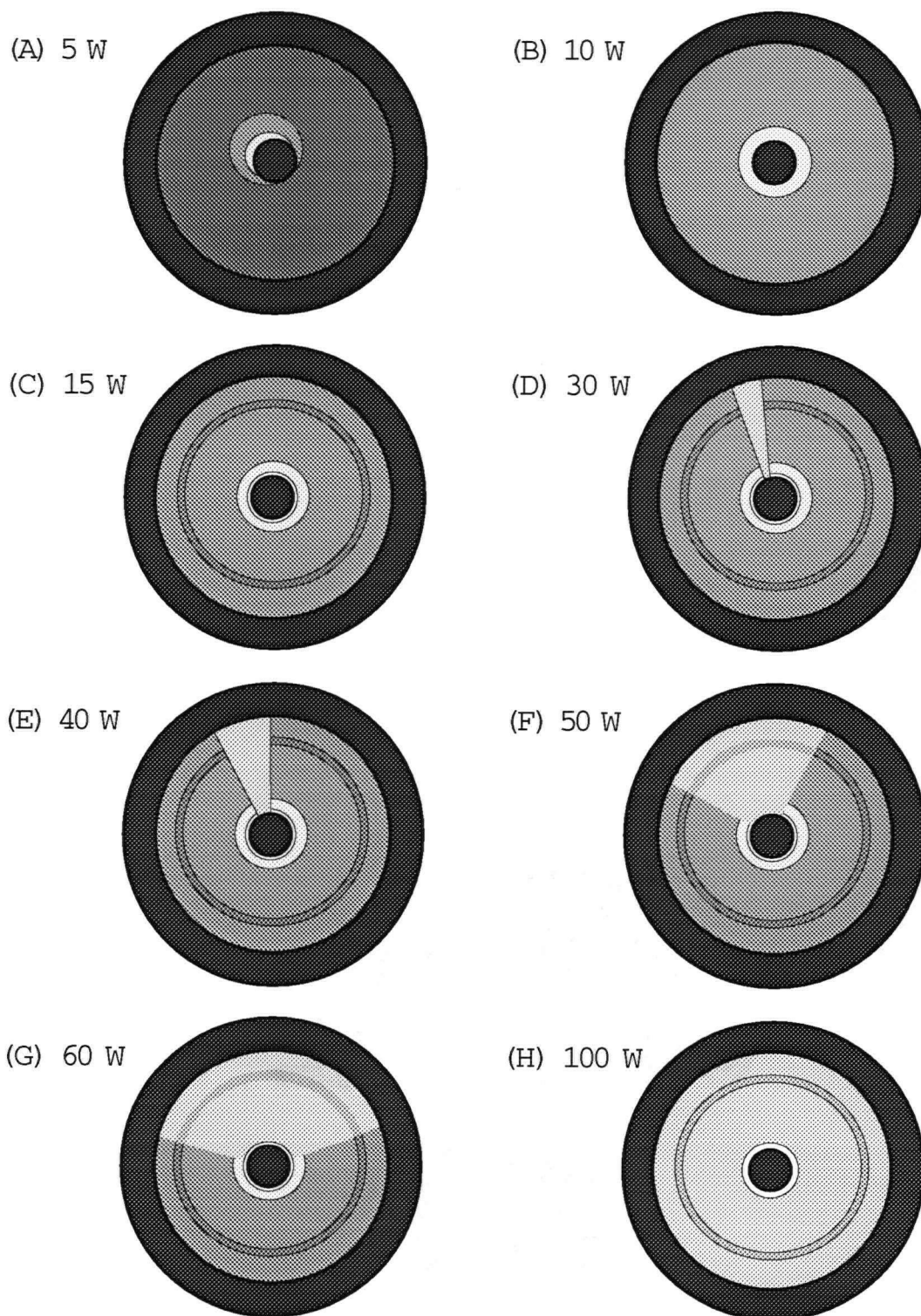


Fig. 7.1: Visual end view appearance of the helium FAPES source at different r.f. powers. The graphite cuvette and center electrode are represented by the darkest shade of gray. Lighter shades of gray represent brighter zones in the source.

The appearance of the helium plasma in the FAPES source viewed end-on is represented in Fig. 7.1. Visual observations at atmospheric pressure as the r.f. power was increased suggested that at least three type of electric discharges are possible within the FAPES source. The process of changing from one type of discharge to another was not gradual but rather a discrete transition.

The first discharge type occurred at low r.f. powers, typically between 5 and 10 Watts. At the lower end of this range, around 5 or 6 Watts, the plasma appeared as a faint glow near one side of the central electrode as shown in Fig. 7.1A. This glow was on the side of the central electrode that was closer to the cuvette wall. Note here that the center electrode was positioned as close to coaxially as possible but an exact positioning was not possible. The discharge became virtually cylindrically symmetric as the r.f. power was increased beyond 7 Watts. This first discharge type had two zones that were coaxial with the central electrode. Visually, a higher intensity emission zone was seen within half a millimetre of the central electrode. A less intense discharge extended approximately one to two millimetres further. Increasing the forward r.f. power at this point simply expanded the diameter of the outer zone without affecting the inner one. When the forward r.f. power reached 10 Watts, this outer zone appeared to fill the cuvette (Fig. 7.1B). A further increase beyond 10 Watts caused a transition to the second type of discharge.

The second type of discharge, represented by Fig. 7.1C, had the same visual features as the first type but with additional structure. Together with the low intensity emission observed throughout the cuvette and the one half millimetre thick higher intensity zone, a third discharge zone appeared which had a significantly higher intensity than either of these. This discharge appeared to be a sheath that resided on the surface of the central electrode. This zone may

correspond to a cathode glow though further investigations are needed to confirm this. Within the low intensity discharge that filled the rest of the cuvette, there appeared to be a lower intensity ring about one half millimetre off, and concentric to, the cuvette. Increasing the r.f. power within this discharge's power range increased the intensity of all the zones but did not change their geometry. The transition to the next type of discharge occurred around 32 Watts r.f. power.

This transition to the third type of discharge was the formation of a diffuse arc or filament between the central electrode and the cuvette. As with the previous transition, this transition did not change the structure of the discharge but rather added to it. The diffuse arc formed where the central electrode was slightly closer to the cuvette wall as shown in Fig. 7.1D. This diffuse arc expanded as the r.f. power was increased until it filled the cuvette at a forward power of about 100 Watts. This process is shown in Figs. 7.1E to H. The innermost zone remained and became more intense as the r.f. power was increased. The second innermost zone which extended half a millimetre off the central electrode was not present in the diffuse arc but did remain in the regions where the diffuse arc was not present. Increasing the forward r.f. power beyond 100 Watts simply increased the intensity of the emission within the cuvette.

While these observations correlate well with the spectroscopic measurements reported in the earlier chapters, a closer investigation of the current-voltage nature of the transitions should yield valuable information and give a clearer picture of the discharge's operation. In light of the results presented in this thesis, it seems likely that the initial low power asymmetric plasma, Fig. 7.1A, is operating in the normal glow mode. Increasing the r.f. power possibly changes the discharge to an abnormal glow mode adjacent to the

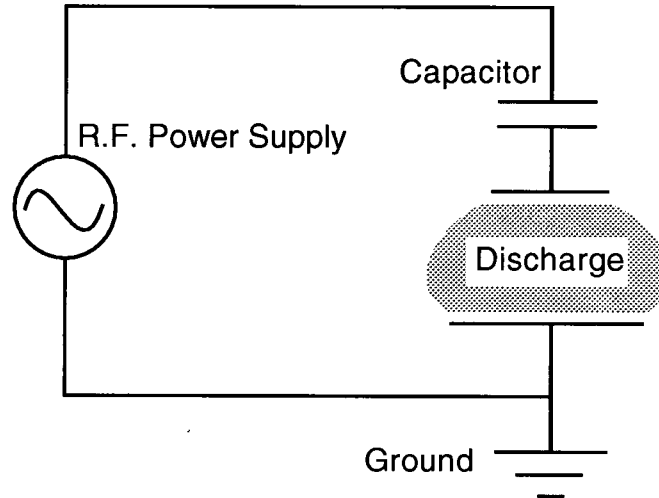


Fig. 7.2: Schematic of a high frequency glow discharge circuit. Adapted from Chapman [56].

center electrode and further increases in the r.f. power result in the formation of a diffuse arc. A parametric survey of the effect of different operating parameters on the onset of these transitions would be useful in verifying their identity.

7.3 Center Electrode Self-Bias

During the course of the studies reported in this thesis the d.c. self-bias on the center electrode was monitored periodically since the r.f. power supply used continually measured this value. The trend in these measurements has been generalized and plotted in Fig. 7.3. Before discussing these results, the cause of the r.f. electrode self-bias should be considered. In r.f. discharges where the electrodes are conducting, a blocking capacitor is typically used. A schematic of the circuit can be represented as shown in Fig. 7.2. Once the discharge has

been initiated, if the electrodes are of different surface areas and the frequency is sufficiently high (>1 MHz), the smaller electrode will develop a negative potential bias relative to the larger electrode[56]. In a given electric field, lighter charge carriers will carry more current than heavier charge carriers due to their higher mobilities. In helium discharges, such as the FAPES source, the lighter charged particles are mainly electrons and the heavier charged particles are mainly He^+ . When an electrode has a negative potential it is bombarded by positive ions and the capacitor begins to charge positively. When this electrode has a positive potential it is bombarded with a higher current of electrons thus the capacitor gains a net negative charge resulting in a negative d.c. bias. The relative intensity of this effect on the two electrodes is related to the area of each electrode in contact with the discharge. The smaller electrode, having a higher electric field, obtains a more negative bias than the larger electrode.

The d.c. bias on the center, and smaller, electrode in the FAPES source was indeed negative as expected. The magnitude of the d.c. bias varied with operating conditions including the r.f. power as shown in Fig. 7.3. As the r.f. power was increased from 0 W, the magnitude of the d.c. bias increased fairly sharply with respect to r.f. power up to about -30 V at roughly 10 W. At this point there was a transition to the second type of discharge, as described in section 7.2, and a concurrent drop in the magnitude of the d.c. bias back to 0 V. In the regime of the second type of discharge, the magnitude of the d.c. bias increased again as the r.f. power was increased. This continued until there was the formation of the diffuse arc in the source, described by Fig. 7.1D, at which point the magnitude of the d.c. bias again dropped down to 0 V. A further increase in r.f. power caused another increase the d.c. bias.

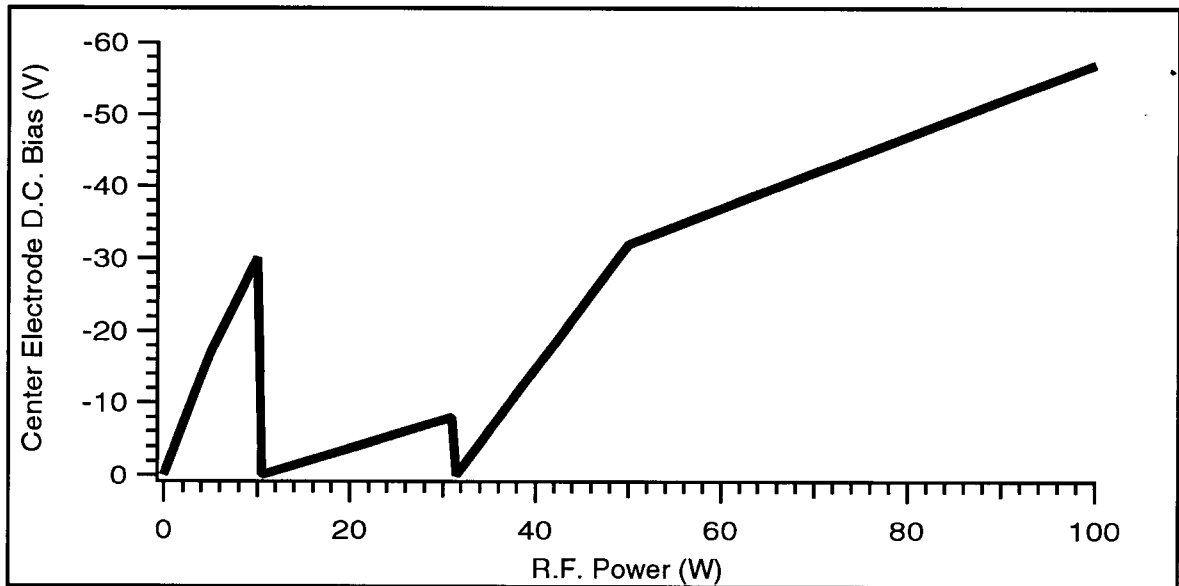


Fig. 7.3 General trend of the d.c. bias on the center electrode in the FAPES source. Data shown represents typical values found over the course of the research.

These measurements support the visual observation that the FAPES source can operate in three different modes. The emission data collected during the course of the studies reported in this thesis did not show any discernible effect from these differences therefore they were not included in the preceding discussions.

During the reduced pressure studies reported in Chapter 6, the d.c. bias was measured as a function of pressure with 60 W r.f. power applied to the center electrode. These results are plotted in Fig. 7.4 which shows that as the pressure was decreased the magnitude of the d.c. bias on the center electrode increased. A complete understanding of the shape of this curve would require further analysis considered beyond the scope of this thesis but the general inverse relationship between pressure and d.c. bias can be explained readily.

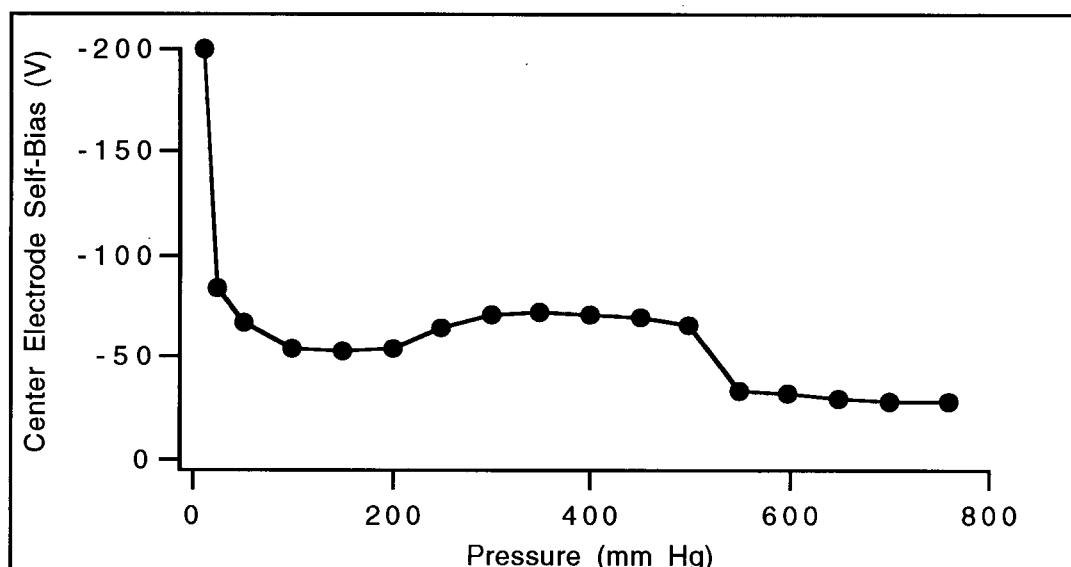


Fig. 7.4 Effect of pressure on the magnitude of the center electrode self-bias for a 60 W plasma.

As the pressure in the source is decreased, the mobility of the charge carriers increases since they undergo fewer collisions. This results in a magnification of the self-bias effect described above.

7.4 Attempts at Spatially Resolved Electron Number Density Measurements

Schram *et al.* [67] have argued that electron densities should be used in describing spectrochemical sources since they are much more sensitive to conditions in plasmas than temperature measurements. They also note, as mentioned in Chapter 1, that in low temperature plasmas, reactions with analytes are usually dominated by charge exchange reactions which can most easily be related to the electron (or ion) density since these are the primary

excitation agents. To this end, attempts were made to measure spatially resolved electron number densities in the FAPES source. The technique chosen was to measure the Stark broadening of the H_{β} line at 486.13 nm since this technique requires no assumption of thermal equilibrium [63].

The use of a 3600 lines/mm grating in the 1 m monochromator with an entrance slit width of 30 μm resulted in a full width at half maximum of 0.02 nm at the H_{β} line. Spatially resolved spectral line profiles of the H_{β} line were taken over a variety of r.f. powers applied to the center electrode and none of the line profiles were significantly wider than that resulting from instrumental broadening. Given the spectral resolution of the system, it can be deduced that the electron number density in the FAPES source must be lower than approximately 10^{14} cm^{-3} . This agrees with Sturgeon *et al.*'s [7] measurements. They calculated electron number densities in the FAPES source from the Stark broadening of the H_{β} line measured using a high resolution échelle grating. They found the electron number density in a 13.56 MHz helium FAPES source to be 9.6, 8.1 and $6.7 \times 10^{13} \text{ cm}^{-3}$ at r.f. powers of 100, 75 and 50 Watts respectively.

CONCLUSIONS

“In studying this Fourth state of Mater we seem at length to have within our grasp and obedient to our control the little indivisible particles which with good warrant are suppose to constitute the physical basis of the universe ... We have actually touched the border land where Matter and Force seem to merge into one another, the shadowy realm between Known and Unknown, which for me has always had peculiar temptations. I venture to think that the greatest scientific problems of the future will find their solution in this Border Land, and even beyond; here it seems to me, lie Ultimate Realities, subtle, far-reaching, wonderful.”

Sir William Crookes (1879) Lecture on “Radiant Matter” delivered to the Brit. Assoc. Adv. Sci., Sheffield, August 22. From [55] .

8.1 Summary

Spatially and temporally resolved spectroscopic studies of a FAPES source have been performed and are reported in this thesis. In this chapter, a brief summary of these studies and their results is given together with some suggestions for further research on the FAPES source.

Atomic and molecular optical emission in the FAPES source was found to have spatial structure and to be dependent on the magnitude of the r.f. power applied to the center electrode. Increasing the r.f. power increased the emission intensity from a He(I) line but did not change its spatial structure significantly. The He(I) emission was found to be most intense adjacent to the center electrode and cuvette wall with some relatively weaker emission throughout the volume of

the cuvette. While this was generally known before, in this thesis the spatial distribution of the He(I) emission has been studied quantitatively and the parametric response noted for the first time. Spatially resolved emission intensities from OH and N_2^+ were used to measure rotational temperatures in the source because these values enable a comparison with other plasma sources and help to understand excitation mechanisms. These showed that there is a fairly significant thermal gradient in the source with OH rotational temperatures ranging between 680 K and 1050 K and N_2^+ rotational temperatures ranging between 580 K and 1920 K in a 20 Watt plasma. Increases in the r.f. power increased the rotational temperature and appeared to increase the dissociation of these molecular species. These spatial emission intensity profiles and rotational temperatures were also consistent with the formation of N_2^+ via a charge transfer reaction with He_2^+ . Lead excitation temperatures were found to increase monotonically with r.f. power over the range of 25 to 75 Watts. A least squares fit to the lead excitation temperature data resulted in a straight line with a slope of 3.8 ± 0.7 K/Watt and an intercept of 4790 ± 40 K at 0 Watts. The information noted above suggested that the source is an atmospheric pressure r.f. glow discharge.

Indium spatially and temporally resolved profiles were measured to gain a better understanding of the plasma discharge and to quantify analyte spatial distributions within the source. Spatially and temporally resolved emission measurements of the In(I) 303.94 nm line showed that there is a significant degree of inhomogeneity in the FAPES source. Three emission maxima were observed in these emission profiles: one adjacent to the center electrode, one adjacent to the cuvette wall, and a third at an intermediate position approximately halfway between the cuvette wall and center electrode. Increases in r.f. power increased the intensity of the intermediate maximum relative to that of the two

maxima adjacent to the center electrode and cuvette wall. While some of this spatial structure had been observed previously, it had not been identified as significant.

The cause of the spatial effects was investigated by measuring absorption profiles to see if the inhomogeneity was caused by the spatial distribution of the analytes in the source. These results showed that, while there is a slight inhomogeneity in the analyte ground state population, the main causes of the complex spatial structure in the FAPES source were the properties of the plasma discharge and not analyte population distributions. The data presented in this thesis are the first quantitative look at this spatial structure and can be interpreted as the presence of negative glows, Faraday dark spaces and a positive column.

Increases in r.f. power increased the emission from the In(I) line up to 40 Watts above which the atomic emission signal decreased. This decrease in the atomic emission signal at higher r.f. powers had been observed before but was not investigated to determine its cause. In this thesis, a trend was found between this observation and the ionization potential of the atom studied, thus the decrease in atomic emission signal was attributed to ionization of the analyte atoms. In order to confirm this hypothesis, the degree of ionization of magnesium was measured in the FAPES source as a function of both r.f. power and spatial position since no previous data of this nature had been reported. This study was also useful in determining the suitability of FAPES as an ion source for mass spectrometric analysis.

Spatially resolved emission measurements from Mg(I) and Mg(II) showed that increases in the r.f. power increased the degree of ionization in the source. Ionization was measured to range between approximately 20% and 30% with r.f.

powers of 10 to 100 Watts respectively. There were maxima in the spatial profile of the degree of ionization as high as 45% adjacent to the center electrode and 40% adjacent to the cuvette wall with 100 Watts r.f. power. The spatially resolved degree of ionization together with the spatially resolved atomic emission signal confirmed that the decrease in atomic emission signal was caused by an increase in analyte ionization mainly adjacent to the center electrode. The ionization data also agreed with the classification of the maxima adjacent to the cuvette wall and center electrode as negative glows and that of the intermediate emission maximum as a positive column.

Reduced pressure He(I) emission studies were then conducted to further confirm these assignments of the spatial zones within the FAPES source. As the pressure was reduced, cathode dark spaces appeared between the negative glows and their respective electrodes. The thickness of these dark spaces were found to increase as the pressure was decreased as the two negative glows moved away from their respective electrodes. Concurrently, the positive column gradually decreased in size until it was no longer present in the discharge.

The concentric spatial zones identified using the results obtained in this study are summarized in Fig. 8.1. This figure is a gray scale representation of a typical emission intensity spatial profile from an analyte in the FAPES source. Moving from the center electrode outwards there is first the brightest zone of the discharge, the inner negative glow, which also has the highest excitation and rotational temperature and the highest degree of ionization. Next is the inner Faraday dark space. A positive column, slightly brighter than the Faraday dark spaces exists halfway between the center electrode and cuvette wall. This is surrounded by the outer Faraday dark space. An outer negative glow adjacent to the cuvette wall is the second brightest region in the discharge and also has the

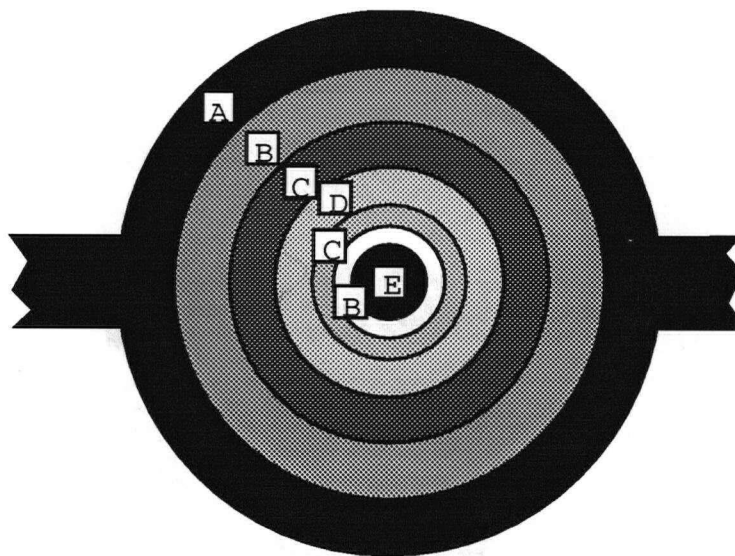


Fig. 8.1: End-view schematic illustration of the FAPES source showing the different spatial zones present at atmospheric pressure. Gray scale represents the relative emission intensity from indium's 303.94 nm line in a 20 Watt plasma.
 A) Graphite Furnace, B) Negative Glow, C) Faraday Dark Space, D) Positive Column, E) Center Electrode

next highest excitation temperature, rotational temperature and degree of ionization.

8.2 Suggestions for Future Research

Spatially resolved emission measurements suggest that the plasma operates as an r.f glow discharge. As such, it may have *some* features in common with other analytical glow discharges such as Grimm lamps. Further investigations in this area may reveal ways of expanding the negative glows to fill

the volume of the graphite cuvette thus increasing the number of analyte atoms excited. Studies have shown that the stability of the discharge is increased by controlling the bias on the center electrode. The application of a positive bias on the center electrode would increase the size and intensity of the emission from the negative glow adjacent to the graphite cuvette by causing the cuvette to spend a longer proportion of time as a cathode throughout the r.f. cycle. An added bonus of this configuration would likely be an increase in the operational lifetime of the center graphite electrode. This is because there would likely be less sputtering of the center electrode if it operated less as a cathode and more as an anode throughout the r.f. cycle. Increasing the size of the center electrode relative to the cuvette would also increase the volume of the negative glow, in this case it would be that of the inner negative glow. A larger center electrode would likely act as a greater condensation site for analyte atoms deposited on the cuvette wall but could also be used as a L'vov platform to improve the analytical performance of the source.

Changing the geometry of the graphite cuvette may also improve the analytical characteristics of the source. The FAPES source is based on a geometry that has been optimized for use as an atomizer for absorption measurements. While this geometry is also optimized to increase the residence time of analyte atoms in the source, it is not the ideal geometry to measure emission. This is because the efficiency of measuring optical emission from a spatial zone decreases away from the zone focused onto the detector. Changing the geometry may also make it possible to increase the maximum operational r.f. power of the source. At present the upper power limit is determined by the onset of an arc discharge. The r.f. power at which this arc occurs may be increased by increasing the dimensions of the source. These changes in the geometry of the

source could be implemented in a single design — a FAPES source with a shorter and larger diameter graphite cuvette together with a larger diameter center electrode.

It is clear from the rotational temperature and emission profiles found that future studies in the FAPES source should be conducted with the spatial structure of the plasma in mind. Namely, reports of such characteristics as rotational, excitation, or ion temperatures and electron number densities should include information on the viewing zone observed for the study. These should ultimately lead to the determination of an analytical zone in both physical and parameter space. Since the source is not spatially homogeneous, an analytical zone should exist within the volume of the graphite cuvette. It should be possible to improve the analytical characteristics of this source by optimizing the choice of the location and size of the viewing zone. As such the analytical characteristics of the FAPES source should now be investigated with spatial position as one of the important parameters of the study.

The FAPES source has reached a point in its development where it is time to see if it is a viable instrument for spectrochemical analysis. In this research direction, complete analytical methods should be developed for the simultaneous multielemental analysis of real samples (as opposed to analytical standards). This will require the use of compromise conditions for both the r.f. power applied to the center electrode and the graphite cuvette's temperature heating program. Increased sensitivity and reduced detection limits may be obtained by using current GFAAS technologies such as the use of chemical modifiers and L'vov platforms. Ways of increasing the linear dynamic range should also be investigated. These could include the use of condensation sites or a gas cross flow in front of the source to remove ground state atoms.

REFERENCES

1. D. C. Liang and M. W. Blades, *Spectrochim. Acta* **44B**, 1059 (1989).
2. R. E. Sturgeon, S. N. Willie, V. Luong, S. S. Berman and J. G. Dunn, *J. Anal. At. Spectrom.* **4**, 669 (1989).
3. D. L. Smith, D. C. Liang, D. Steel and M. W. Blades, *Spectrochim. Acta* **45B**, 493 (1990).
4. R. E. Sturgeon, S. N. Willie, V. Luong and S. S. Berman, *J. Anal. At. Spectrom.* **5**, 635 (1990).
5. R. E. Sturgeon, S. N. Willie, V. Luong and S. S. Berman, *Anal. Chem.* **62**, 2370 (1990).
6. R. E. Sturgeon, S. N. Willie, V. Luong and S. S. Berman, *J. Anal. At. Spectrom.* **6**, 19 (1991).
7. R. E. Sturgeon, S. N. Willie and V. T. Luong, *Spectrochim. Acta* **46B**, 1021 (1991).
8. R. E. Sturgeon, S. N. Willie, V. T. Luong and J. G. Dunn, *Appl. Spectrosc.* **45**, 1413 (1991).
9. P. R. Banks, D. C. Liang and M. W. Blades, *Spectroscopy* **7**, 36 (1992).
10. T. D. Hettipathirana and M. W. Blades, *Spectrochim. Acta* **47B**, 493 (1992).
11. T. D. Hettipathirana and M. W. Blades, *J. Anal. At. Spectrom.* **7**, 1039 (1992).
12. R. E. Sturgeon and S. N. Willie, *J. Anal. At. Spectrom.* **7**, 339 (1992).
13. G. F. R. Gilchrist, P. M. Celliers, H. Yang, C. Yu and D. C. Liang, *J. Anal. At. Spectrom.* **8**, 809 (1993).
14. G. F. R. Gilchrist and D. C. Liang, *Am. Lab. March*, 34U (1993).
15. T. D. Hettipathirana, Ph.D. Thesis, University of British Columbia (1993).
16. T. D. Hettipathirana and M. W. Blades, *J. Anal. At. Spectrom.* **8**, 955 (1993).
17. K. E. A. Ohlsson, R. E. Sturgeon, S. N. Willie and V. T. Luong, *J. Anal. At. Spectrom.* **8**, 41 (1993).

18. R. E. Sturgeon, V. T. Luong, S. N. Willie and R. K. Marcus, *Spectrochim. Acta* **48B**, 893 (1993).
19. S. Imai and R. E. Sturgeon, *J. Anal. At. Spectrom.* **9**, 765 (1994).
20. S. Imai and R. E. Sturgeon, *J. Anal. At. Spectrom.* **9**, 493 (1994).
21. S. Imai, R. E. Sturgeon and S. N. Willie, *J. Anal. At. Spectrom.* **9**, 759 (1994).
22. V. Pavski, C. L. Chakrabarti and R. E. Sturgeon, *J. Anal. At. Spectrom.* **9**, 1399 (1994).
23. M. M. Rahman, M.Sc. Thesis, University of British Columbia (1994).
24. C. W. Le Blanc and M. W. Blades, *Spectrochim. Acta* **50B**, 1395 (1995).
25. G. Kirchhoff and R. Bunsen, *Phil. Mag.* **22**, 329 (1861).
26. W. H. Hartley, *J. Chem. Soc.*, 210 (1882).
27. A. Walsh, *Spectrochim. Acta* **7**, 108 (1955).
28. B. V. L'vov, *Spectrochim. Acta* **17**, 761 (1961).
29. J. D. Winefordner, G. A. Petrucci, C. L. Stevenson and B. W. Smith, *J. Anal. At. Spectrom.* **9**, 130 (1994).
30. C. M. M. Smith, J. M. Harnly, G. P. Moulton and T. C. O'Haver, *J. Anal. At. Spectrom.* **9**, 419 (1994).
31. C. M. M. Smith and J. M. Harnly, *Spectrochim. Acta* **49B**, 387 (1994).
32. J. M. Harnly and B. Radziuk, *J. Anal. At. Spectrom.* **10**, 197 (1995).
33. M. W. Blades, P. Banks, C. Gill, D. Huang, C. Le Blanc and D. Liang, *I.E.E.E. Trans. Plasma Sci.* **19**, 1090 (1991).
34. J. A. C. Broekaert, *Mikrochim. Acta* **120**, 21 (1995).
35. W. B. Thompson, *An Introduction to Plasma Physics* (Pergamon Press, New York, 1962).
36. C. J. Molnar, F. S. Chuang and J. D. Winefordner, *Spectrochim. Acta* **30B**, 183 (1975).
37. J. M. Ottaway and F. Shaw, *Analyst* **100**, 438 (1975).
38. D. C. Baxter and W. Frech, *Spectrochim. Acta* **50B**, 655 (1995).
39. D. C. Baxter, *Spectrochim. Acta* **43B**, 129 (1988).

40. J. J. Schwab and R. J. Lovett, *Spectrochim. Acta* **45B**, 281 (1990).
41. D. Littlejohn and J. M. Ottaway, *The Analyst* **104**, 208 (1979).
42. H. Falk, E. Hoffmann and C. Lüdke, *Prog. Anal. Spectrosc.* **11**, 417 (1988).
43. H. Falk, *Spectrochim. Acta* **32B**, 437 (1977).
44. H. Falk, E. Hoffmann, I. Jaeckel and C. Lüdke, *Spectrochim. Acta* **34B**, 333 (1979).
45. H. Falk, E. Hoffmann and C. Lüdke, *Spectrochim. Acta* **36B**, 767 (1981).
46. H. Falk, E. Hoffmann, C. Ludke, J. M. Ottaway and S. K. Giri, *Analyst* **108**, 1459 (1983).
47. H. Falk, E. Hoffmann and C. Lüdke, *Spectrochim. Acta* **39B**, 283 (1984).
48. K. Dittrich, H. Fuchs and *J. Anal. At. Spectrom.* **5**, 39 (1990).
49. N. Ballou, D. L. Styris and J. M. Harnly, *J. Anal. At. Spectrom.* **3**, 1141 (1988).
50. J. M. Harnly, D. L. Styris and N. E. Ballou, *J. Anal. At. Spectrom.* **5**, 139 (1990).
51. P. G. Riby, J. M. Harnly, D. L. Styris and N. E. Ballou, *Spectrochim. Acta* **46B**, 203 (1991).
52. P. G. Riby and J. M. Harnly, *J. Anal. At. Spectrom.* **8**, 945 (1993).
53. D. F. Fang and R. K. Marcus, in *Glow Discharge Spectroscopies* R. K. Marcus, Ed. (Plenum Press, New York, 1993) pp. 17-66 of 514.
54. J. R. Roth, *Industrial Plasma Engineering: Volume 1 Principles* (Institute of Physics Publishing, Philadelphia, 1995), vol. 1.
55. J. H. Ingold, in *Gaseous Electronics* M. N. Hirsh, H. J. Oskam, Eds. (Academic Press, New York, 1978), vol. 1.
56. B. Chapman, *Glow Discharge Processes: Sputtering and Plasma Etching* (John Wiley & Sons, New York, 1980).
57. A. M. Howatson, *An introduction to gas discharges* (Pergamon Press, Oxford, ed. 2, 1976).
58. H. A. Schwab and C. K. Manka, *J. Appl. Phys.* **40**, 696 (1969).
59. H. A. Schwab and R. F. Hotz, *J. Appl. Phys.* **41**, 1503 (1970).

60. H. A. Schwab, *J. Appl. Phys.* **41**, 1508 (1970).
61. H. A. Schwab, *Proc. I. E. E. E.* **59**, 613 (1971).
62. R. F. Hotz, *J. Appl. Phys.* **41**, 1500 (1970).
63. H. R. Griem, *Plasma Spectroscopy* (McGraw-Hill Book Company, New York, 1964).
64. H. R. Griem, *Spectral Line Broadening by Plasmas*. H. S. W. Massey, K. A. Brueckner, Eds., *Pure and Applied Physics* (Academic Press, New York, 1974), vol. 39.
65. R. H. Huddlestone and S. L. Leonard, *Plasma Diagnostic Techniques* (Academic Press, New York, 1965).
66. J. J. D. Ingle and S. R. Crouch, *Spectrochemical Analysis* (Prentice Hall, Englewood Cliffs, 1988).
67. D. C. Schram, J. A. M. van der Mullen, J. M. de Regt, D. A. Benoy, J. Jonkers and F. H. A. G. Fey, *Fundamental Description of Spectrochemical ICP Discharges*, 1996 Winter Conference on Plasma Spectrochemistry, Ft. Lauderdale, FL (1996).
68. J. M. Mermet, in *Inductively coupled plasma emission spectroscopy - Part 2: Applications and fundamentals* P. W. J. M. Boumans, Ed. (John Wiley & Sons, Inc., New York, 1987).
69. A. P. Thorne, *Spectrophysics* (Chapman and Hall, London, ed. 2, 1988).
70. P. W. J. M. Boumans, *Theory of Spectrochemical Excitation* (Hilger & Watts Ltd., London, NW, ed. 1st, 1966).
71. I. Ishii and A. Montaser, *Spectrochim. Acta* **46B**, 1197 (1991).
72. A. H. Ali, K. C. Ng and J. D. Winefordner, *Spectrochim. Acta* **46B**, 1207 (1991).
73. R. P. Feynman, R. B. Leighton and M. Sands, *The Feynman Lectures on Physics* (Addison-Wesley Publishing Company, Menlo Park, 1963), vol. 1.
74. M. W. Blades, *Spectrochim. Acta* **49B**, 47 (1994).
75. F. W. Sears, *Optics*, Principles of physics. (Addison-Wesley Press, Cambridge, Mass., 1949), vol. 3.
76. P. B. Farnsworth, B. W. Smith and N. Omenetto, *Spectrochim. Acta* **45B**, 1151 (1990).
77. P. W. J. M. Boumans, *Spectrochim. Acta* **46B**, 711 (1991).

78. G. Herzberg, *Spectra of Diatomic Molecules* (Van Nostrand, Princeton, NJ, 1950).
79. J. Lotrian, Y. Guern and J. Cariou, A. Johannin-Gilles, *J. Quant. Spectrosc. Radiat. Transfer* **21**, 143 (1979).
80. C. H. Corliss and W. R. Bozman, "Experimental Transition Probabilities for Spectral Lines of Seventy Elements, NBS Monograph #53" (US Dept. of Commerce, 1962).
81. A. A. Radzig and B. M. Smirnov, *Reference data on atoms, molecules, and ions*. J. P. Toennies, Ed., Springer series in chemical physics. (Springer-Verlag, Berlin, 1985), vol. 31.
82. M. Endoh and M. Tsuji, Y. Nishimura, *J. Chem. Phys.* **79**, 5368 (1983).
83. B. M. Spencer, B. W. Smith and J. D. Winefordner, *Appl. Spectrosc.* **48**, 289 (1994).
84. J. A. Holcombe, G. D. Rayson and J. N. Akerlind, *Spectrochim. Acta* **37B**, 319 (1982).
85. J. McNally and J. A. Holcombe, *Anal. Chem.* **63**, 1918 (1991).
86. C. W. Huie and J. C. J. Curran, *Appl. Spectrosc.* **72**, 1307 (1988).
87. J. D. Stafford and J. A. Holcombe, *J. Anal. At. Spectrom.* **3**, 35 (1988).
88. A. K. Gilmutdinov, Y. A. Zakharov, V. P. Ivanov and A. V. Voloshin, *J. Anal. At. Spectrom.* **6**, 505 (1991).
89. A. K. Gilmutdinov, Y. A. Zakharov, V. P. Ivanov and A. V. Voloshin, *J. Anal. At. Spectrom.* **7**, 675 (1992).
90. A. K. Gilmutdinov, Y. A. Zakharov and A. V. Voloshin, *J. Anal. At. Spectrom.* **8**, 387 (1993).
91. B. V. L'vov, *Spectrochim. Acta* **33B**, 153 (1978).
92. A. K. Gilmutdinov, B. Radziuk, M. Sperling, B. Welz and K. Y. Nagulin, *Appl. Spectrosc.* **49**, 413 (1995).
93. W. L. Wiese, M. W. Smith and B. M. Miles, "Atomic transition probabilities: Volume II Sodium through calcium, a critical data compilation." *NSRDS-NBS 22* (Nat. Bur. Stand. (U.S.), 1969).
94. P. W. J. M. Boumans, in *Analytical Emission Spectroscopy*, E. L. Grove, Ed. (Marcel Dekker, Inc., New York, 1972), vol. 1.
95. L. Bezur, J. Marshall, J. M. Ottaway and R. Fakhrul-Aldeen, *Analyst* **108**, 553 (1983).

96. K. A. Rubinson, *Chemical Analysis* (Little, Brown and Company, Boston, 1987).
97. J. M. Mermet, *Anal. Chim. Acta* **250**, 85 (1991).
98. J. M. Mermet, *Appl. Spectrosc.* **49**, 12A (1995).
99. S. Tanner, . Personal communications, (1996).
100. K. K. Darrow, *Electrical Phenomena in Gases* (The Williams and Wilkins Company, Baltimore, 1932).
101. E. Nasser, *Fundamentals of gaseous ionization and plasma electronics*. S. C. Brown, Ed., Wiley series in plasma physics (Wiley-Interscience, New York, 1971).
102. W. E. Wentworth, Y. Qin, S. Wiedeman, S. D. Stearns and J. Madabushi, *Appl. Spectrosc.* **49**, 1282 (1995).
103. E. W. McDaniel, *Collision Phenomena in Ionized Gases*. S. C. Brown, Ed., Wiley Series in Plasma Physics (John Wiley & Sons, Inc., New York, 1964).
104. S. C. Brown, *Basic Data of Plasma Physics*. S. C. brown, Ed., Basic Data of Plasma Physics (John Wiley & Sons, Inc., New York, 1966).
105. F. Llewellyn-Jones, *The Glow Discharge* (John Wiley & Sons Inc., New York, 1966).